LAYER-BY-LAYER FILMS VIA 3D DROP ON DEMAND PRINTING

by

Ray Cook

A dissertation submitted to the Graduate Council of
Texas State University in partial fulfillment
of the requirements for the degree of
Doctor of Philosophy
with a Major in Material Science, Engineering, and Commercialization
August 2014

Committee Members:

Gary W. Beall, Chair

Clois E. Powell

Ravi Droopad

Yihong Chen

Raymond Fisk

FAIR USE AND AUTHOR'S PERMISSION STATEMENT

Fair Use

Duplication Permission

ACKNOWLEDGEMENTS

I would like to thank my committee chair and advisor, Dr. Gary Beall for his guidance and support throughout the long and challenging path of my research and course work. I would also like to thank Dr. Powell, Dr. Chen, and Dr. Droopad, and for agreeing to be part of my committee and taking the time to work with me and sharing their equipment, knowledge, and skills which allowed me to complete my research. I would like to thank Dr. Fisk for his guidance in market research and commercial aspects of the program. I would like to acknowledge and thank all of the faculty and staff associated with the MSEC Program. Without their support and dedication there would not be an MSEC Program. I would also like to thank all of my fellow classmates for their support and camaraderie.

Most of all I would like to thank my family, for their patience and understanding through this tough and trying period of our lives. Without them, I would not have achieved many of the accomplishments I have today.

I would also like to acknowledge the Ingram School of Engineering for providing me the opportunity to achieve this monumental goal. I would like to acknowledge the support of all the faculty and staff within the Ingram School of Engineering and I would especially like to thank the schools director Dr. Stern for his support and belief in my abilities to accomplish this degree. I would also like to thank his successor, Dr. McClellan for continuing that support and belief.

TABLE OF CONTENTS

Page

ACKNOWLEDGEMENTS iv

LIST OF TABLES vii

LIST OF FIGURES viii

LIST OF ABBREVIATIONS xiii

ABSTRACT xiv

CHAPTER

1. INTRODUCTION 1

    1.1 Background 1
    1.2 Objectives and Dissertation Outline 3

2. LITERATURE REVIEW 6

    2.1 Layer by Layer Assembly 8
    2.2 Drop on Demand Printing 12
        2.2.1 Drop on Demand Basics 12
    2.3 Drop Development 13
    2.4 Drop/Substrate Interaction 17
    2.5 Drop Impact and Spreading 17
    2.6 Drop Coalescence and Pattern Stability 20
    2.7 Barrier Films 20
        2.7.1 Tortuous Path Theories 20
    2.8 Filled Polymers 24

3. EXPERIMENTAL METHODS 31

    3.1 Establishment of Parameters for Drop on Demand Printing 31
    3.2 Establishment of Weight % of Material Required for Printing 31
    3.3 Establishment of Drop Formation and Rate 36
        3.3.1 Formation of Solution 36

4. CREATION OF FILMS 39

4.1 Layering of Materials 39
4.1.1 PVP and MMT Clay 39
4.1.2 PVA and MMT Clay 40
4.1.3 PEG and MMT Clay 43
4.1.4 Graphenol and MMT Clay 44
4.2 Film Characterization 45
4.2.1 Optical Microscope 45
4.2.2 Profilometer 46
4.2.3 Scanning Electron Microscope (SEM) 46
4.2.4 Atomic Force Microscope (AFM) 47
4.2.5 Permeability Study 47
4.2.6 Wide Angle X-ray Scattering (WAXS) 47

5. RESULTS AND DISCUSSION 48

5.1 PVP and MMT Clay 48
5.2 PVA and MMT Clay 62
5.3 PEG and MMT Clay 69
5.4 Graphenol and MMT Clay 72
5.5 Wide Angle X-ray Scattering (WAXS) Results and Analysis 74

6. CONCLUSIONS 80

6.1 Summary 80
6.2 Commercialization Potential 82
6.3 Limitations 83
6.4 Future Work 83

APPENDIX SECTION 84

LITERATURE CITED 114

LIST OF TABLES

Table **Page**

1. Results of bilayer formation from different charge density clays and polymers 30

2. Settings used to print films comprising of PVP, MMT, PVA PEG, and Graphenol ...38

3. Oxygen Transition Rates for DOD printed films made of PVP & MMT nanoclay 48

4. Oxygen Transition Rates for DOD printed films made of PVP & MMT nanoclay 49

5. Calculated thickness of films created from a solution of PVP & MMT.....62

6. Calculated film thickness for a film created from a solution of PVA & MMT.....68

7. Oxygen Transmission rates for films created from a solution of PVA & MMT with no PVP base coat and with a PVP base coat.....69

8. Oxygen Transmission rates for films created from a solution of PEG & MMT with no PVP base coat and with a PVP base coat.....70

9. Calculated thickness of films created from a solution of PEG & MMT 72

10. Oxygen Transmission Rates of films created from a solution of Graphenol & MMT 72

11. Film thickness values for each bi-layer 81

LIST OF FIGURES

Figure **Page**

1. (A) Image of layer-by-layer assembly with cationic polyethylenimine (PEI) and anionic montmorillonite (MMT) and (B) across-sectional view of the resultant nanobrick wall microstructure 7

2. (A) 300-bilayer PVA/MMT free-standing film. (B) SEM cross sectional view of the film....11

3. DOD printing 14

4. Image showing three drops ejected from a DOD printer at different stages of drop formation 15

5. The image shows the sequence of events that occurs after droplet impact on a substrate 19

6. Image showing the path of diffusing a molecule through a tortuous pathway with impermeable parts....22

7. Image showing layered silicates-filled polymer composites can have an intercalated (A) or disordered structure (B)....25

8. Image of basic polymer structures 26

9. Depiction of a polymer bonded to MMT nanoclay particles....27

10. Molecular model of PVP bonded to MMT clay 28

11. Graph indicating the steps in d-spacing for PVP intercalates at various loadings of PVP 29

12. Image of a Dimatix DMC-11601 print head and ink solution cartridge....33

13. Image of a Dimatix DMP-2831 Materials Printer 34

14. Image of Dimatix DMP-2831 Printer cartriage settings screen....35

15. Image from Dimatix DMP-2831 Printer Drop Watcher screen 36

16. Image of a fiducial camera mounted on a Dimatix DMP-2831 DOD Printer 41

17. Image from the fiducial camera screen of a Dimatix DMP-2831 DOD Printer 42

18. Images of films made from solutions of PVP & MMT 50

19. Images showing the effects of no platen heat (A) vs. platen heat (B) on films made from solutions of PVP & MMT 51

20. Images showing the effects of drop spacing 52

21. Image showing the effects of drop spacing without heat, the drop spacing is at 12μm and room temperature 52

22. Images of films created from solutions of PVP & MMT with varying numbers of jets/nozzles 53

23. SEM images showing dispersed clay in films created from a solution of PVP & MMT nanoclays 54

24. AFM image of a film created from a solution of PVP & MMT nanoclay 55

25. Image of EDAX point analysis performed on a film made from a solution of PVP & MMT 56

26. Image of EDAX point (1) analysis performed on a film made of PVP & MMT printed on a Mylar substrate 57

27. Image of EDAX point (2) analysis performed on a film made of PVP & MMT printed on a Mylar substrate 57

28. Image of EDAX point (3) analysis performed on a film made of PVP & MMT printed on a Mylar substrate 58

29. Image of EDAX point (4) analysis performed on a film made of PVP & MMT printed on a Mylar substrate 58

30. SEM image indicating the thickness of a single Bilayer of a film made of PVP & MMT 60

31. Optical microscope image indicating the film thickness of a film made from 1 Bilayer of PVP & MMT, film thickness average is 3.6µm 60

32. Optical microscope image indicating the film thickness of a film made from 3 Bilayers of PVP & MMT, film thickness average is 7.5µm.....61

33. Optical microscope image indicating the film thickness of a film made from 6 Bilayers of PVP & MMT, film thickness average is 14.5µm.....61

34. Image (A) 1 bi-layer and (B) 6 bi-layers of films created from a solution of PVA & MMT with no PVP basecoat.....63

35. Image (A) 1 bi-layer and (B) 6 bi-layers of films created from a solution of PVA & MMT with a PVP basecoat.....63

36. AFM image of a film created from a solution PVA & MMT.....64

37. Images of a film created from a solution of PVA & MMT indicating the effects of heat on the film formation 65

38. Image of EDAX point analysis performed on a film made of PVA & MMT printed on a Mylar substrate 66

39. Image of EDAX point (1) analysis of the PVA/MMT film on a Mylar substrate.....67

40. Image of EDAX point (2) analysis of the PVA/MMT film on a Mylar substrate.....67

41. Image of EDAX point (3) analysis of the PVA/MMT film on a Mylar substrate.....68

42. Images of films created from a solution of PEG & MMT indicating the effects of film formation with no PVP base coat.....70

43. Images of films created from a solution of PEG&MMT indicating the effects of film formation with a PVP base coat.....71

44. Images of films created from a solution of Graphenol & MMT indicating the effects of film formation with no PVP base coat.....73

45. Images of films created from a solution of Graphenol & MMT indicating the effects of film formation with a PVP base coat 73

46. Wide Angle X-ray Scattering results for a 1 bi-layer film created from a solution of PVP & MMT 75

47. Wide Angle X-ray Scattering results for a 2 bi-layer film created from a solution of PVP & MMT 75

48. Wide Angle X-ray Scattering results for a 3 bi-layer film created from a solution of PVP & MMT 76

49. Wide Angle X-ray Scattering results for a 4 bi-layer film created from a solution of PVP & MMT 76

50. Wide Angle X-ray Scattering results for a 5 bi-layer film created from a solution of PVP & MMT 77

51. Wide Angle X-ray Scattering results for a 6 bi-layer film created from a solution of PVP & MMT 77

52. Wide Angle X-ray Scattering results for a 6 bi-layer film created from a solution of PVA & MMT.....78

53. Wide Angle X-ray Scattering results for a 6 bi-layer film created from a solution of PEG & MMT 79

54. Wide Angle X-ray Scattering results for a Mylar substrate without any coating.....79

55. Oxygen transmission rate comparison of films made with a DOD printer.....80

A1-1. Page 23 of operations manual for Dimatix DMP 2831 Printer 84

A1-2. Page 24 of operations manual for Dimatix DMP 2831 Printer 85

A1-3. Page 25 of operations manual for Dimatix DMP 2831 Printer 86

A1-4. Page 26 of operations manual for Dimatix DMP 2831 Printer 87

A1-5. Page 27 of operations manual for Dimatix DMP 2831 Printer 88

A1-6. Page 28 of operations manual for Dimatix DMP 2831 Printer 89

A1-7. Page 29 of operations manual for Dimatix DMP 2831 Printer 90

A1-8. Page 30 of operations manual for Dimatix DMP 2831 Printer 91

A1-9. Page 31 of operations manual for Dimatix DMP 2831 Printer 92

A2-1. Page 61 of operations manual for Dimatix DMP 2831 Printer 93

A2-2. Page 62 of operations manual for Dimatix DMP 2831 Printer 94

A2-3. Page 63 of operations manual for Dimatix DMP 2831 Printer 95

A2-4. Page 64 of operations manual for Dimatix DMP 2831 Printer 96

A2-5. Page 65 of operations manual for Dimatix DMP 2831 Printer 97

A2-6. Page 66 of operations manual for Dimatix DMP 2831 Printer 98

A3-1. Page 39 of operations manual for Dimatix DMP 2831 Printer 99

A3-2. Page 40 of operations manual for Dimatix DMP 2831 Printer 100

A3-3. Page 41 of operations manual for Dimatix DMP 2831 Printer 101

A3-4. Page 42 of operations manual for Dimatix DMP 2831 Printer 102

A4-1. Page 79 of operations manual for Dimatix DMP 2831 Printer 103

A4-2. Page 80 of operations manual for Dimatix DMP 2831 Printer 104

A4-3. Page 81 of operations manual for Dimatix DMP 2831 Printer 105

A5-1. Image of a BURKER NANO Dimension 3100 AFM 106

A5-2. Image of an Olympus BX60 Optical Microscope 106

A5-3. Image of a Alpha Step 500 Surface Profilometer.....107

A5-4. Image of a Helios Nano Lab 400 Scanning Electron Microscope.....107

A5-5. Image of a Bruker D8 Focus Powder X-Ray Diffractometer.....108

A5-6. Image of a Mocon Ox-Tron 2/60 Oxygen and Moisture analyzer 108

LIST OF ABBREVIATIONS

DOD	Drop on Demand, a form of inkjet printing
PVP	Polyvinylpyrrolidone, a water soluble polymer
PVA	Polyvinyl Alcohol, a water soluble polymer
PEG	Polyethylene Glycol, a water soluble polymer
MMT	Montmorillonite nanoclay
LBL	Layer By Layer, a form of making thin films
3D	Three dimensional printing
PDDA	Polydiallyldimethylammonium chloride
PAH	Polyallylamine hydrochloride
PEI	Polyethylenimine
OTR	Oxygen Transmission Rate
LCD	Liquid Crystal Display
OLED	Organic Light Emitting Diode
SEM	Scanning Electron Microscope
WAXS	Wide Angle X-ray Scattering
AFM	Atomic Force Microscope
DI	Deionized, referring to water

ABSTRACT

The traditional method for making Layer-By-Layer films is a laborious, expensive, wasteful, and non-ecofriendly process; therefore this study was conducted to find a faster, more cost efficient, and non-wasteful method of producing ecofriendly Layer-By-Layer films which could potentially be used in the food and beverage packaging industry.

Thin films consisting of polymers and nanoclays were produced utilizing a Drop on demand (DOD) 3D printer, where small droplets of solutions and suspensions were dispensed onto Mylar substrates in pre-defined patterns in a non-contact manner. Once the solution had dried, the residual compounds yielded an array of materials, which could potentially be used in various applications, such as an oxygen barrier film.

The preparation of thin films on substrates via 3D drop on demand printing is particularly attractive as a means of preparing polymer microarrays. The size of the deposited structures is on the order of tens or hundreds of microns. This coincides with the dimensions used in different types of gas barriers, moisture barriers, UV prevention coatings, and drug release applications.

Different concentrations of ink solutions of polymers and nanoclays were printed on a Mylar substrate and analyzed for their effectiveness as a gas barrier film for various applications, primarily focusing on oxygen. The study evaluated the physical and functional properties of the different solutions. Each ink solution was analyzed using

different material characterization techniques. The research yielded surprising and promising results with some of thin films exhibiting very good oxygen barrier properties, such as the combination of PVP & MMT and some like PEG & MMT that did not.

CHAPTER 1

Introduction

1.1 Background

The preparation of Layer-By-Layer (LBL) barrier films on different types of substrates is an area of highly active research. Developing thin films with different chemistries on a single substrate is a goal shared by a wide range of basic and applied materials science disciplines. Reproducible films on various substrate materials with different compositions but with a well-defined and comparable geometry allows for a better understanding of structure-property relationships.

Traditional LBL gas barrier films are produced by a dipping and drying technique where a substrate is dipped in a predetermined solution followed by rinsing and drying. Next, the substrate is dipped in second predetermined solution followed by rinsing and drying. The rinsing steps dramatically limit the practical applications of the LBL technique by adding processing time and waste. Modifications to the technology have accelerated the process with spraying and/or spin coating. Rinsing steps are still required for film production and structural control. The entire process is repeated, some twenty to forty times until the desired thickness and or properties are obtained. This process is time consuming, produces a lot of waste, costly, and limited in what types of materials can be combined. Therefore, it has attracted very little attention thus far.

One popular microfluidics technique for preparing layer-by-layer thin films is inkjet drop on demand (DOD) 3D printing, where small sub-nanoliter droplets of solutions and suspensions are dispensed onto substrates in pre-defined patterns in a non-contact manner. This process is employed by dispensing various materials as inks onto a

surface. Once the solution has dried, the residual compounds yield an array of materials, which can be used in various applications.

The preparation of thin films on substrates via 3D drop on demand printing is particularly attractive as a means of preparing polymer microarrays. The size of the deposited structures is on the order of tens or hundreds of microns. This coincides with the dimensions used in different types of gas barriers, moisture barriers, UV prevention coatings, and drug release applications. Film production via LBL drop on demand printing is an attractive alternate method that can deliver precise amounts of each component for the formation of LBL films without the need of any rinsing. The replacement of the numerous rinsing steps saves material, time, and money. The technique offers nanoscale control over layer thickness, variable coverage of the surface, and compatibility with additive schemes of film manufacturing, which sets it apart from the traditional dip and rinse LBL method.[1] The vast range of materials that can be deposited with this method has not been determined but it may be limitless. Drop on demand 3D LBL printing is a convenient and economical alternative method of patterning surfaces with composite materials that is expected to be useful for the developing advanced materials and films.

Advances in 3D drop on demand LBL printing technology has resulted in an increase in the creation of films generated via a printer. The growing gas barrier film market is demanding cost effective and efficient application processes that can be tailored to fit specific gas barrier needs and applications. Drop on demand 3D LBL printing satisfies these requirements. Several printer companies have printers capable of printing a wide range of ink solutions, which are commonly used to make gas barrier films. The

printers range in size from a desktop to an industrial size unit that will print on substrates over several feet wide.

One of the big advantages of drop on demand 3D printing over the traditional dip and rinse LBL method is the reduced time required to produce a film. The dip and rinse method requires longer drying times between each deposited layer. The drop on demand process deposits a very small amount of material (pico-size droplets) and therefore dries very fast. Faster drying times allow additional layers to be added quickly. The rate of production increases and thus leads to a final product in a shorter period of time.

The small ink droplets produced by drop on demand printing allow for a precise deposit of solutions. A more uniformed structure and better performing material is produced. The high precision deposition method eliminates material waste. It is easier to tailor and reproduce films to meet specific application requirements. It is difficult to make very small changes to the chemistry of films produced by the dip and rinse method. The drop on demand printing process allows for changing the drop size and therefore the ability to make submicron changes to the chemistry. The further development of this technology will help create optimized cost effective gas barrier films, save energy, and reduce chemical waste. 3D printing provides a method for making films, which cannot be made with the traditional dip, rinse, and dry method.

1.2 Objectives and Dissertation Outline

Different concentrations of ink solutions consisting of polymers and nanoclays were printed on Mylar substrates to determine if films can be produced via 3D drop on demand inkjet printing and analyzed for their effectiveness as a gas barrier film for various applications, primarily focusing on oxygen due to the predicted growth in the

oxygen barrier film market. The study evaluated the physical and functional properties of the different solutions. Each ink solution were printed on Mylar substrates using a Dimatix DMP 2831 3D drop on demand printer and then analyzed using different material characterization techniques such as Optical Microscopy, Atomic Force Microscopy, Scanning Electron Microscopy, Elemental Data Analysis, Wide Angle X-ray Scattering, and Oxygen Transition Rate.

It is hoped that this work will result in a low cost, transparent, and more flexible barrier film than is currently available for a variety of packaging applications (e.g., food, beverage, drug, and flexible electronics). Impermeable clay platelets make the diffusion length longer through a polymer matrix by creating a tortuous path that reduces the oxygen transmission rate (OTR).[2,3,4,5] The tortuous path concept was initially proposed by Nielsen and further developed by Cussler and others.[6,7,8,9] With regard to the study of LBL assemblies with clay, the key tasks include:

1. Formulating printable ink solutions;
2. Print films consisting of PVP, PEG, PVA, MMT clay, and Graphenol;
3. Measuring the Oxygen transmission rate (OTR) of clay-based LBL assemblies as a function of bilayers printed with a Dimatix DMP 2831 Fujifilm 3D drop on demand printer;
4. Evaluating film structure with optical microscopy, electron microscopy (SEM), atomic force microscopy (AFM), and surface profilometer;
5. Correlating barrier behavior to film thickness.

Chapter II is a literature review of LBL assembly, drop on demand systems, and current oxygen barrier systems. An in depth review of the physical and chemical concepts

of LBL assembly, and the types of functional films that can be produced, is provided. A review of current barrier technologies and several theories dealing with the tortuous pathway concept is also described in detail.

Chapter III discusses the methods behind the project. The printing equipment used, and the method of drop formulation are presented. Solutions were created as a percent weight by volume, and the final parameter settings are given. Chapter IV pertains to the creation of the films. The process behind forming the different samples and quantities is discussed, as are the methods of characterization. Chapter V gives the relevant and pertinent results of the various characterizations.

Chapter VI provides conclusions and future directions for clay-based assemblies, their possible use as a flame retardant coating for foam and dielectric layer for thin film capacitors.

CHAPTER 2

Literature Review

In the early 1960s, Dr. Sweet of Stanford University demonstrated that by applying a pressure wave pattern to an orifice, the ink stream could be broken into droplets of uniform size and spacing.[10] This process became known as continuous ink-jet printing. This led to the development of other printing techniques in the late 1970's, one of which is the drop on demand process.[11] Zoltan, Kyser, and Sears are among the pioneer inventors of the drop-on-demand ink-jet systems.[12,13]

The majority of the activity in LBL printing today is with the drop-on-demand method. Depending on the mechanism used in the drop formation process, the technology can be categorized into four major application methods: thermal, piezoelectric, electrostatic, and acoustic ink-jet. Most of the drop-on-demand printers on the market today use the thermal or the piezoelectric principle. The piezoelectric seems to be the better choice, because it is more adjustable and durable, and is the industry standard in this particular field. It works well with a variety of different types of materials and produces better control over the ink solution dispersion.

Many composite materials produced via the traditional dip, rinse, and dry layer-by-layer (LBL) assembly possess impressive mechanical, electrical, optical, and biological properties desirable in many emerging technologies. Such properties are advantageous in many macro, micro, and nanoscale materials used in numerous applications. The multiple fluid cycles that is required for multilayer preparation makes this promising method for the design and fabrication of customized materials time consuming and often-impractical on a commercial scale.[14,15,16,17,18,19] The abundance of

fluids used in the process make it challenging to couple LBL deposition with other processing steps for materials fabrication. It is quintessential to investigate other means to produce LBL materials that maintain a similar nanoscale control over structure and accelerate the composite buildup for better integration with materials manufacturing.

Formation of the sequentially adsorbed monolayers is traditionally carried out by alternate dipping of a substrate between two reservoirs of oppositely charged macromolecular compounds. An example is found in Figure 1 where a positively charged polyelectrolyte solution and a negatively charged nanoparticle (NP) dispersion is alternatively applied, with intermediate rinse steps that remove excess fluid and loosely adsorbed component.[20,21]

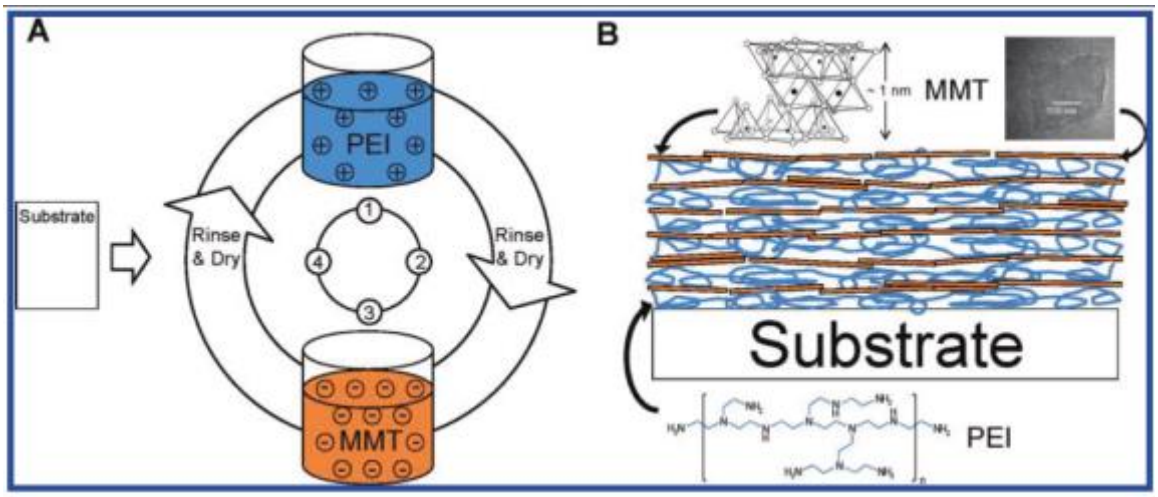

Figure 1. (A) Image of layer-by-layer assembly with cationic polyethylenimine (PEI) and anionic montmorillonite (MMT) and (B) across-sectional view of the resultant nanobrick wall microstructure.

2.1 Layer by Layer Assembly

The Langmuir-Blodgett technique, which applies amphiphilic monolayers from a solution surface onto a substrate with simple dipping, was the precursor to layer-by-layer (LBL) assembly.[22] Iler was the first to perform true layer-by-layer assembly using charged particles.[23] Decher and coworkers later refined and further developed the LBL method,[24,25,26] which is more practical than Langmuir-Blodgett deposition. Ease of layer deposition and tailor ability of film composition has led to numerous applications for LBL assemblies. For many practical applications, accurate thickness characterization and tailoring is necessary. In order for this to occur, the attraction between ingredients, the driving force for the LBL assembly, needs to be studied.[25]

A variety of functional thin films can be produced using the layer-by-layer (LBL) assembly technique, indicating an array of uses.[27,28] Currently, LBL films are being evaluated for a variety of applications that include drug delivery,[29] molecular sensing,[30] solid battery electrolytes,[31] photovoltaics,[32] and membranes.[33] Thin films, typically < 1μm thick, are created by alternately exposing a substrate to positively and negatively charged molecules or particles.

Jang (2008) studied the assemblies of clay and polymer with regard to film growth and gas barrier properties. Thin films of sodium montmorillonite clay and cationic polymer were grown and studied on poly (ethylene terephthalate) film or a silicon wafer. After 30 clay polymer bilayers were deposited, the resulting transparent film had an oxygen transmission rate (OTR) below 0.005 cm3/m2/day/atm. This low OTR, which is unprecedented for a clay-filled polymer composite, is believed to be due to a “brick wall” nanostructure comprised of completely exfoliated clay bricks in polymeric “mortar”. The

growth of polymer and clay assemblies is controlled by altering the pH of polyethylenimine (PEI). Growth, oxygen permeability, and mechanical behavior of clay-PEI assemblies were studied as a function of pH in an effort to tailor the behavior of these thin films. Thicker deposition at high pH resulted in reduced oxygen permeability and lower modulus, which highlights the tailor ability of this system.

Molecular weight,[34,35] temperature,[36,37] and counter ion,[38,39] are other variables that can alter the thickness of LBL assemblies. For high molecular weight polymers, there is little change in thickness, but low molecular weight leads to tight binding and thinner layers.[35] Büscher and coworkers showed that increased deposition solution temperature led to an increase in the thickness of the PAH/PSS system.[37] Van Patten et al. observed a similar temperature effect for poly(diallyldimethylammonium chloride) and poly(styrene sulfonate)[36] Temperature effects are understood in terms of swelling and melting that alters the electrostatic force between oppositely charged polyelectrolytes.

Layer-by-layer assemblies typically grow linearly[40,41,42,43] or exponentially [44,45,46,47] Decher and his collaborators conducted thorough studies on linear growth.[40,41,42,43] Strong cationic polyelectrolytes, such as poly(diallyldimethylammonium chloride) (PDDA) and poly(allylamine hydrochloride) (PAH), were combined with strongly anionic poly(styrene sulfonate) (PSS) for these studies. These polyelectrolytes are fully charged and this “strong” charge density results in relatively extended polymer chains due to self-repulsion. Highly charged polymer chains will result in thinner layers that better cover the substrate surface relative to the more coiled, low charge density polymers. In the case of the PAH/PSS system, small angle X-ray diffraction (SAXS) was used to accurately characterize the buildup of consecutive multilayers.[40]

Ultra-thin organic films with inorganic nanoparticles have broad applications[48,49,50,51] The mechanical properties exhibited by these nanoparticle-filled organic composites are generally worse than predicted.[52,53,54,55,56,57,58,59] The major limiting factors in a composite's mechanical properties are the inability to adequately disperse nanoparticles, the lack of structural control, and the ineffective load transfer from polymer matrix to inorganic nanoparticles.[60] Compared to traditional deposition techniques for inorganic nanoparticle-based ultra-thin films, such as sputtering and vacuum evaporation, LBL assembly has several key advantages, including ambient processing conditions, flexibility in substrate size and shape,[61] and efficient stress distribution throughout the entire composite.[60,62,63] In addition to polyelectrolytes, any type of charged particle, including inorganic molecular clusters,[64] nanoparticles,[65] nanotubes and nanowires,[66,67] can be used in a stabilized form for LBL assembly. The addition of inorganic nanoparticles has been shown to increase the mechanical properties of LBL films due to the immobilization of the high strength material inside the polymer matrix.[63] The characterization of mechanical properties for inorganic nanoparticle-based LBL assemblies is complicated by their small physical dimensions.

Very recently, the Kotov group made a transparent thin film with clay and poly(vinyl alcohol) (PVA) that had a modulus of 100 GPa and tensile strength of 400 MPa.[60] This "plastic steel"[68] is the result of the unique nano brick wall architecture that is only possible with layer-by-layer assembly. Figure 2 highlights the transparency and structure of these unique films. These types of inorganic-organic assemblies can also have interesting transport properties.

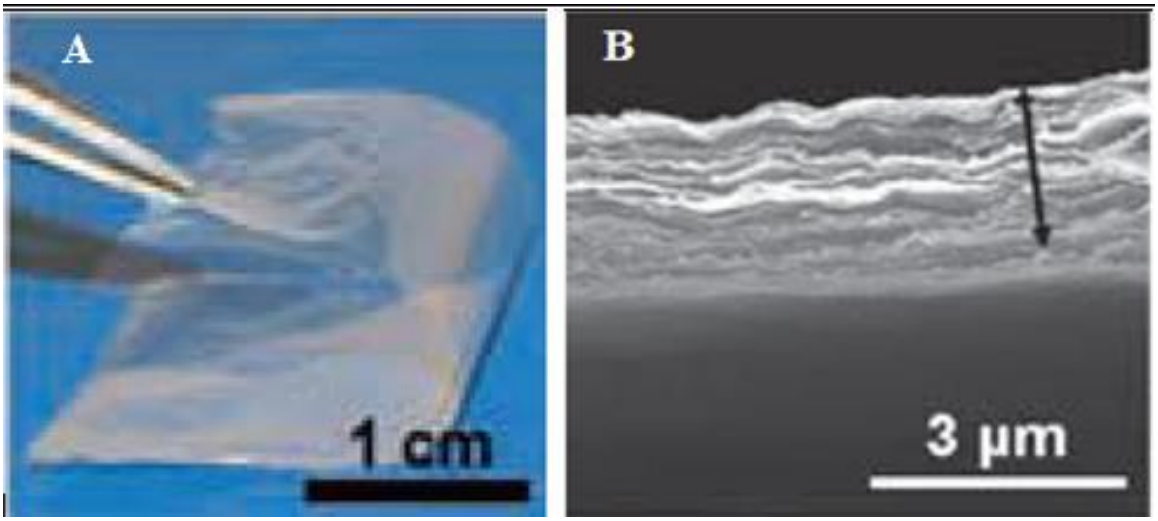

Figure 2. (A) 300-bilayer PVA/MMT free-standing film. (B) SEM cross sectional view of the film.

For the past two decades, the demand for flexible displays and smart windows has been steadily increasing.[69,70,71] One technology used in flexible displays is electrochromism (i.e., color change with applied electric field). Electrochromics are of interest due to their low cost and reasonable contrast in a variety of colors.[72,73,74] Current electrochromic research is focused primarily on thin polymer films.[73] Competing technologies are liquid crystal displays (LCDs) and organic light emmiting diodes (OLED).[75,76] Conventional techniques for producing electrochromic polymer films are electropolymerization and spin-casting with soluble derivatives.[76] Layer-by-layer assembly has several advantages over these techniques, such as simplicity, low cost, and the ability to mix various functional materials in a single film without phase separation.[76]

2.2 Drop on Demand Printing

2.2.1 Drop on Demand Basics

Ever since Joseph Plateau and Lord Rayleigh first generated beads from non-viscous liquid, the study of drops has been utilized in application across a wide range of industries. Three common modes of producing single drops are dripping, continuous jetting and drop-on-demand (DOD) jetting. Dripping occurs when liquid is forced out of a capillary at low flow rates. When the gravitational force acting on the liquid exceeds the capillary force holding the liquid to the surface, pinch off occurs and a drop is formed. In the dripping mode, the rate of drop formation is low since it takes a relatively long time for pinch off to occur. As flow rate is increased through the capillary, transition from dripping to continuous jetting occurs.[77,78,79] The jet will break up due to Raleigh instability;[80] however, drop size will vary significantly.

By introducing a cyclic disturbance, a continuous stream of uniform drops can be generated. The continuous jetting mode, which has been successfully used in inkjet printing, has the advantage of high drop formation rate, but produces drops continuously whether or not they are needed. Consequently, complicated control and recycling systems are required. For the drop-on-demand (DOD) mode, drops are produced only when they needed. A DOD inkjet printer ejects out a tiny amount of liquid by applying a short pressure wave to liquid filling a channel. Under the appropriate conditions, the blob of fluid exiting the nozzle evolves into a single drop.[77]

DOD inkjet printing is an ideal method to deposit micron-size liquid on a substrate in many applications because it is compatible with various materials and easily

controlled by tuning the driving electrical signal.[77] In addition, DOD inkjet printing is a non-contacting process, which means less contamination. It also has high flexibility in materials and substrates, as well as in deposit area, size and shape. Functional materials, especially polymers are more preferably processed from solution. Based on the advantages in depositing liquids, DOD inkjet printing has become a particularly attractive technique, especially for the controlled solution deposition of polymer patterns and delivery of small quantities of functional materials.[81] DOD inkjet printing technology has been applied in many fields from physics, electronics,[82,83,84,85,86] to chemistry,[87,88] tissue engineering,[89,90,91] and biology.[92,93,94]

Drop positioning is achieved by manually locating the printer nozzle above the desired location on the substrate before drop ejection. Drops are formed by propagating a pressure pulse in the fluid held in a chamber behind the printing nozzle. If the pulse exceeds some threshold at the nozzle, a drop is ejected. In the absence of a pressure pulse, liquid is held in place by surface tension at the nozzle. It is normal to also control the static pressure at the nozzle to ensure that the meniscus at the nozzle is stable. In DOD systems, drops are generated at acoustic frequencies (typically 1–20 kHz), and resonances within the chamber behind the nozzle strongly influence pressure pulse propagation and drop generation.[95,96] Drop size is typically equal to the nozzle size, but it is possible to control both drop size and ejection velocity (within a defined range) by management of the pressure pulse used to form the drops.

2.3 Drop Development

Two methods are used to generate the pressure pulse and to promote drop formation and ejection. In thermal DOD printing, a small thin-film heater is located in the

fluid chamber. On passing a current through this heater, the fluid in immediate contact is heated to above its boiling temperature to form a small vapor pocket or bubble. After the current is removed, heat transfer leads to rapid bubble collapse. The rapid expansion and collapse of the bubble generate the required pressure pulse. In piezoelectric DOD printing, the pressure pulse is generated by direct mechanical actuation using a piezoelectric transducer as shown in Figure 3. Similar mechanical actuation has been achieved using MEMS technology and electrostatic forces.[97]

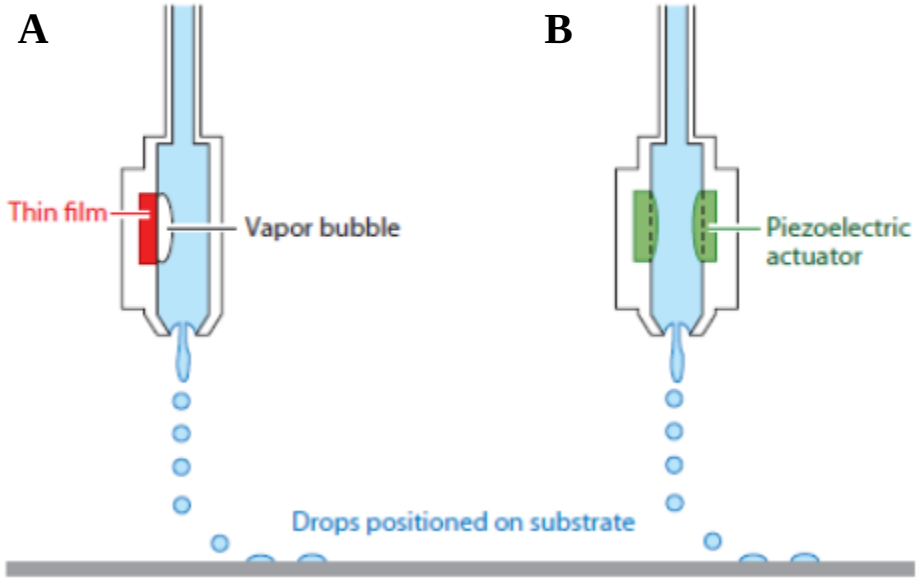

Figure 3. DOD printing. (A) Thermal drop formation, a vapor pocket or bubble is generated by a thin film heater. (B) Piezoelectric drop formation, droplets are formed from a mechanical actuation.

Previous work in the field of drop formation is mainly for Newtonian fluids. Over the last few years, interest in jetting of polymer solutions has received attention. In some cases, the formation and subsequent break up of drops from a nozzle are significantly affected by the addition of polymers to the inkjet ink.

Hoyt and Taylor[98] observed that a pure water stream continuously jetting out of a nozzle generated a number of satellite droplets. There were no satellite droplets near the stream with polymer additive. They assumed it is the resistance of the polymer molecules to elongation, which was responsible for liquid stabilization.

Figure 4 shows the sequence of drop formation observed on a DOD printer. The long extended fluid tail is a characteristic of the DOD process. The drop forms from an initial liquid column that thins to define a leading droplet and the elongated tail or ligament; the final rupture of the ligament can lead to the formation of satellite drops. Often these drops catch up and merge with the leading large drop in flight, prior to impact, in which case their presence is irrelevant. If they are still present at impact, they lead to noncircular impact footprints of the drop, with a deleterious influence on deposit precision, resolution, and accuracy. To facilitate drop merging in flight, it is customary to print at a stand-off distance from the substrate. The appropriate stand-off will also influence drop placement accuracy because drag from air currents in the printing environment can deviate drops from their desired trajectory. To minimize this effect, the stand-off distance is normally set at the minimum to ensure stable single drops.

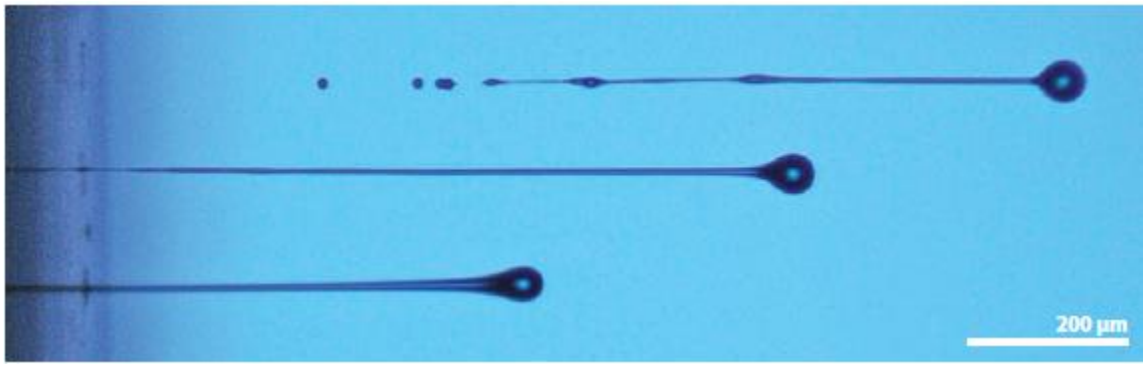

Figure 4. Image showing three drops ejected from a DOD printer at different stages of drop formation.

The generation of droplets in a DOD printer is a complex process. The precise physics and fluid mechanics of the process are still the subject of much research.[99] The behavior of liquid drops can be characterized by a number of dimensionless groupings of physical constants. The most useful are the Reynolds (*Re*), Weber (*We*), and Ohnesorge (*Oh*) numbers, which deal with the fluids density, dynamic viscosity, surface tension, velocity, and characteristic length.

For the drop formation process, the addition of polymer gives elasticity to the liquid, which may greatly affect the process. The degree to which elasticity is important is closely associated with the polymer relaxation time. Attempts have been made to obtain relaxation time both theoretically[100,101,102,103] and experimentally.[104,105]

Christanti and Walker[103, 104,106] investigated the influence of polymer (PEO) on jet stream break up for continuous jetting. They found that both the polymer molecular weight and polymer concentration affect the breakup dynamics. Solutions with higher extensional viscosity and relaxation time are more effective at retarding break up. For dilute solutions, the measured relaxation times are on the same scale as the calculated values from the Zimm model. The drop formation process of dilute polymer solutions for continuous jetting mode is determined by the fluid relaxation time and the disturbance growth rate.

The addition of small amount of polymer has a significant effect on DOD drop formation,[107] suppressing the satellite drop and affecting primary drop speed in some cases. Xu et al. [108] investigated the influence of polymer concentration on DOD inkjet printing for concentrations from dilute through the overlap regimes. They found that the physical behavior of the fluids in drop formation is due to the dominance of viscoelastic

effect within the timescale of the process, in preventing ligament break up at the pinch point compared with a Newtonian fluid of similar viscosity. Measured relaxation times were much longer than those calculated using the relationship reported by Tirtaatmadja, McKinley, and Cooper-White.[103]

2.4 Drop/Substrate Interaction

For most applications, the liquid drop will impact on a substrate, and a subsequent phase change will transform the liquid into a solid. For some applications, this phase change will generate the final desired product, whereas for others a secondary process (e.g., sintering) is required. The liquid/solid phase change can occur by a number of mechanisms, including solvent evaporation, cooling through a transition temperature, gelling of a polymer precursor, and chemical reaction. In all these cases, solidification occurs post deposition. The printed pattern must retain some stability in the liquid state prior to solidification. To fully understand the processes that occur between the printed drop and the substrate prior to attaining the desired structure, we must identify the interactions that occur between the substrate and the fluid drop prior to solidification.

2.5 Drop Impact and Spreading

The behavior of a liquid drop on impacting a solid surface is controlled by a number of physical processes and can be driven by inertial forces, capillary forces, and gravitational forces. The important dimensionless groupings are the Reynolds, Weber, and Ohnesorge numbers, as with drop generation.

Typical fluids used for inkjet printing have a density close to 1000 kgm^{-3}, a surface energy below 0.1 Jm^{-2}, and in DOD printing the drops have diameters $<100\ \mu$ m. At these small length scales, $Bo<<1$; hence gravitational forces can be neglected. The

dominant forces will be inertial and capillary. Schiaffino & Sonin[109] considered the impact of relatively low Weber number drops on a solid surface. Although their analysis was for solidifying drops, the initial stages after drop impact should be the same for all impacting fluids. They proposed that drop behavior on impact can be divided into two regimes: impact driven, in which the inertial forces dominate, and capillarity driven, in which initial drop velocity is unimportant and the transition in behavior occurs at a critical value of the Weber number. These authors characterized the resistance to spreading in terms of the Ohnesorge number, defining regimes as almost inviscous and highly viscous. The initial stage of the interaction between an inkjet-printed drop and a substrate is impact driven in a region of relatively inviscous behavior.

Yarin[110] reviewed the behavior of impacting liquid drops in the velocity range 1–30 ms^{-1} and size range 100–3000 μ m; this is sufficiently close to the regime of inkjet printing to provide a useful reference. Drop impact behavior can be conveniently divided into a number of timescales determined by the dimensionless time after impact, $t* = t(v/d0)$, where $d0$ is the droplet diameter and v is droplet velocity.[111] The initial impact stage is governed by kinematic behavior and has a duration of approximately $t^* = 0.1$ (or <1 μ s for the dimensions and velocities appropriate for inkjet printing). This is followed by impact-driven spreading, recoil, and oscillation. At small values of t^*, viscous forces damp the spreading and oscillations, and surface tension forces become more important in controlling behavior. At later stages the capillary forces begin to dominate until, at t^* ~10–100 (0.1–1 ms), spreading is fully controlled by capillarity, and further extension occurs proportional to $t^{1/10}$.[112] Spreading continues and approaches true equilibrium at t^* >1000. The sequence of these processes is shown in Figure 5.[113]

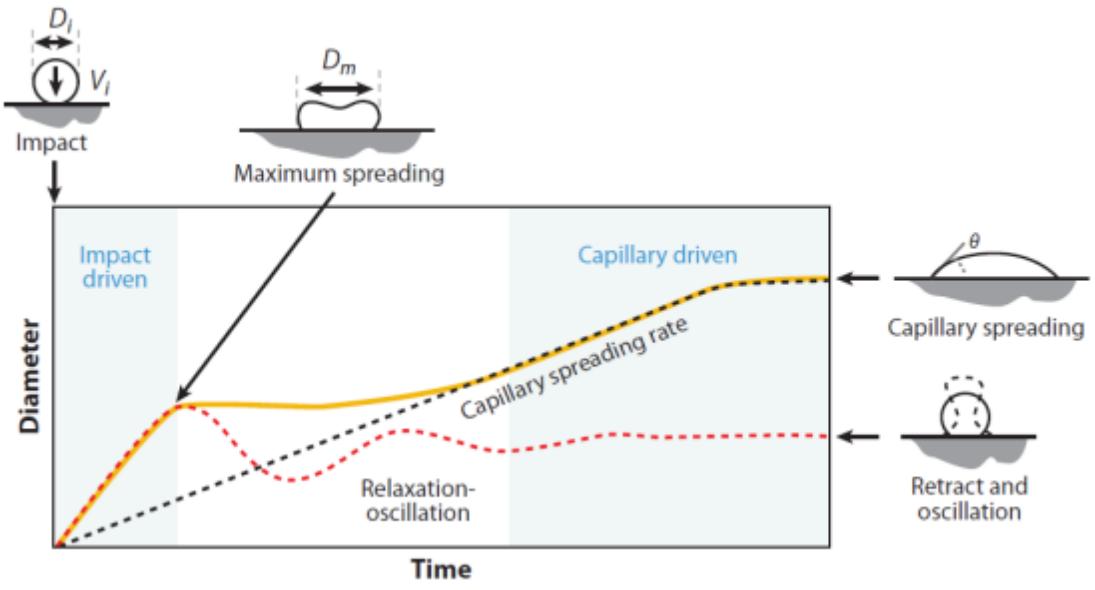

Figure 5. The image shows the sequence of events that occurs after droplet impact on a substrate. Initial impact is followed by a series of damped oscillations before capillary-driven flow occurs. θ is the contact angle, D_i is the initial droplet diameter, D_m is the maximum radius to which a droplet spreads during impact, and *Vi* is the droplet velocity at impact.

The final spread drop will have a contact diameter or footprint, d_{con}, determined by its volume and the equilibrium contact angle, θ_{eqm}. The drop footprint increases with decreasing contact angle and is approximately $3d_0$ at a contact angle of 10°. The contact angle is very important in controlling the final shape of a printed drop and patterns built up from the interaction of drops. As a drop spreads after impact, it advances over a dry surface. In the production of films and patterns, drops may contact and interact with other drops. This interaction may lead to flow reversals, and in such cases, the receding contact angle becomes important. Receding contact angles are also important if drop solidification occurs by solvent evaporation, in which case decreasing drop volume

would be expected to lead to the drop footprint decreasing in area. Drying droplets of solutions (especially polymer solutions) often show contact line pinning from solute deposition; this, combined with increased solvent evaporation rate toward the edge of the droplet, can lead to solute deposition in a ring at the contact line. This phenomenon is known as the coffee stain effect.[114] When contact line pinning occurs, the receding contact angle will decrease during evaporation and will tend toward zero.

2.6 Drop Coalescence and Pattern Stability

Conventional graphics printing requires patterns made up of isolated drops to produce a pixilated image. A key distinguishing feature between materials printing and graphics printing is that, for many materials applications the drops are required to overlap to form continuous features. Thus, a key behavior is the interaction of spread or spreading droplets on a substrate to form stable liquid beads or lines and more complex 2-D patterns. 3-D structures are produced by overprinting sequential layers, but in this case, a drop interacts with a solidified deposit and behaves qualitatively the same manner as deposition on a substrate. Inkjet printing forms liquid beads through the overlap of adjacent spread drops. If there is no overlap of drops, there is no mechanism for the formation of liquid beads. Two overlapping drops will tend to coalesce, and a train of overlapping drops will form a bead, if there is significant contact line pinning.

2.7 Barrier Films

2.7.1 Tortuous Path Theories

Inorganic nanoparticles can block the diffusion of gases or liquids in a permeable (e.g., polymeric) matrix. If the inorganic nanoparticles are impermeable, then the

diffusing molecules have to go around them. This assumption leads us to the tortuous pathway theory. Equation 1 is an initial approximation:

$$PF / PU = \varphi_P / \tau \qquad (1)$$

Where PF and PU are permeability of the filled and unfilled polymer, respectively, φ_P is the volume fraction of the polymer,[115] and τ is the tortuous factor, which is the distance a molecule must travel to get through the film divided by film thickness. A required assumption is that the fractional area occupied by the polymer in any cross section is equal to the volume fraction of the polymer. Permeability is independent of thickness, which means PF/PU is not proportional to thickness.

Nielsen created the formal tortuosity theory as shown in equation 2:[116]

$$\tau = 1 + (L/2W)\varphi_F \qquad (2)$$

Where L is the length of a face of a filler particle, W is the thickness of filler plates, and φ_F is the volume fraction of filler. A large aspect ratio (L/W) produces decreased permeability if the particle lies with its largest dimension parallel to the substrate surface. Figure 6 shows an image depicting a tortuous path.

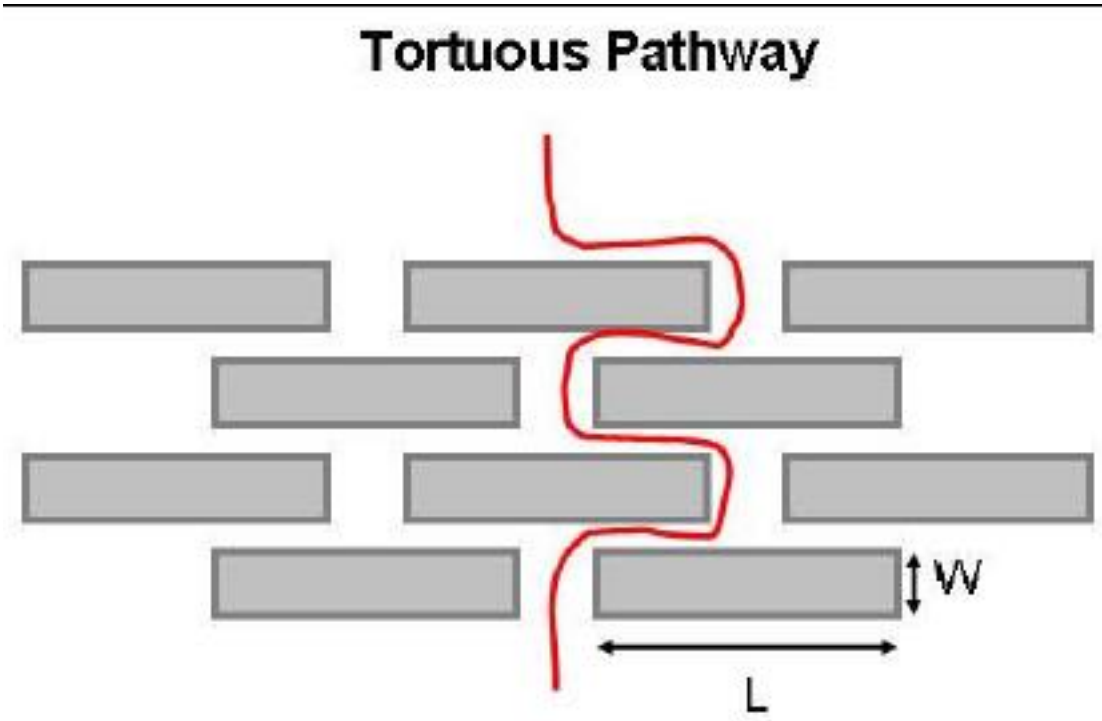

Figure 6. Image showing the path of diffusing a molecule through a tortuous pathway with impermeable parts.

Equation 3 is Cussler's model for diffusion coefficient:[117]

$$D = \frac{D_0}{1 + \alpha^2 \varphi^2 / (1 - \varphi)} \qquad (3)$$

Where D0 is the diffusion coefficient without impermeable flakes, D is the composite diffusion coefficient, α is the flake aspect ratio, and φ is the volume fraction of impermeable flakes. Equation 4 has been verified experimentally[118,119,120,119,120] and through Monte Carlo simulations.[118] The second term in the denominator of Cussler's equation is the resistance to diffusion of the tortuous path around the flakes, known as a "wiggle". The square of α and φ reflects the increased diffusion distance and the reduced

cross-sectional area between the flakes. This wiggling is the most important factor of the increased resistance in flake-filled barrier membranes.[116,121,122,117,118]

Cussler and coworkers later improved their own model~~, which~~ takes into account the resistance to diffusion of the slits between adjacent flakes in the same horizontal plane and the constriction of the solute to pass into and out of the narrow slits.[123]

By combining the diffusion flux and diffusion coefficient models, Cussler and coworkers were able to determine the permeability of flake aligned composite coatings[124] and polydispersed flake-based barrier films.[125]

Fredrickson et al. developed a barrier model that includes several additional assumptions:[126] the matrix is homogeneously filled with impermeable flakes, the flakes are disks, and the directional vector of the flake surface is parallel to the diffusion direction. Equation 4 represents this model:

$$D=D_{\parallel}\hat{u}\hat{u}+D_{\perp}(\delta-\hat{u}\hat{u}) \qquad (4)$$

Where D is the diffusion tensor and $\hat{u}$ is a directional vector of the flake surface. $D_{\parallel}$ and $D_{\perp}$ denote diffusion coefficients parallel and perpendicular to $\hat{u}$ and δ is the unit tensor.

When the flakes have a very small aspect ratio and perfect alignment, $D_{\perp}$ is the same as D_0 (the diffusion coefficient of the neat matrix). The final assumption is that diffusivity in the matrix is independent of the presence of particles.

The critical difference between Cussler's model and Fredrickson's model is the shape of impermeable flakes creating a difference in geometric factors. If the flakes are polydispersed in size, then the geometric factor has little influence.[123] These tortuous path theories have laid the groundwork for the current understanding of platelet filled polymer

composites used in barrier applications. The polymer associated with the clay surface behaves differently than bulk polymer and can contribute positively to barrier properties.

2.8 Filled Polymers

Inorganic nanoparticle–filled polymer composites have relatively low density, improved barrier properties, and enhanced mechanical properties.[127] In addition to these benefits, inorganic nanoparticle–filled polymer composites have recently been shown to exhibit excellent flame retardant behavior.[128,129] Adding impermeable inorganic nanoparticles to bulk polymer films is a common route to reduce oxygen transmission rate (OTR).[130,131,132] Clay platelets are especially effective for gas barrier due to their nano thickness (~1nm) and large aspect ratio ($10 < l/d < 2000$, depending on type). Giannelis and coworkers have extensively studied the synthesis and characterization of impermeable nanoparticle-filled oxygen and moisture barrier.[125,126,127] They used melt intercalation of polymer,[133] which can be applied to a non-polar polymer matrix, such as polystyrene, or to a strongly polar polymer matrix, such as nylon. An intercalated structure has a few polymer chains in between the silicate layers, in the case of clay platelets. Disordered systems have exfoliated and dispersed silicate layers in the polymer matrix, as shown in Figure 7.

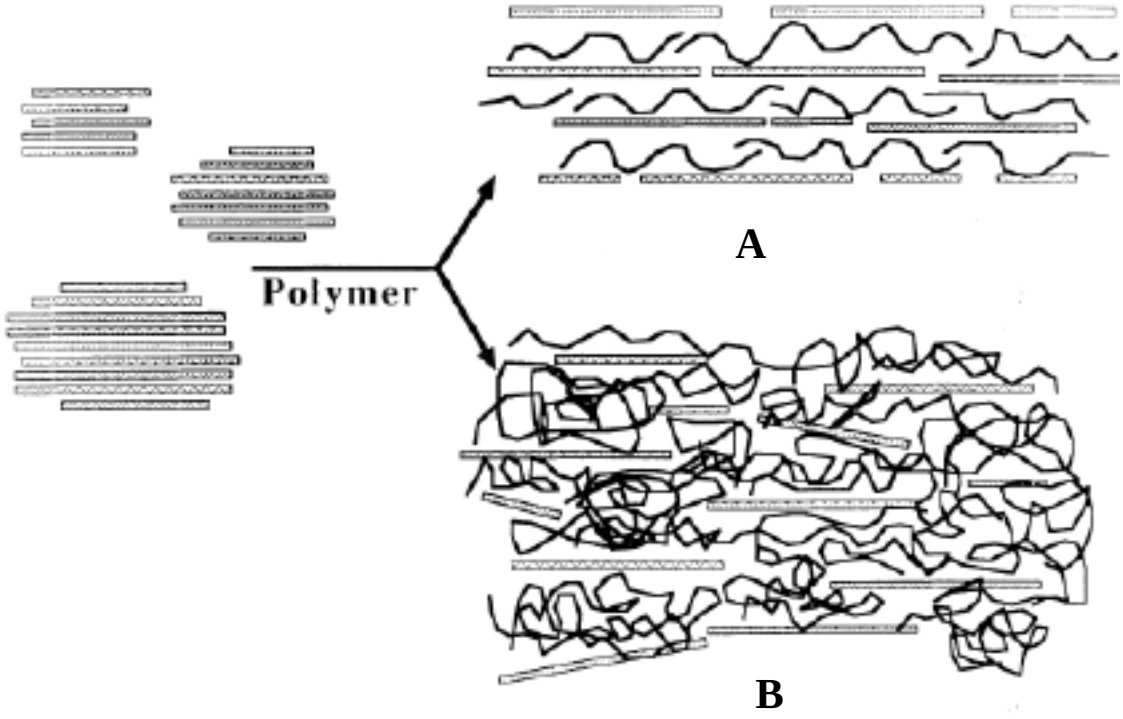

Figure 7. Image showing layered silicates-filled polymer composites can have an intercalated (A) or disordered structure (B).

Montmorillonite layered silicates (MLS) are ceramic platelets with a high aspect ratio,[134] typically >100nm in diameter and 1nm thick. This high aspect ratio creates a tortuous path for gas molecules moving through the polymer matrix, which creates a large diffusion length that lowers the permeability.[114,135] Unlike SiOx films and polymer multilayer films, clay-filled polymer composites typically suffer from poor transparency and relatively high OTR. Most systems show an OTR or permeability reduction of 1 to 100%,[127,129,130,136,137,138] but a few show an order of magnitude improvement.[139]

Prior research conducted by Beall et al. has proven that water soluble polymers can be utilized to surface modify smectites/clays via ion-dipole bonding. The most common of these polymers includes polyvinylpyrrolidone (PVP), polyvinylalcohol

(PVA), and polyethylene glycol (PEG). Figures 8 is the basic structure for each of these polymers, Figure 9 is the bonding action of polymers and MMT nanoclays.

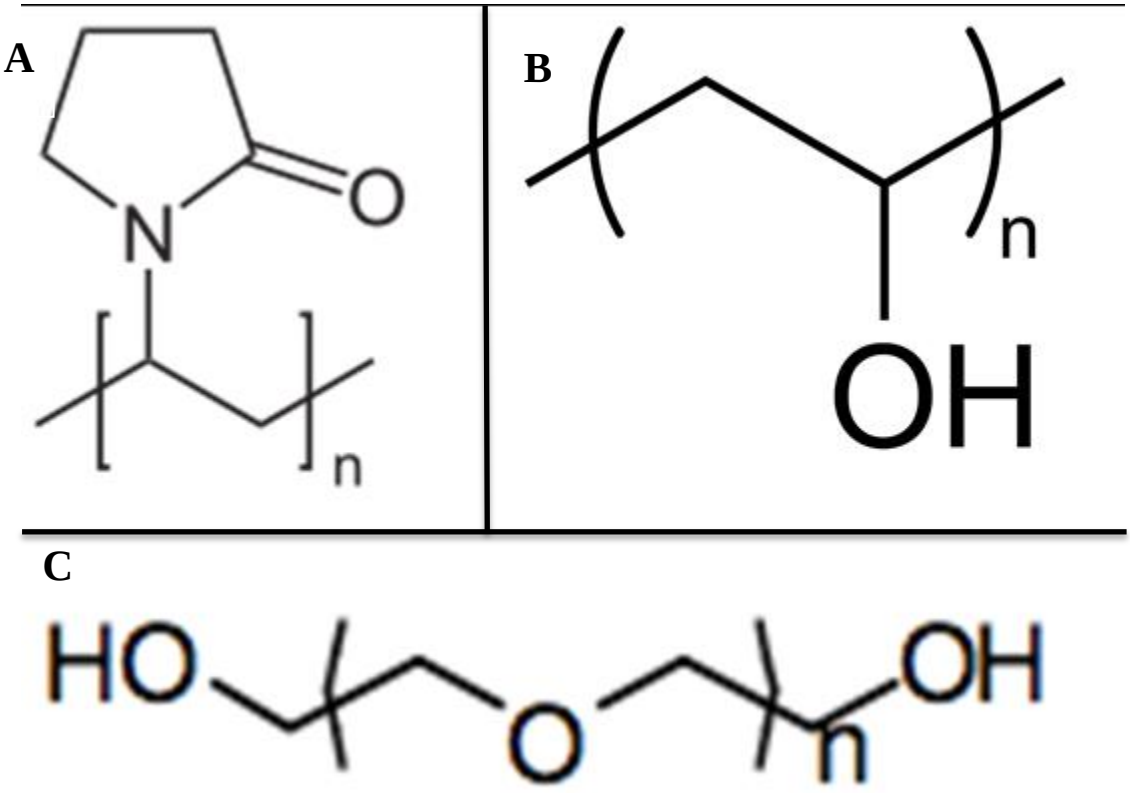

Figure 8. Image of basic polymer structures. (A) is polyvinylpyrrolidone (PVP), (B) is polyvinylalcohol (PVA), and (C) is polyethylene glycol (PEG) structures.

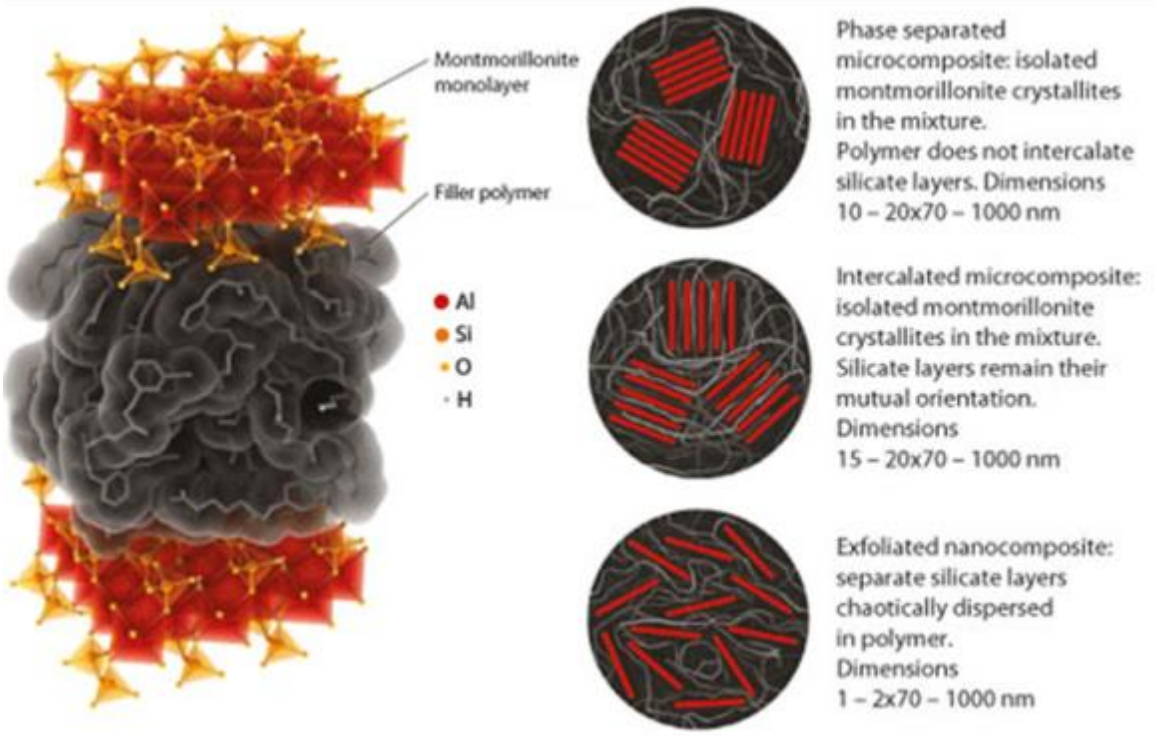

Figure 9. Depiction of a polymer bonded to MMT nanoclay particles.

The polar group of PVP is a carbonyl, for PVA it is an alcohol, and the PEG has an ether. Figure 10 shows a molecular model of PVP bonded to the clay. It can be seen that the bulkiness of the pyrrolidone ring causes the polymer backbone to be fairly linear. It also appears that once the rings on one side of the polymer bonds then the rings on the opposite side have difficulty bonding to another clay plate.

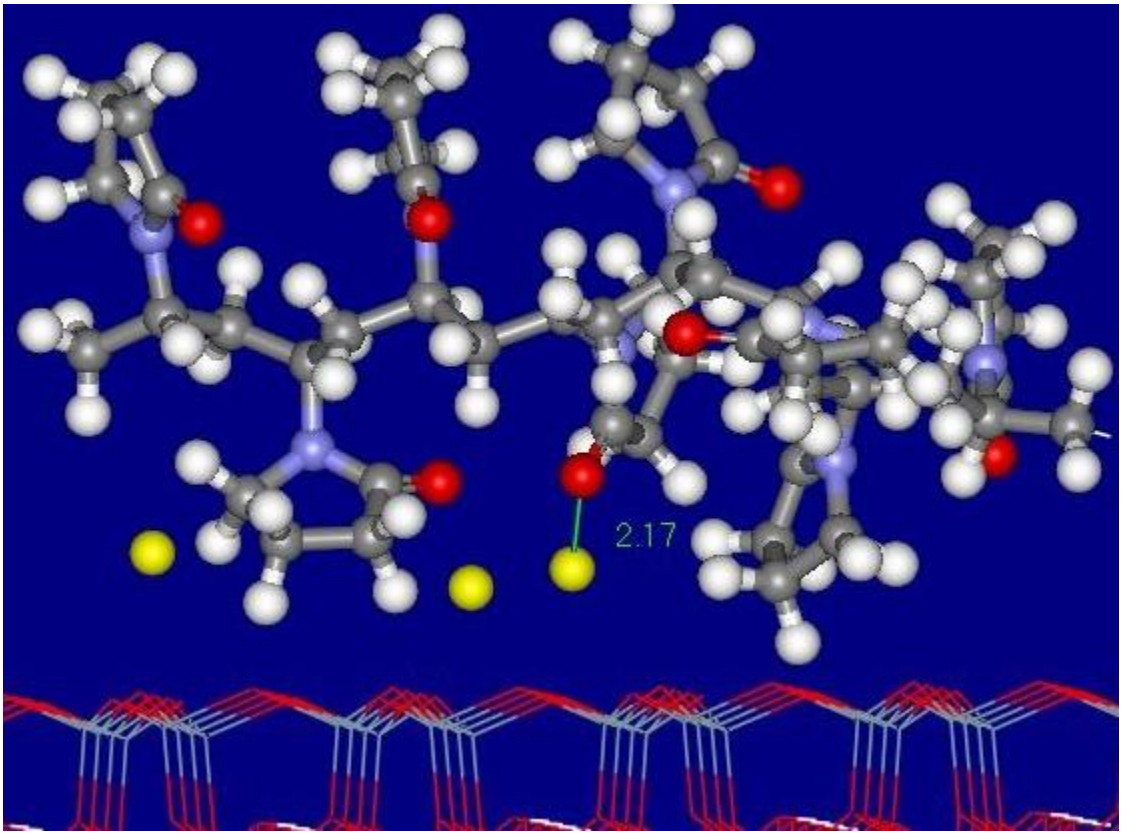

Figure 10. Molecular model of PVP bonded to MMT clay.

This strongly influences the intercalation/exfoliation character of this polymer as shown in Figure 11. A loading of PVP increases the d-spacing has steps. The first step is for one layer of PVP in the gallery. The second step is a bilayer followed by a trilayer. As you add even more PVP, the clay can be completely exfoliated.

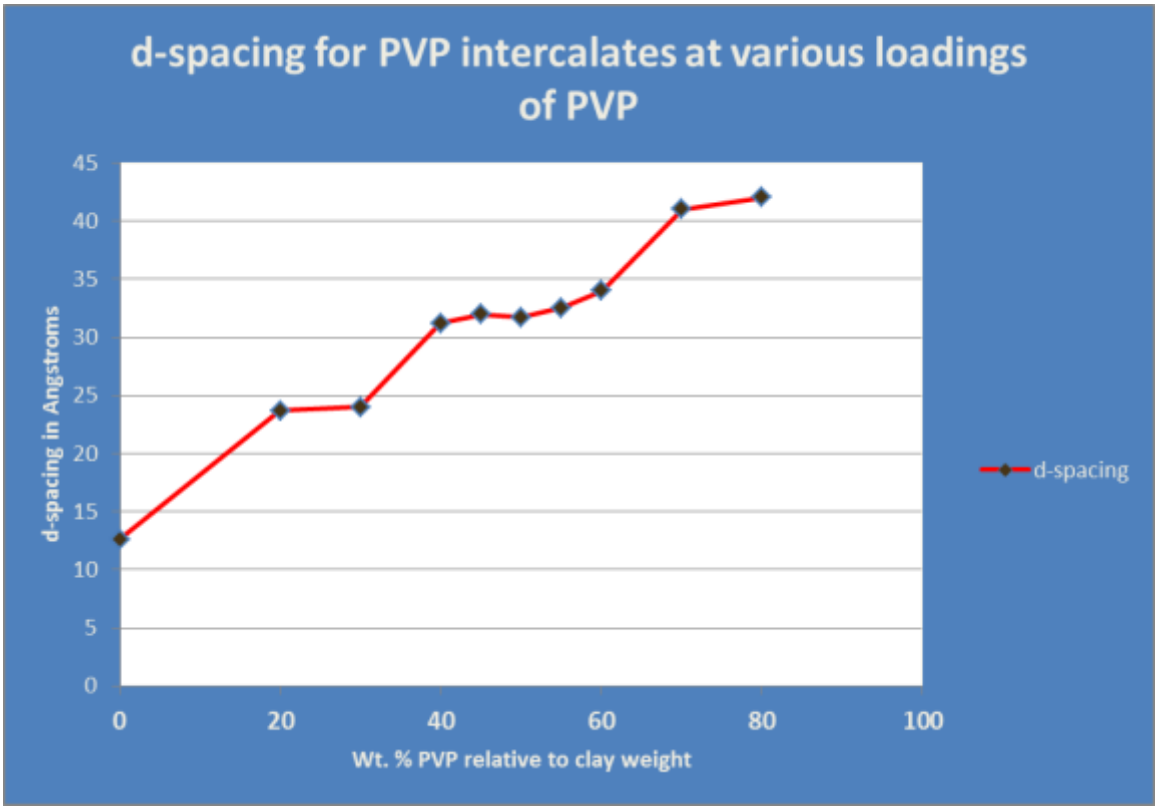

Figure 11. Graph indicating the steps in d-spacing for PVP intercalates at various loadings of PVP.

When comparing PVP to PVA and PEG on a clay with a charge density of 95 meq/100 g the other two polymers did intercalate but will form bilayers. The literature indicates studies were conducted to explore this phenomenon. A series of different charge density clays were utilized to determine if bilayer structures could be formed with the three polymers. The clays studied had charge densities of 75, 95 and 143 meq/ 100 g. Table 1 is a compilation of the results. In all three clays, PVP would form the bilayer structure. The PEG never formed the bilayer and PVA would form the bilayer for low charge but would form a mixed structure at medium charge and never at the high charge.

Table 1. Results of bilayer formation from different charge density clays and polymers.

Polymer	Low Charge Clay	Medium Charge Clay	High Charge Clay
PEG	No	No	No
PVA	Yes	No/Yes	No
PVP	Yes	Yes	Yes

This behavior relates to the flexibility of the three polymers. PEG is the most flexible and can bond easily to both sides of the gallery. PVA is slightly less flexible and bonds across the gallery if charge density is high enough.

CHAPTER 3

Experimental Methods

This work established the capabilities of 3D LBL printed films for use in creating gas barrier films, mainly oxygen, to be used in commercial applications such as food and beverage packaging. The barrier properties and functionality of the films were established. Comparative data to the commercially used dip and rinse LBL materials were collected and reported.

3.1 Establishment of Parameters for Drop on Demand Printing

Ink solutions consisting of multiple polymer materials and deionized water in varying weight percentages were prepared to determine which concentrations would print and disperse the best on a Mylar substrate. The starting percentage of each material by weight varied depending on the type of material used. In the beginning, only one layer of the solution was printed and analyzed. The print speed, drop size, drop spacing, ink solution temperature, and substrate temperature were varied to obtain the best results for each concentration. The subsequent films were analyzed using materials characterization techniques such as optical microscopy, SEM, AFM, a surface profilometry, and oxygen permeability testing. The permeability of the films was analyzed using a Mocon Ox-Tran model 2/60, (See Appendix VI for equipment details).

3.2 Establishment of Weight % of Material Required for Printing

Due to the wide use and known oxygen barrier properties of the materials, it was determined that the first ink solution would be a mixture of polyvinylpyrrolidone (PVP) and deionized water. Weight percentages for the solution were determined based on quantities established in the literature review, and thus initial amounts were based on

previous research. This research started by formulating a batch of 120 grams of 0.5% PVP in deionized water.

An electronic scale was used to measure the ingredients of each solution. A test beaker was first placed on the scale and the reading was zeroed. Once the total amount (in grams) of solution to be produced is determined (arbitrarily), the amount of ingredient needed can be calculated (based on desired weight percentages). To insure the correct amount of a certain ingredient was used, the total mass value for the mass of the ingredient plus the initial mass reading on the scale was calculated prior to any weights being taken. Once the ingredient was added to the beaker, the weight was verified against the calculation. It was found that it is best to start by adding water first and the polymer second. When the polymer was added first, it tended to stick to the side of the beaker. The solutions were submersed in a sonicator bath on low for 30 minutes.

The solution was left in an airtight storage container overnight to allow any residual undissolved particles to dissolve/dissperse and allow the sample to return to room temperature. To test printability, the container was re-mixed by shaking prior to testing, and a portion (1.5 mL) was extracted and inserted into the print cartridge.

The solutions were extracted using equipment that came with the cartridge, which was a FUJIFILM Dimatix DMC-11601 print head as seen in Figure 12.

Figure 12. Image of a Dimatix DMC-11601 print head and ink solution cartridge

It is a two-part cartridge consisting of a reservoir and a print head. The nozzle plate is located on the bottom of the print head and is made of silicon. It contains sixteen nozzles spaced 254 microns apart. Each nozzle is approximately 20 microns in diameter. It can generate drop volumes as small as 1 picoliter. All solutions were printed onto standard 8.5" by 11" Mylar film sheets. The film is manufactured by DuPont and is used primarily for transparencies by ink jet and laser printers.

After the solution had been inserted into the printer cartridge, it was taken to the printer for testing. The printer used was a DMP 2831 Dimatix Materials printer as seen in Figure 13, which is used by developers of printable functional fluids and research and development. It allows for high-precision jetting of all kinds of functional fluids on any surface including plastic, glass, metal sheets, silicon, membranes, gels, thin films and paper.

Figure 13: Image of a Dimatix DMP-2831 Materials Printer

The cartridges used were made specifically for the printer. There are default settings that can be adjusted, allowing for all, some, or only one jet/nozzle to print at one time as seen in Figure 14, (See Appendix V for more details on settings and functions).

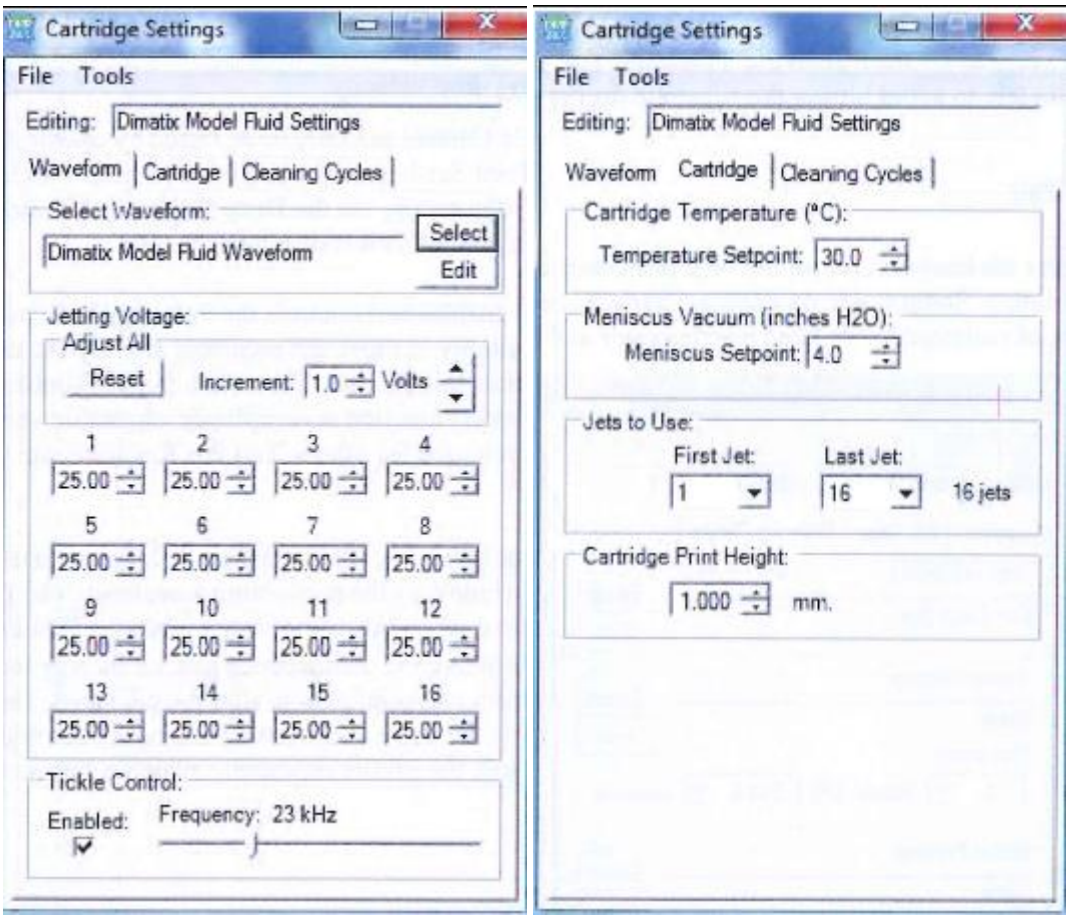

Figure 14. Image from a Dimatix DMP-2831 Printer cartriage settings screen.

Drop formations are observed using the Drop Watcher feature in the printer as seen in Figure 15. The printer software allows you adjust the refresh rate to provide images of the droplets forming and dropping several times per second. (See Appendix II for more details on Drop Watcher operation).

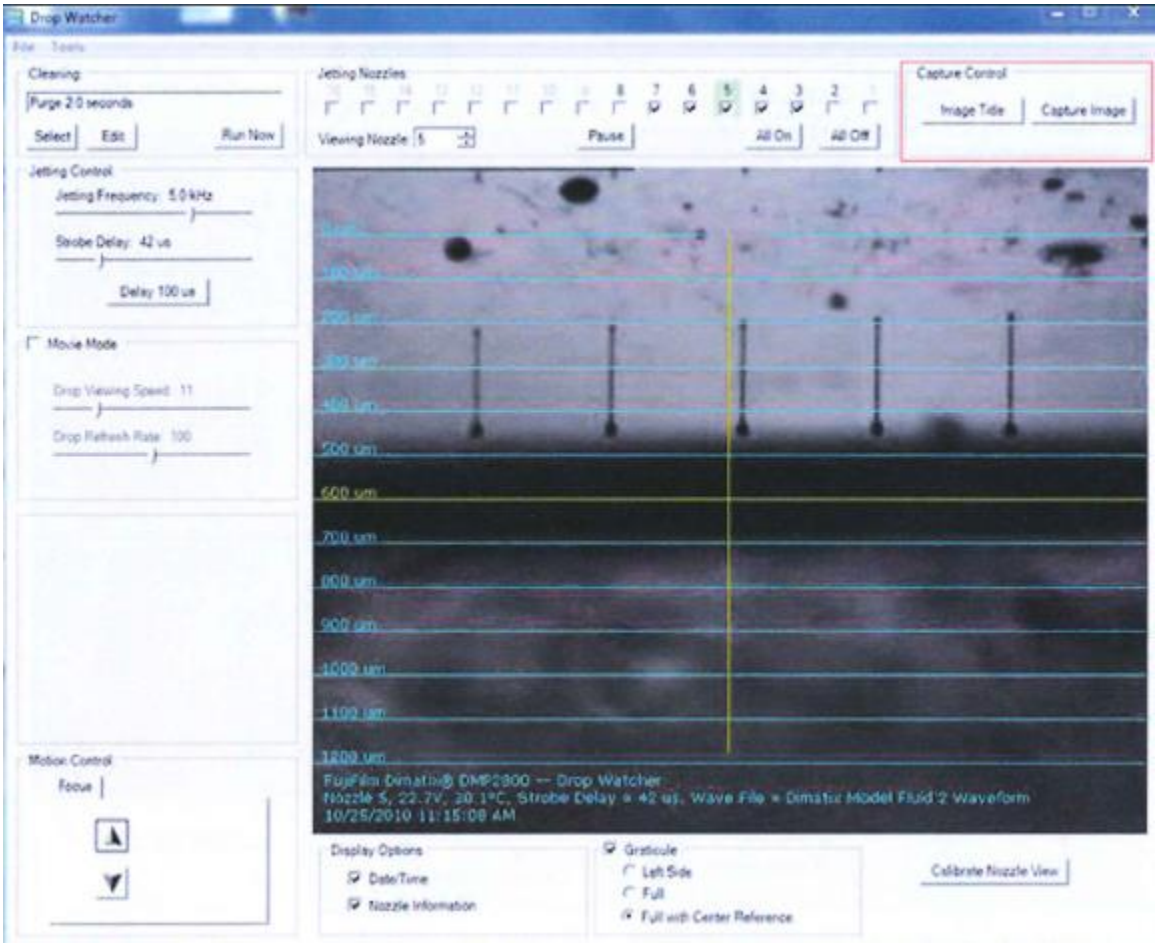

Figure 15. Image from a Dimatix DMP-2831 Printer Drop Watcher screen.

This process for creating solutions was repeated for polyvinylalcohol (PVA) and polyethylynglycol (PEG). A solution of (MMT) clay and de-ionzed water was determined for use in formulating a layered film. For the solution (graphenol) made with graphene, humic acid (rather than DI water) was used.

3.3 Establishment of Drop Formation and Rate

3.3.1 Formation of Solution

Once the initial solution of PVP and DI water (0.5% by weight) was formulated, it was tested in the printer. The default settings were used for the first run of tests. The 0.5% PVP solution was found to be too viscous, and would not form a drop. After this

observation, the parameters were adjusted to determine the best printing configuration, including the number and spacing of nozzles, the preferred print speed, and the correct waveform. No changes to the printing parameters yielded any drop formation at the 0.5% level.

The entire formulation and testing process was repeated with solutions of 0.4%, 0.3%, and 0.2% PVP by weight. The 0.4% solution produced a few droplets, but plugged up the nozzles almost immediately. The 0.3% produced more droplets, but caused blockage in the nozzles over time. The 0.2% solution was able to generate consistent printing. Multiple films were printed varying the drop waveform, size, spacing, speed, and number of nozzles to determine the best parameters for each solution.

For the PEG, the process suggested a 0.2% weight by volume. PVA was found to be slightly more viscous, and required a solution of 0.1% weight by volume. The polymer was very tacky, causing suspended tails to form on the print head. The MMT clay produced good results at a 0.2% solution. Graphenol functioned well at 0.2% weight by volume. There was a difference in variation in voltage and waveform settings between PVP, PEG, and Graphenol. These differences are presented in Table 2, along with all of the final parameter settings for each solution.

Table 2. Settings used to print films comprising of PVP, MMT, PVA PEG, and Graphenol.

PVP PRINT SETTING

Wave Form	Cartidge Settings	Cleaning Cycle	Drop Spacing
Default Dimatix Model Fluid settings	Temp = 27C	Start of Print = Spit Purge Spit	20.0 um
Jetting Voltage = 27.0	Meniscus Vacuum = 3	During Print = Run every 300 sec	
Tickle Control = 23.0 kHz	Jets (Nozzles) = 6-8	End of print = Spit Purge Spit	
	Print Height = 1.0 mm	While idle = None	

MMT PRINT SETTING

Wave Form	Cartidge Settings	Cleaning Cycle	Drop Spacing
Default Dimatix Model Fluid settings	Temp = 27C	Start of Print = Spit Purge Spit	24 um
Jetting Voltage = 30.0	Meniscus Vacuum = 2	During Print = Run every 300 sec	
Tickle Control = 23.0 kHz	Jets (Nozzles) = 6-8	End of print = Spit Purge Spit	
	Print Height = 1.0 mm	While idle = None	

PVA PRINT SETTING

Wave Form	Cartidge Settings	Cleaning Cycle	Drop Spacing
Custom Wave Settings	Temp = 27C	Start of Print = Spit Purge Spit	28 um
Jetting Voltage = 36.0	Meniscus Vacuum = 1	During Print = Run every 60 sec	
Tickle Control = 23.0 kHz	Jets (Nozzles) = 6-8	End of print = Spit Purge Spit	
Slew Rate = 0.70	Print Height = 1.0 mm	While idle = None	
Duration = 2.90 us			

PEG PRINT SETTING

Wave Form	Cartidge Settings	Cleaning Cycle	Drop Spacing
Custom Wave Settings	Temp = 27C	Start of Print = Spit Purge Spit	24 um
Jetting Voltage = 32.0	Meniscus Vacuum = 2	During Print = Run every 90 sec	
Tickle Control = 23.0 kHz	Jets (Nozzles) = 6-8	End of print = Spit Purge Spit	
Slew Rate = 0.65	Print Height = 1.0 mm	While idle = None	
Duration = 2.50 us			

GRAPHENOL PRINT SETTING

Wave Form	Cartidge Settings	Cleaning Cycle	Drop Spacing
Default Dimatix Model Fluid settings	Temp = 27C	Start of Print = Spit Purge Spit	28 um
Jetting Voltage = 30.0	Meniscus Vacuum = 2	During Print = Run every 90 sec	
Tickle Control = 23.0 kHz	Jets (Nozzles) = 6-8	End of print = Spit Purge Spit	
	Print Height = 1.0 mm	While idle = None	

CHAPTER 4

Creation of Films

4.1 Layering of Materials

The generation of reproducible drops for the materials enabled the creation of testable films. Films were created by placing layers of materials onto a Mylar substrate. The number and variation of layers for each material are discussed below.

4.1.1 PVP and MMT Clay

The first film produced using the ink jet DOD printer was PVP only. Within the printer is the ability to generate a template for placement of material during printing, (See Appendix IV for template creation details). Initially, the template consisted of six (6) 2.5" x 2.5" squares in a 3 x 2 matrix on one sheet of Mylar substrate. A 2.5" square was used because the Mocon 2/60 testing equipment used to test the permeability of the films holds samples approximately that size. One layer of polymer was printed using the six square template. The template was modified to print another layer on only five (5) squares, leaving one (1) square with a single layer of PVP, and five (5) with two layers. It was modified again, producing four (4) squares with three (3) layers of material. This process was repeated until each square had a varying number of layers of PVP (1-6 layers). All of the patterns created were saved and used on the remaining ink solutions.

The samples were created using various solution temperatures on the different levels. The first layer was applied at room temperature. Successive layers were placed at gradually higher temperatures up to 45º C. Visual inspection at this stage indicated temperature had a negative impact on drop dispersion due to molecular bonding, and the decision was made to apply all layers that would be tested at room temperature.

The second round of film production used MMT nanoclay. There were six (6) samples of film produced in the same manner as the PVP above. Initially, a template of six squares was used, adjusted each print run down one (1) square, until six (6) samples had been created. Each sample varied from 1-6 layers of MMT clay, which could then be tested for permeability. This produced a total of twelve (12) samples, each with a different number of layers of each material (PVP and MMT clay). Permeability analysis was run on all twelve (12) samples. This established a base permeability rate (CC/M2/24H/MIL) for the PVP alone and for the clay alone at different thicknesses.

After each had been measured individually, a film containing both materials was created. The same initial six (6) square template was used. One (1) layer of PVP was placed on all six (6) squares, followed by one (1) layer of MMT clay on all six (6) squares. The template was then adjusted as in the previous process to place a second layer of PVP and MMT clay on five (5) squares, a third layer of both materials on four (4) squares, a fourth layer on three (3) squares, etc., until there were six (6) alternating bilayers of PVP and MMT clay on the last sample (12 individual layers total). This produced six (6) samples, which were then tested for permeability and characterized.

4.1.2 PVA and MMT Clay

The next round of printing on the DOD ink jet printer was used to analyze the PVA solution. The same six (6) sample production method was used for assessing only PVA, same as the single material PVP and MMT clay samples. A template of six individual squares was used, and was to be adjusted down one (1) square each print run until six (6) individual samples ranging from one layer to six layers had been created. The drops beaded up and did not disperse on the Mylar substrate (as seen through the fiducial

camera on the printer), see Figures 16 &17. (See Appendix V for more details on camera).

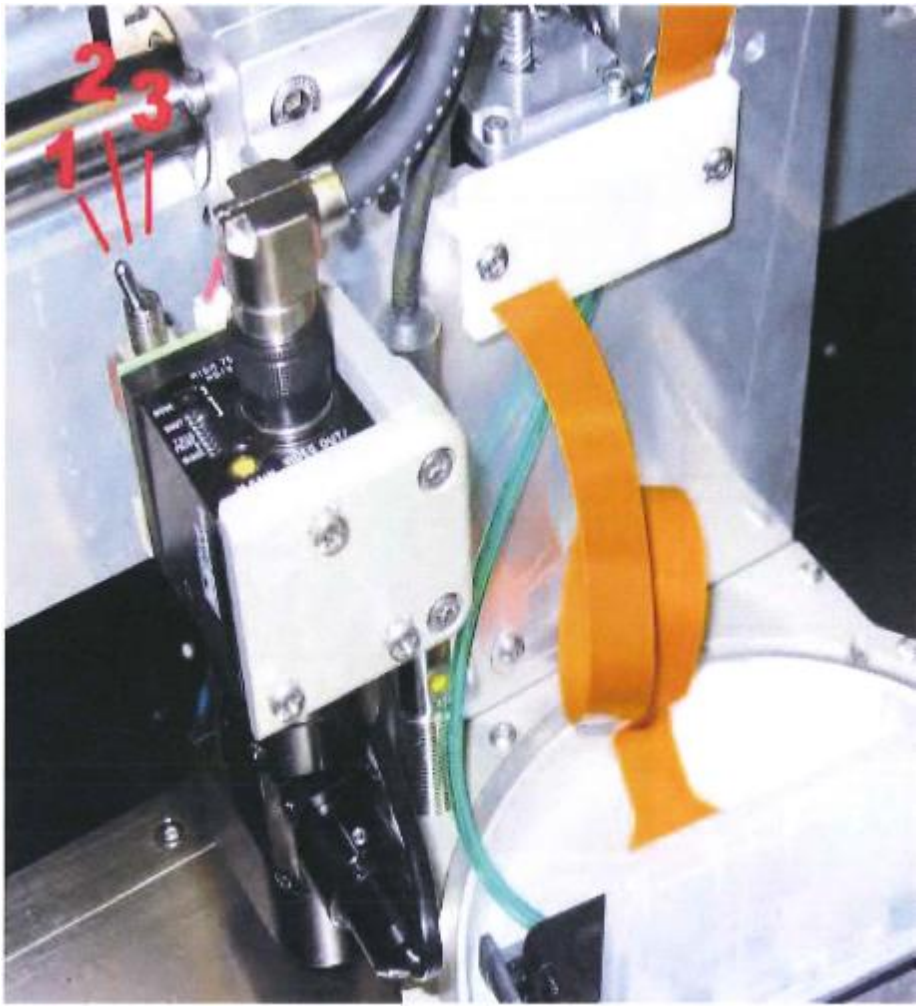

Figure 16. Image of a fiducial camera mounted on a Dimatix DMP-2831 DOD Printer.

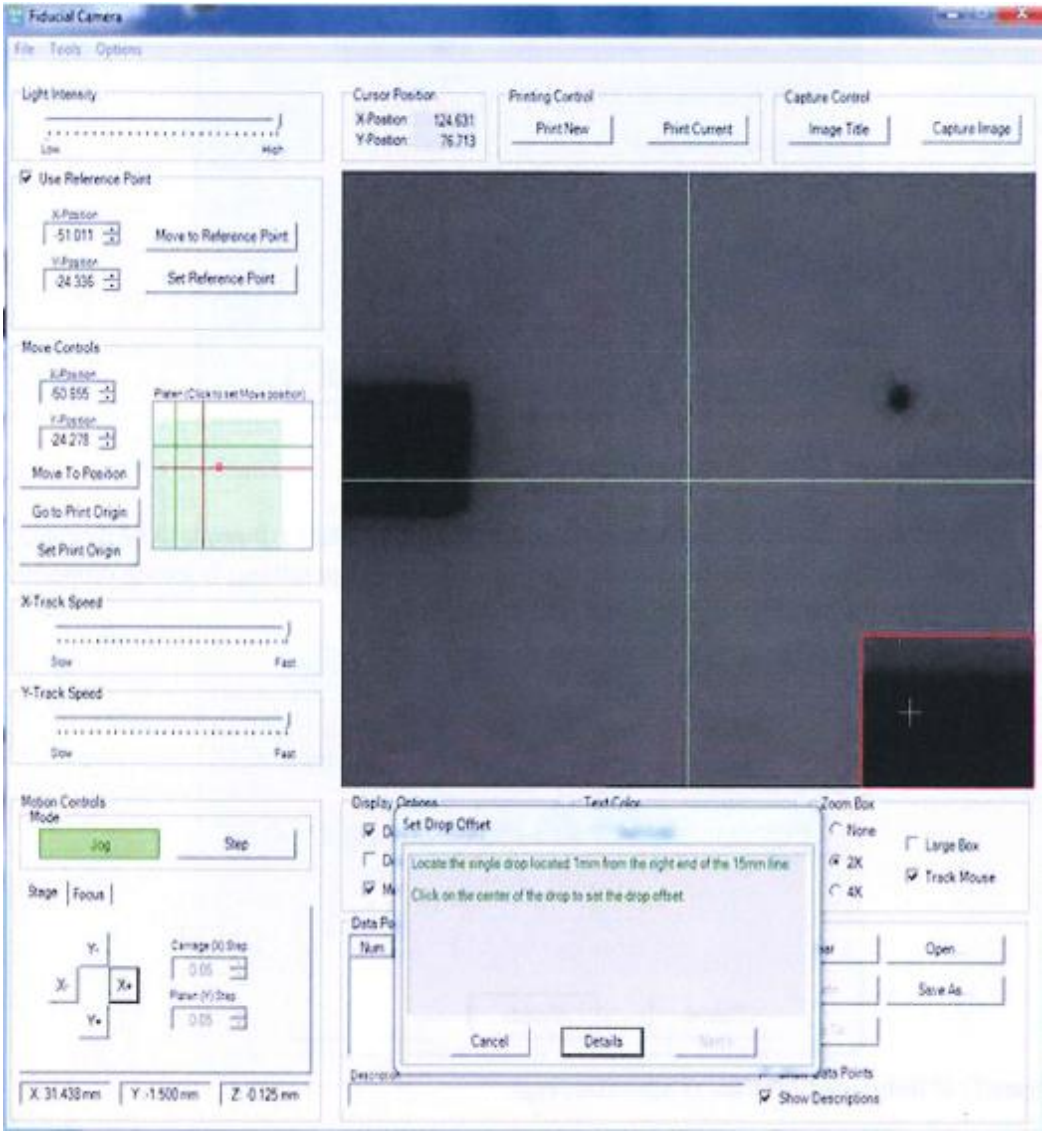

Figure 17. Image of the fiducial camera screen of a Dimatix DMP-2831 DOD Printer.

It was noted after the first print run that the solution appeared different than the first material (PVP). The next five runs were done as planned (and as above, reducing the layer on one (1) square for each layer placed). This was done to see if subsequent layers had any impact on the material dispersion on the substrate. Even though there was a visual difference, the samples were still tested for permeability.

The visual difference in solution dispersal was assessed and researched (See Section 2.2). Since polyvinylpyrridone (PVP) is used as a coating to promote the dispersal of inks on transparencies, a layer of PVP was placed on the substrate prior to a secondary print run of PVA. The PVP was placed in the same six (6) square pattern and one (1) layer was printed. Then, one (1) layer of PVA was applied, followed by one (1) layer of MMT clay, to all six squares. From here, the process was similar to layering the PVP and MMT clay; each print run, the template was reduced by one (1) square. The result was six (6) samples, each with a base layer of PVP, and with graduating bi-layers of PVA and MMT clay. These six (6) samples were then tested for permeability and characterized.

4.1.3 PEG and MMT Clay

The third round of printing on the DOD ink jet focused on the PEG solution. The same six (6) sample production method was used for PEG as for the single material PVP and MMT clay samples. It encountered the same issues as the PVA. The solution failed to disperse properly. A template of six individual squares was used, and was adjusted down one (1) square each print run until six (6) individual samples ranging from one to six bi-layers had been created. The drops beaded up and did not disperse on the Mylar substrate (as seen through the fiducial camera on the printer). It was noted after the first print run that the solution appeared different from the first material (PVP) and behaved similarly to the second (PVA). The next five runs were done as planned (and as above, reducing the number of printed squares by one (1) square for each bi-layer printed). This was done to see if subsequent layers had any impact on the material dispersion on the substrate. These samples were then tested for permeability.

Like the PVA, a second print run was performed utilizing a primary layer of PVP placed on the substrate prior to a secondary print run to promote dispersion and prevent beading of the PEG. The PVP was placed in the same six (6) square pattern and one (1) layer was printed. One (1) layer of PEG was applied, followed by one (1) layer of MMT clay to all six squares. The process was the same as layering the PVA and MMT clay. For each print run, the template was reduced by one (1) square. The result was six (6) samples, each with a base layer of PVP, and with graduating bi-layers of PEG and MMT clay. These six (6) samples were then tested for permeability and characterized.

4.1.4 Graphenol and MMT Clay

The fourth round of printing on the DOD ink jet focused on the Graphenol. The same six (6) sample production method was used for Graphenol as for the other single material samples. It encountered the same issues as the PVA and PEG. The solution failed to disperse properly. Initially, a template of six squares was adjusted in the same manner as the previous films until six (6) individual samples consisting of one to six bi-layers had been created. However, the drops beaded up and did not disperse on the Mylar substrate (as seen through the fiducial camera on the printer). It was noted after the first print run that the solution appeared different than the first material (PVP) and more like the PVA and PEG, but the next five runs were done as planned (and as above, reducing the layer on one (1) square for each layer placed). This was done to see if subsequent layers had any impact on the material dispersion on the substrate. These samples were then tested for permeability.

Like the PVA and PEG, a second print run was performed utilizing a primary layer of PVP placed on the substrate prior to a secondary print run to promote dispersion

and prevent beading of the Graphenol. The PVP was placed in the same six (6) square pattern and one (1) layer was printed. Then, one (1) layer of PEG was applied, followed by one (1) layer of MMT clay, to all six squares. From here, the process was the same as layering the PVA and MMT clay; each print run, the template was reduced by one (1) square. The result was six (6) samples, each with a base layer of PVP, and with graduating bi-layers of Graphenol and MMT clay. These six (6) samples were then tested for permeability and characterized.

4.2 Film Characterization

Total, there were 54 samples for analysis. After all films had been printed, it was necessary to examine them both visually and test their permeability. The following methods were used to analyze the various films: optical microscope, scanning electron microscope (SEM), atomic force microscope (AFM), surface profilometer, and permeability testing. The single material PVP and MMT clay films were analyzed for permeability and using the optical microscope. Only those samples, which contained layered solutions and clay, were analyzed using the SEM, AFM, and profilometer.

4.2.1 Optical Microscope

The fiducial camera on the printer, while useful for visualizations while printing was limited in ability to 5x scope. Therefore, each sample was viewed using an Olympus BX60 Polarizing optical microscope (See Appendix V). Each sample was viewed using polarized light at 5x, 10x, 20x, 50x. The polarized light helped to distinguish the difference between the polymer and clay layers. The different levels of magnification allowed for the identification of drop spacing. It also provided a visual for how well the solution dispersed over the substrate and if any voids had developed. There was an

attempt made to view some of the films at higher magnification, but it was so close that spacing could not adequately be determined and voids could not be seen.

4.2.2 Profilometer

Initially to gauge film thickness, samples were mounted on a Tencor Alpha Step 500 surface profilometer, (See Appendix V for equipment details). A profilometer has a sensitive stylus that can indicate surface profile. First, a sheet of Mylar alone was measured to gauge substrate thickness. Then, the different samples at the varying numbers of layers were measured. This was done to see if layer growth (thickness) was linear or non-linear.

4.2.3 Scanning Electron Microscope (SEM)

The next round of visual characterization involved viewing samples with the FEI Helios Nano Lab 400 scanning electron microscope (SEM), (See Appendix V). It was thought the SEM would assist in determining film thickness. Because the SEM causes the polymer to charge up, the image quality was degraded. To combat this, a 2μm layer of gold was placed on the tops of the films so that SEM imagery could be taken. This allowed for the films to be imaged.

Ion milling was performed utilizing the SEM. Based on a user input pattern, the SEM bombards the sample with ions, milling out a place where elemental analysis can be performed at user-programmed points. This shows the elemental composition at each measured point. This allowed for the identification of where the transitions from gold to film and film to substrate occur. This information can be used to determine the thickness of the different layers.

4.2.4 Atomic Force Microscope (AFM)

A Burker Nano Dimension 3100 atomic force microscope (AFM) was used for surface analysis, (See Appendix V). Analysis by AFM indicates how smooth or rough the film surface is. For those samples, which required a gold coating, the AFM measurements were done prior to placement of the gold.

4.2.5 Permeability Study

Permeability measurements were taken for each sample containing a clay layer. A Mocon 2/60 was used to perform the permeability analysis, and is capable of analyzing six (6) samples at a time, (See Appendix V). This allowed for all six samples of each film (PVP/MMT clay; PVA/MMT clay; PEG/MMT clay; and Graphenol/MMT clay) to be placed in the machine at the same time. The samples are placed between two chambers, one containing carrier gas and the other containing oxygen. The machine analyzes each sample separately by trying to force oxygen through it into the carrier gas in the other chamber. The carrier gas then moves any oxygen, which makes it through to an oxygen detector so that it can analyze any trace amounts that has permeated the sample.

4.2.6 Wide Angle X-ray Scattering (WAXS)

X-ray analysis was conducting using a Bruker D8 Focus Powder X-ray Diffractometer with a Sol-X Solid State Detector. A half inch square section of each film was cut and glued to the sample holder with rubber cement. The samples were mounted with the printed films facing up. The selected scanning angle was from one to thirty-five degrees. The results and explanation of the data can be seen in section 5.5.

CHAPTER 5

Results and Discussion

5.1 PVP and MMT Clay

The first round of films were the singular Polyvinylpyrrolidone **(**PVP) and Montmorillonite (MMT) nanoclay. This was done to see if it was even possible to print using these materials. With a few adjustments to the ink solution concentrations and printer settings, films were generated. The results of the permeability tests for the singular PVP, singular MMT nanoclay is given in Table 3.

Table 3. Oxygen Transition Rates for DOD printed films made of PVP & MMT nanoclay.

MATERIAL	$cm^3/m^2/24hr/mil$	% REDUCTION
Mylar no coating	5.3	
1 LAYER PVP ONLY	5.1	4%
2 LAYER PVP ONLY	5.1	4%
3 LAYER PVP ONLY	5.0	6%
4 LAYER PVP ONLY	4.9	8%
5 LAYER PVP ONLY	4.9	8%
6 LAYER PVP ONLY	4.8	9%
1 LAYER MMT ONLY	5.1	4%
2 LAYER MMT ONLY	5.1	4%
3 LAYER MMT ONLY	5.1	4%
4 LAYER MMT ONLY	5.1	4%
5 LAYER MMT ONLY	5.0	6%
6 LAYER MMT ONLY	5.0	6%

The permeability of the Mylar film by itself was 5.3 $cm^3/m^2/24hr/mil$. As subsequent layers of PVP and MMT nanoclay is added, there is little change in the permeability as can be seen in the percent of OTR reduction. Once the materials are layered, there is a substantial difference in the oxygen transmission rate and the percent of reduction in the OTR. The results for the layered PVP and MMT clay are given in Table 4.

Table 4. Oxygen Transition Rates for DOD printed films made of PVP & MMT nanoclay.

PVP & MMT LAYERED	$cm^3/m^2/24hr/mil$	% REDUCTION
Mylar no coating	5.3	
1 BI-LAYER	1.6	70%
2 BI-LAYER	1.0	81%
3 BI-LAYER	0.6	89%
4 BI-LAYER	0.2	96%
5 BI-LAYER	0.0	100%
6 BI-LAYER	0.0	100%

The results at 5 bi-layers and 6 bi-layers PVP/MMT clay indicate a 0.0 oxygen transmission rate. The implication is that this combination of solutions layered at the correct rate is an acceptable oxygen barrier in a given application. With more layers, there is more polymer/clay bonding occurring, creating a more effective film. Figure 18 shows the difference in films at 1 and 6 bi-layers each of PVP and MMT nanoclay as observed with the printers fiducial camera.

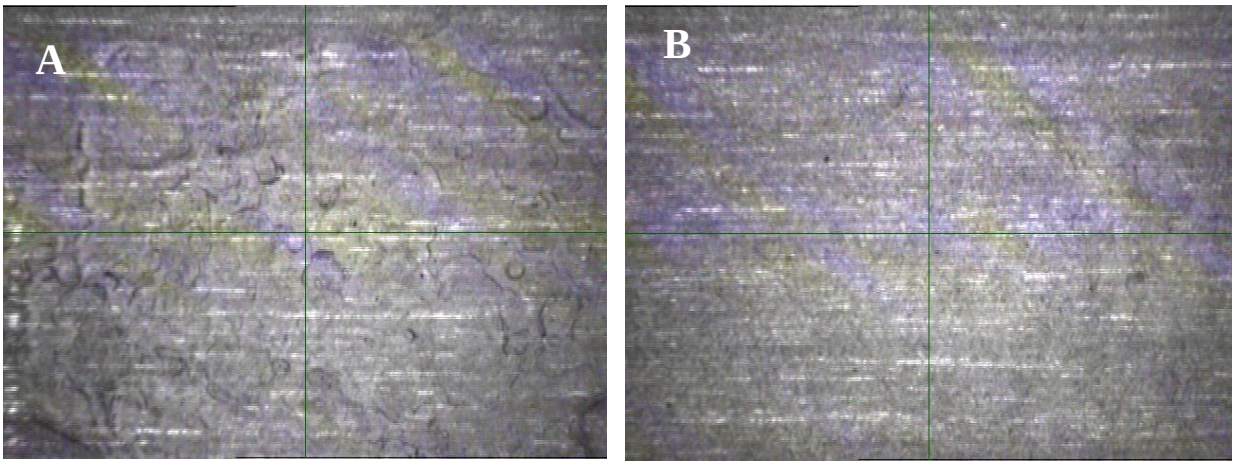

Figure 18. Images of films made from solutions of PVP & MMT. 1 bi-layer (A) and 6 bi-layers (B).

The film formation in the 1 bi-layer image on the left is distinctly textured compared to the 6 bi-layer image on the right. This is due to the drops of the single layers coalescing into each other. As they coalesce, more solution is forced to the outer edge of the drops, creating the "rings" visible in the image on the left. As more layers are added, the wave propagation of the drops is restricted by the previous layers. This results in successive layers "filling in the rough spots," creating the more uniform film on the right. This indicates that the clay helps with uniformity in film formation, and as more layers are added, the film thickness becomes more even and uniformed.

The goal is for bonding to take place and for the drops to disperse evenly across the surface without coalescing into un-even areas. One of the parameters, which emerged as important was the temperature of the solution at application. The hotter material dries more quickly. This means less time for the cationic and hydrogen bonding to occur between the polymer and the clay. The heat can cause the material to become crystalline in nature, resulting in brittleness and cracking. Figure 19 shows the difference in 1 bi-

layer applied with no heat (left) compared to 1 bi-layer applied with heat, specifically at 45º C (right).

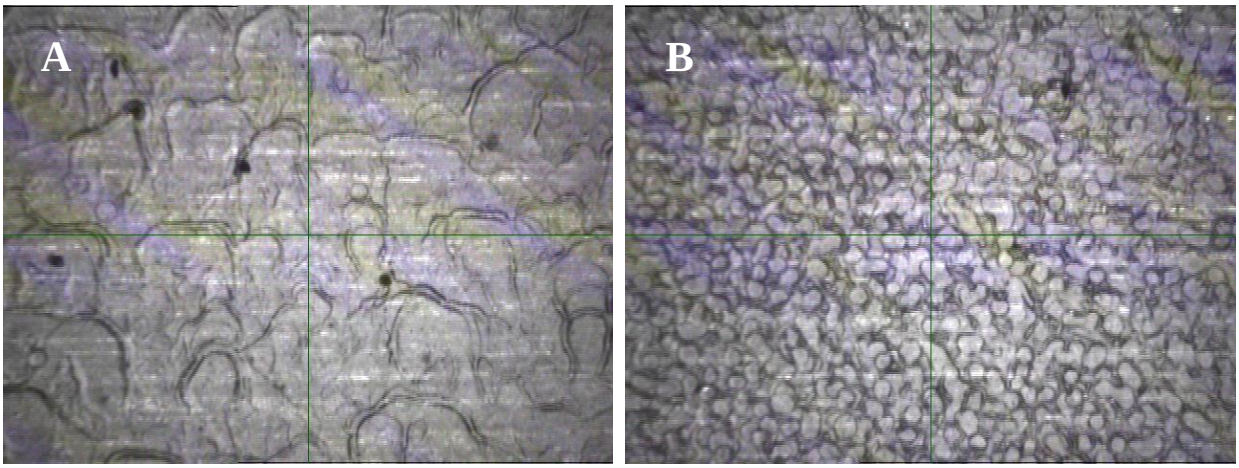

Figure 19. Images showing the effects of no platen heat (A) vs. platen heat (B) on films made from solutions of PVP & MMT.

The image of the film on the left, while exhibiting strong coalescence, indicates that bonding is occurring. In the image on the right, the drops applied with heat dried in place before bonding could occur, and so individual drops are still visible. The result is voids between each individual droplet where there is no film generation. The voids make it permeable by oxygen and moisture. It is desirable to apply the material at room temperature and allowing the bonding to take place.

Drop spacing was also investigated to determine the optimal spacing of the droplets. Figure 20 shows that changing the drop spacing of a single bi-layer film from 12μm to 25μm greatly affected the film formation. The images were taken with platen heat applied at 39º C. Additional testing was done with no heat applied. The results were similar but the droplets were more dispersed as seen in Figure 21.

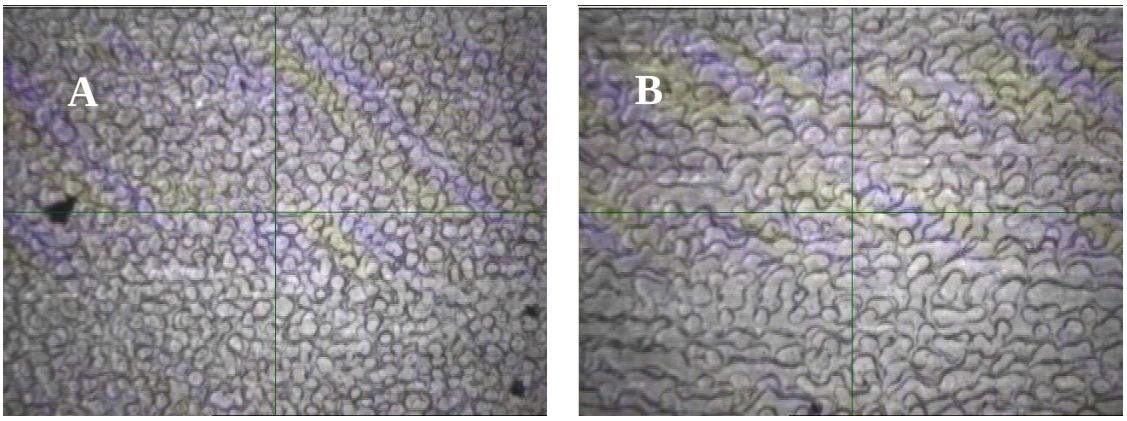

Figure 20. Images showing the effects of drop spacing. (A) drop spacing is at 12µm and 39º C, (B) drop spacing is at 25µm and 39º C.

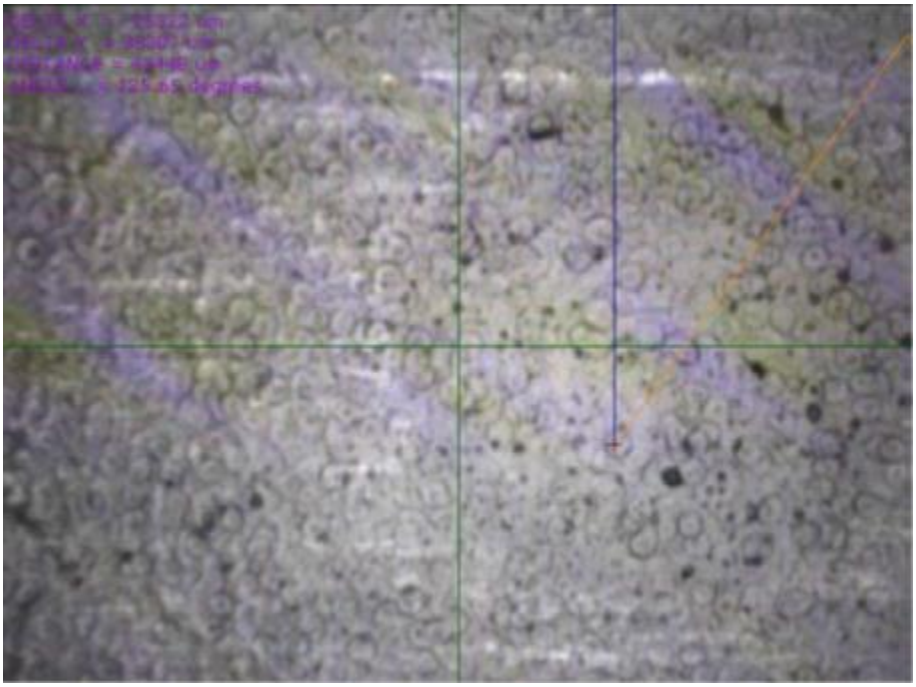

Figure 21. Image showing the effects of drop spacing without heat, the drop spacing is at 12µm and room temperature.

Varying the number jets/nozzles used at one time produced results similar to the drop spacing changes. Using more jets/nozzles at the same drop spacing caused the

droplets to coalesce into larger droplets leaving large voids in the film. Using fewer jets/nozzles at the same drop spacing reduced the coalescence. When you drop below three jets/nozzles, the droplets begin to become separated and create large void areas between the droplets. Figure 22 illustrates the effects of varying the number of used during printing.

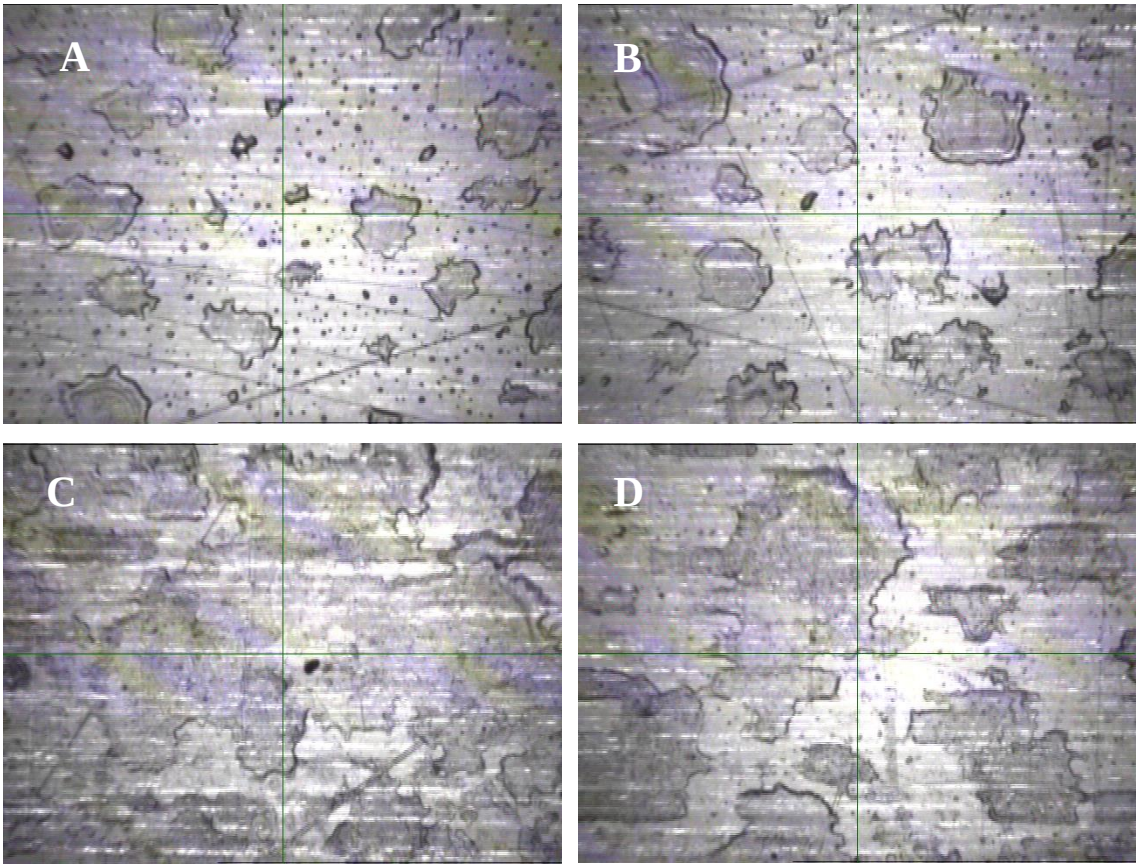

Figure 22. Images of films created from solutions of PVP & MMT with varying numbers of jets/nozzles. (A) 1 bi-layer printed with 1 jet/nozzle at 30µm, (B) 2 jets/nozzles at 30µm, (C) 3 jets/nozzles at 30µm, and (D) 5 jets/nozzles at 30µm.

The film uniformity was assessed with a scanning electron microscope (SEM). It is possible to see the dispersion of clay particles in the polymer material in Figure 23. According to this analysis, the MMT clay had a good dispersion rate in the PVP.

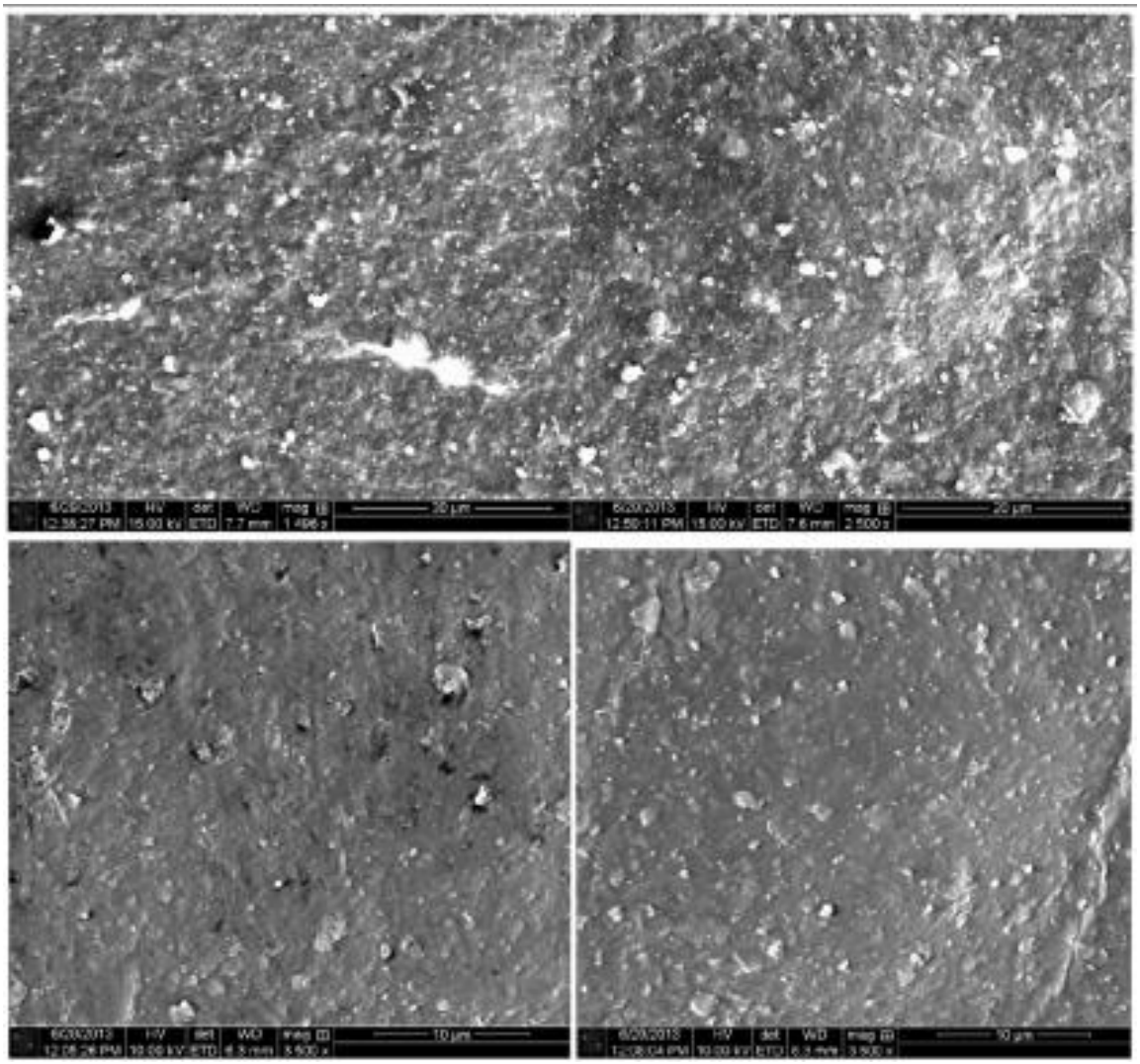

Figure 23. SEM images showing dispersed clay in films created from a solution of PVP & MMT nanoclays.

The AFM image in Figure 24 indicates good uniformity in the films surface as indicated by a Z range of 59.919 nanometers as compared to the PVA image in Figure 36, which had a Z range of 652.07 nanometers due to droplet coalescence and resultant voids between the combined droplets.

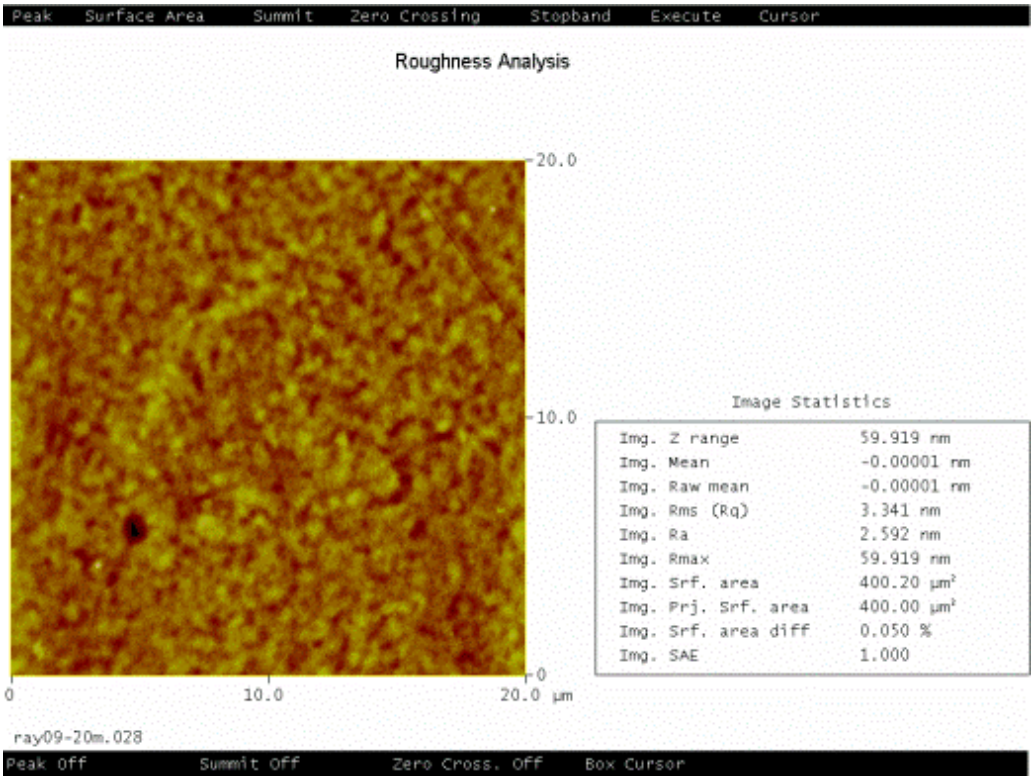

Figure 24. AFM image of a film created from a solution of PVP & MMT nanoclay. Results indicate a uniformed film.

An elemental analysis was done to distinguish between the films and the Mylar substrate. Prior to the elemental analysis, ion milling was performed to expose the individual layers and materials as shown in Figure 25. The elemental analysis tool, EDAX, was used to do point analysis to determine the transition point from Mylar substrate to film. For the purposes of this research, the elements Aluminum (AlK) and Silicate (SiK) were sought. They indicate the presence of clay and not the substrate. It is possible to determine the thickness of the film by measuring from the top down to the transition point to the substrate. This gives the overall thickness of the film, which is shown in Figure 30.

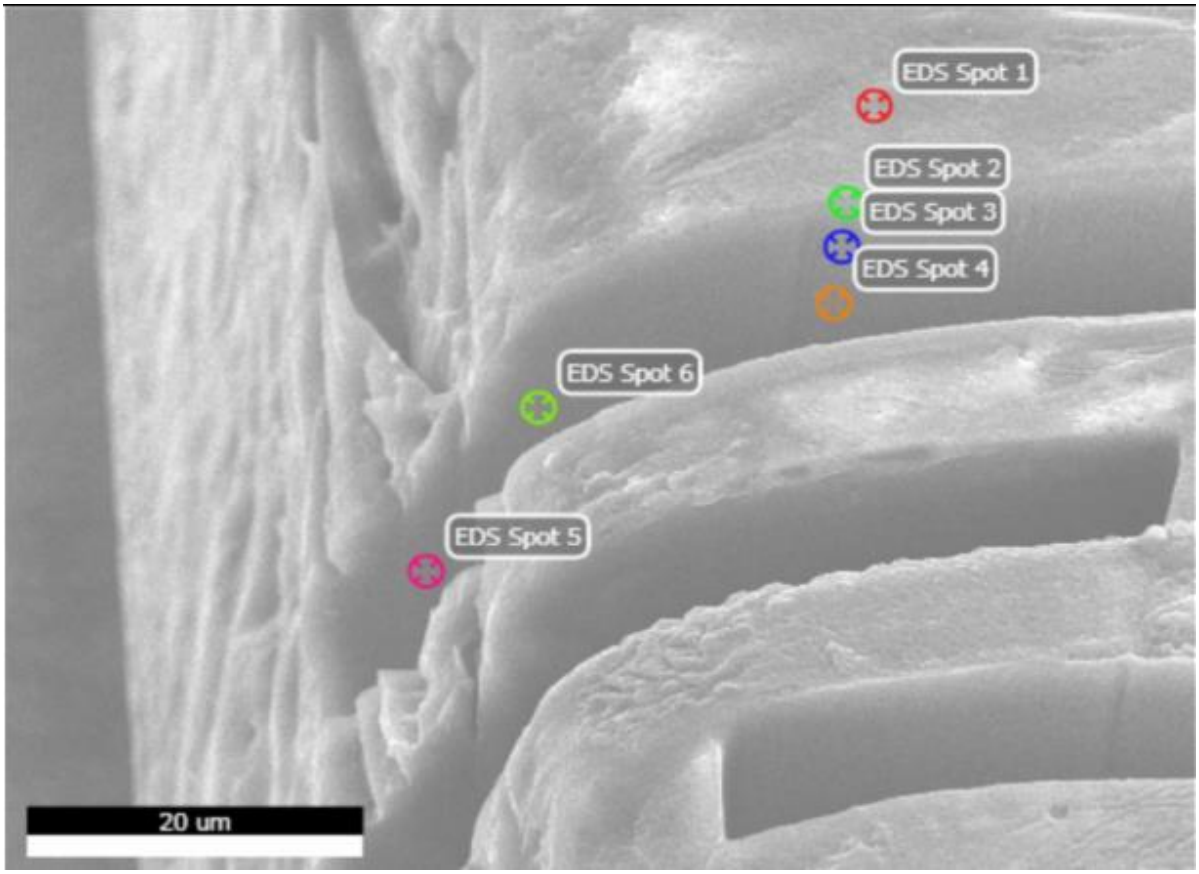

Figure 25. Image of EDAX point analysis performed on a film made from a solution of PVP & MMT.

The results of the EDAX are given in Figures 26 - 29. EDS Spot 1 is taken from the surface where the film is none to exist, EDS Spot 2 is on the side of the milled slot in the film area, and spots 3 and 4 are located on the side of the milled slot below the film, as there is no presence of Al or Si. There is a slight change in color on the side of the milled slot where there is a transition from the film to substrate; this can be observed better in Figure 30.

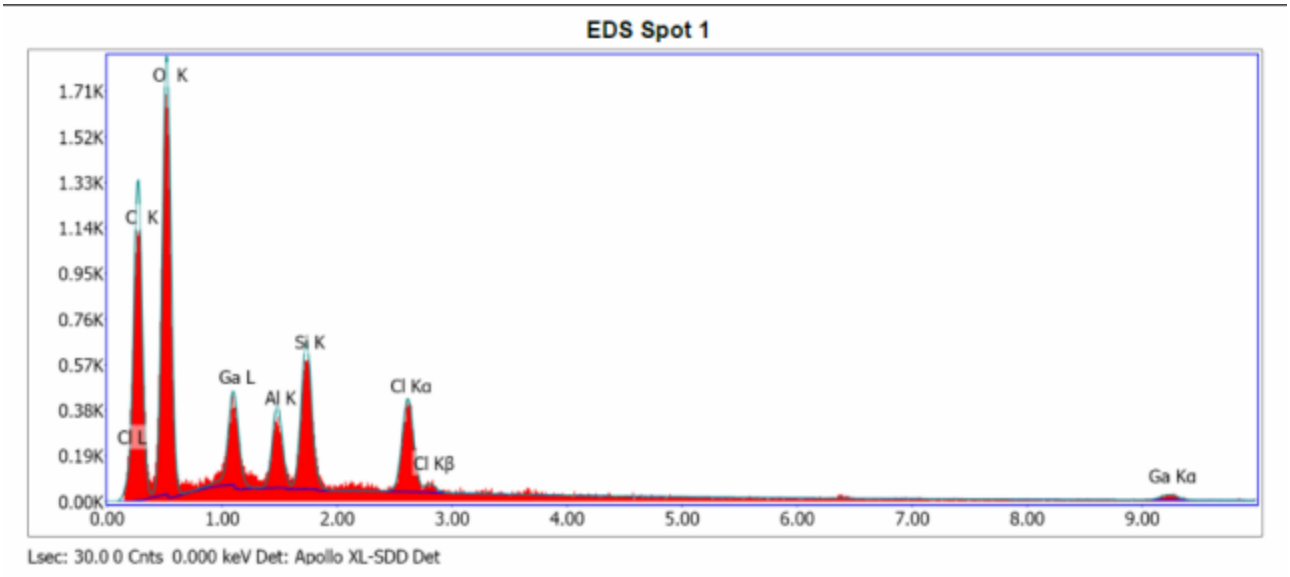

Figure 26. Image of EDAX point (1) analysis performed on a film made of PVP & MMT printed on a Mylar substrate. The presence of Al and Si indicate the presence of the PVP&MMT film.

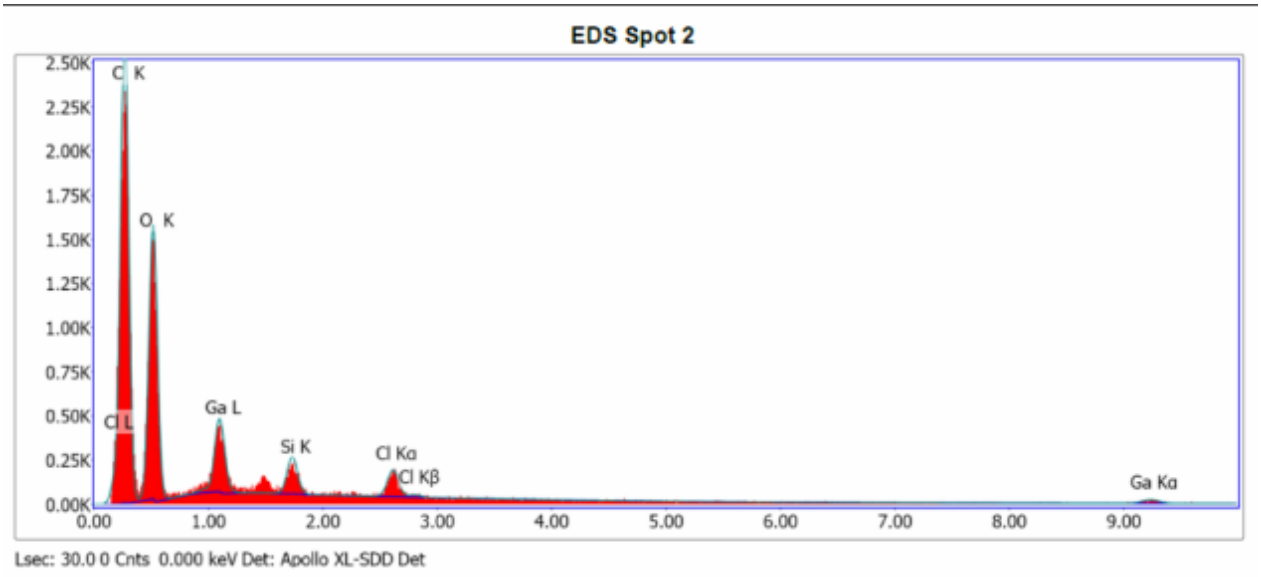

Figure 27. Image of EDAX point (2) analysis performed on a film made of PVP & MMT printed on a Mylar substrate. The presence of Al and Si indicates the presence of the PVP&MMT film.

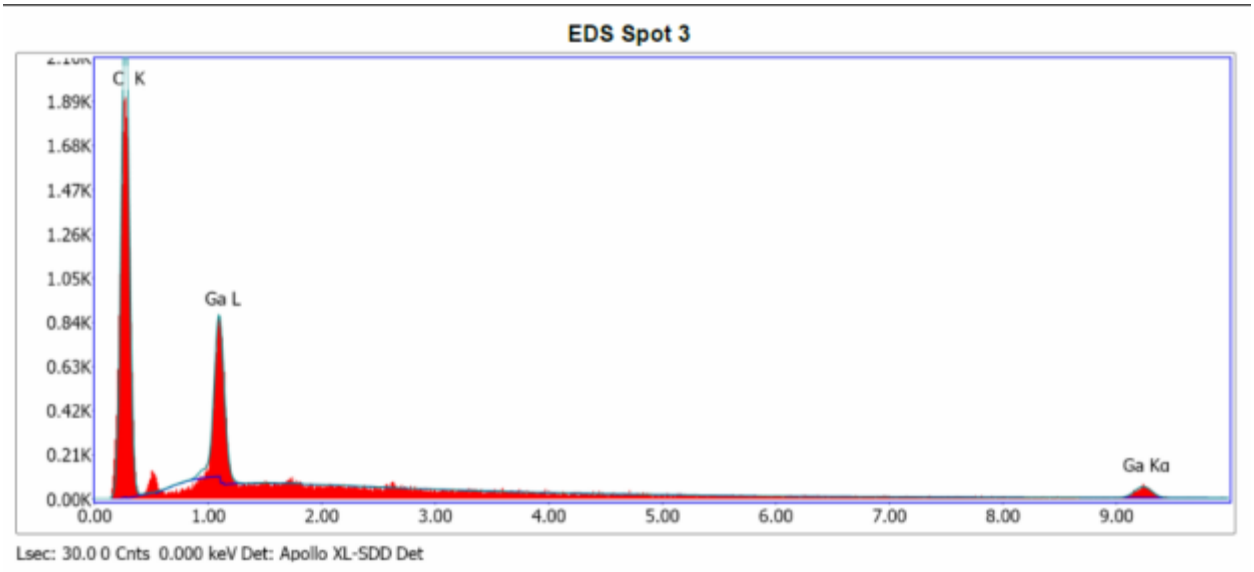

Figure 28. Image of EDAX point (3) analysis performed on a film made of PVP & MMT printed on a Mylar substrate. The lack of Al and Si indicates it is the Mylar substrate.

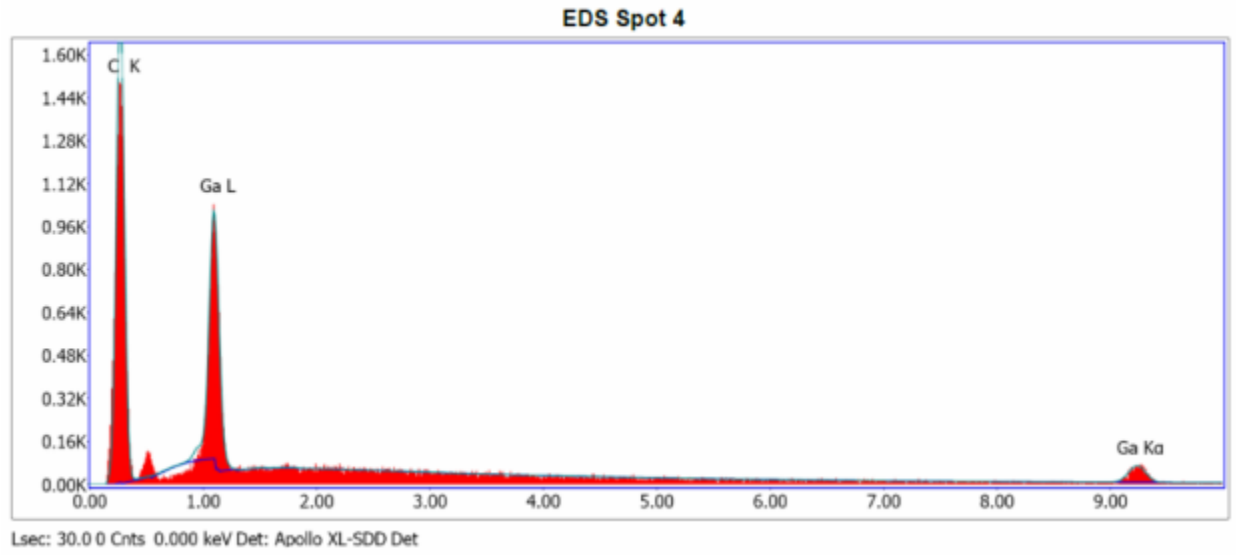

Figure 29. Image of EDAX point (4) analysis performed on a film made of PVP & MMT printed on a Mylar substrate. The lack of Al and Si indicates it is the Mylar substrate.

Due to cost and equipment time constraints, it was not realistic to measure the thickness of all the fifty four film samples with the SEM. Therefore, other techniques such as optical microscope measurements and sample weights from a percision balance

were used. Film thickness was verified and determined by comparing the PVP/MMT clay film thicknesses as measured on the SEM to the thicknesses visible in the optical microscope images and calculations using film weights. Figure 30 is the SEM image of the 1 bi-layer PVP/MMT clay film. It indicates that the film is 3.79µm thick. Figure 31 is the optical microscope image of the same film, indicating a thickness between 3.61 µm and 3.63 µm, a difference of about 16/100 of a µm. Figures 32 & 33 show the film thickness for 3 & 6 bi-layers.

A preceision balance was used to measure the weight of the uncoated Mylar substrate and each film sample. Using the density of the ink solution, known sample size, and the measured weights, it was possible to calculate the fim thickness, which was 3.92 µm for the single bi-layer. The optical microscope and percision balance provided comperable results quickly at a fraction of the time and cost. They were used to measure the thickness of the remaining films (PVA/MMT clay, PEG/MMT clay and Graphenol/MMT clay). Table 5 indicates the calculated film thickness for the PVP & MMT nanoclay samples.

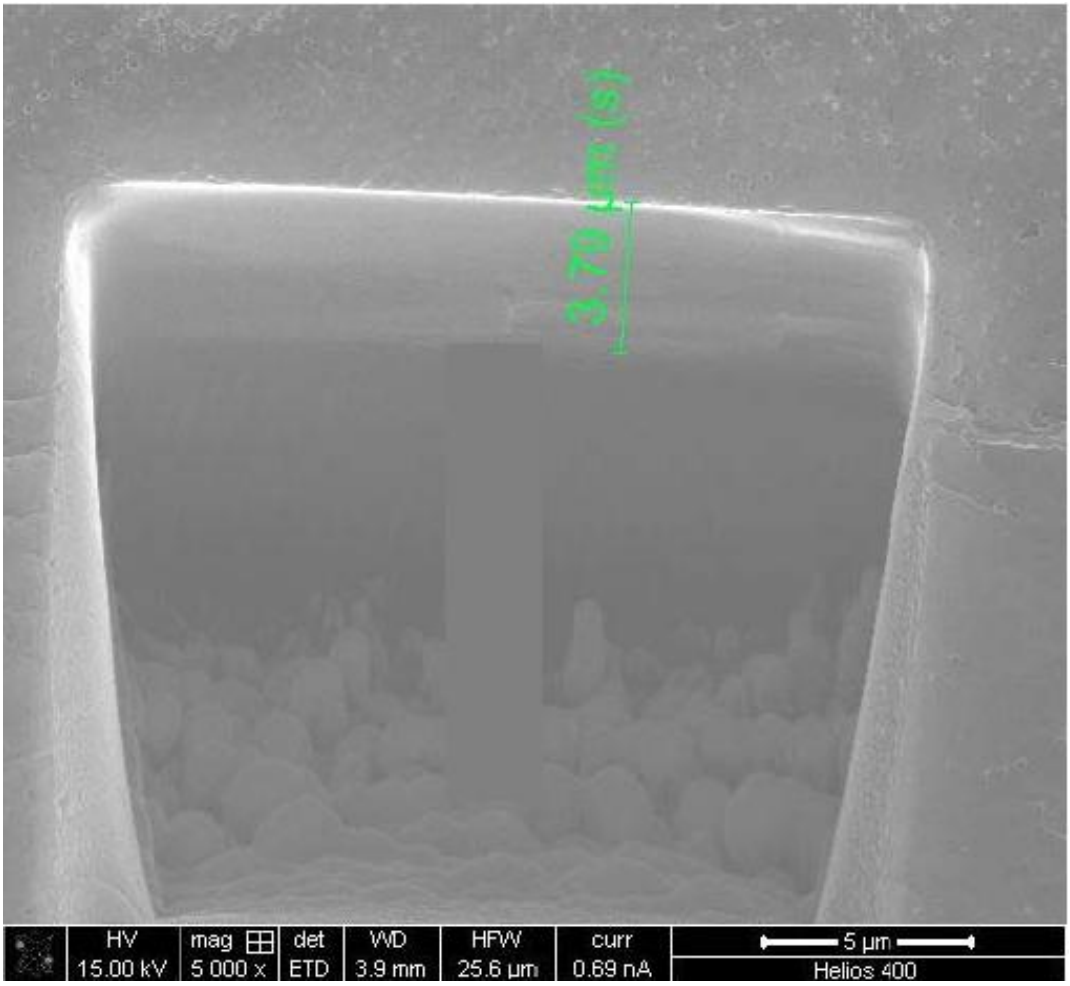

Figure 30. SEM image indicating the thickness of a single Bilayer of a film made of PVP & MMT.

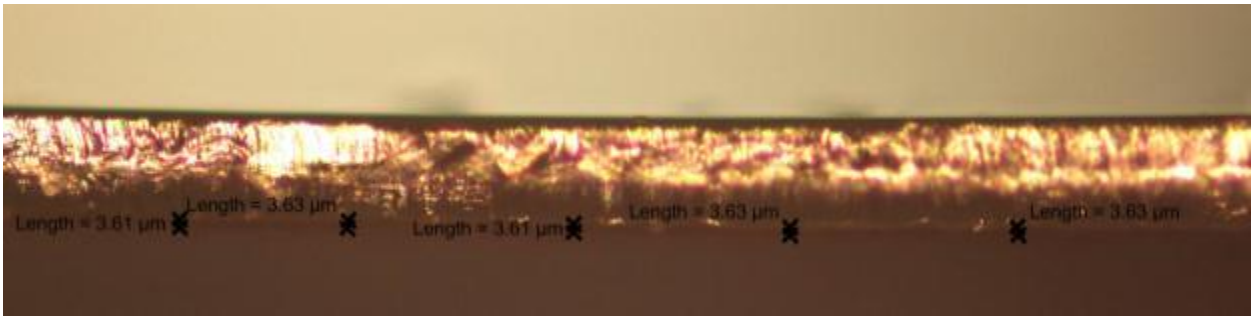

Figure 31. Optical microscope image indicating the film thickness of a film made from 1 Bilayer of PVP & MMT, film thickness average is 3.6µm.

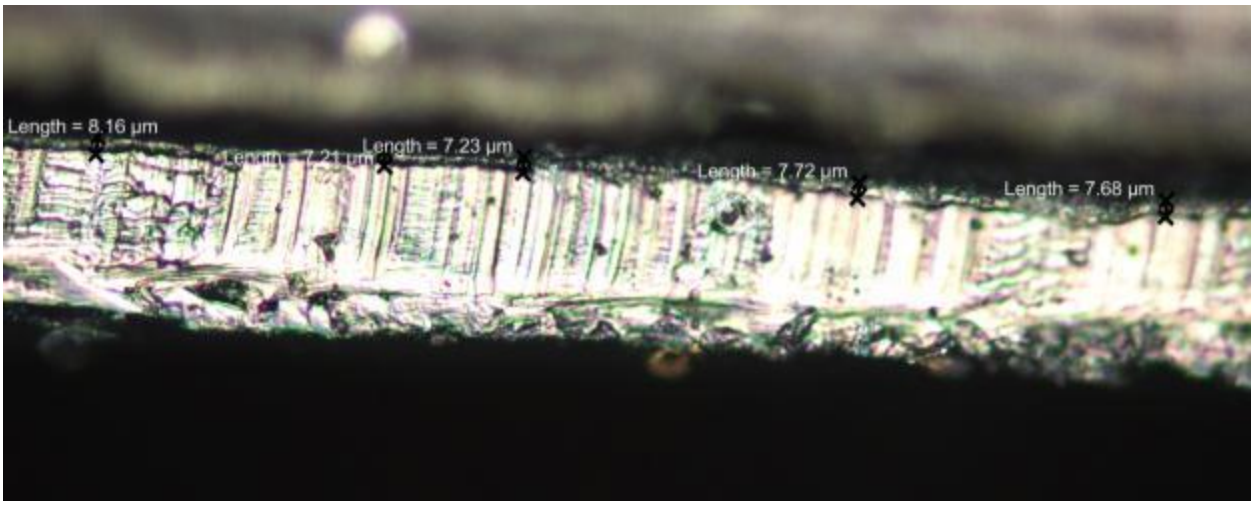

Figure 32. Optical microscope image indicating the film thickness of a film made from 3 Bilayers of PVP & MMT, film thickness average is 7.5µm.

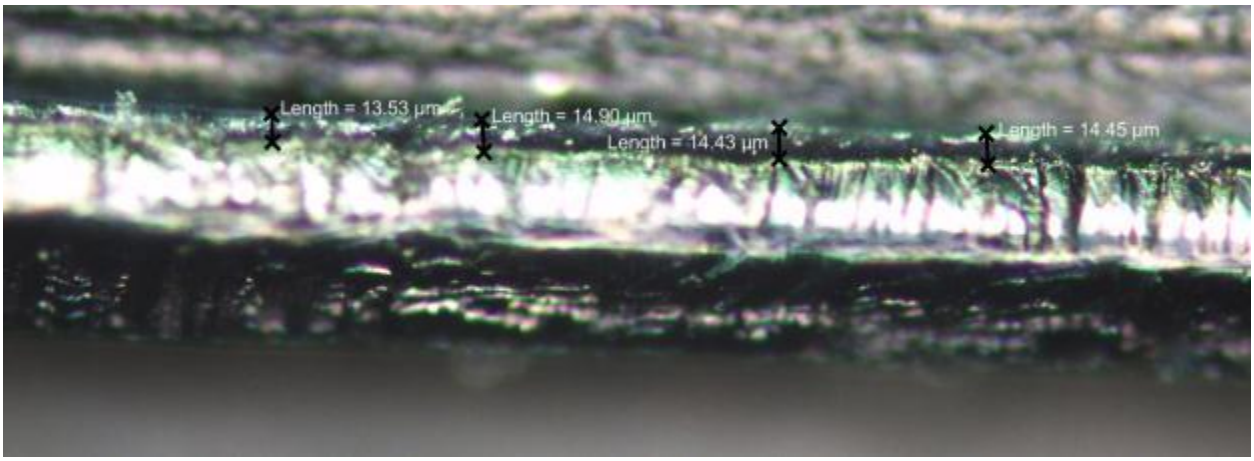

Figure 33. Optical microscope image indicating the film thickness of a film made from 6 Bilayers of PVP & MMT, film thickness average is 14.5µm.

Table 5. Calculated thickness of films created from a solution of PVP & MMT.

PVP & MMT			
Ink Solution Density g/cm^3	Bi-Layers	Film Weight g	Film Thickness µm
1.775	1	0.00008	3.92
1.775	2	0.00012	5.39
1.775	3	0.00018	7.84
1.775	4	0.00025	10.78
1.775	5	0.00031	13.23
1.775	6	0.00037	15.19

5.2. PVA and MMT Clay

Due to the viscosity of the material, the PVA solution was mixed at 0.1% weight by volume. The printed PVA solution appeared visually different from the PVP printed solution. It was immediately apparent that the drop dispersion was flawed. Using the printer fiducial camera, it was possible to see that the solution had beaded up rather than dispersing evenly over the substrate. Permeability results on the initial films containing only PVA (without a PVP base) indicated high permeability. This is believed to be due to the droplet contact angles and surface energy of the solution and the substrate. Figures 34 and 35, taken with the fiducial camera on the printer, show the difference in material applied with and without a PVP base coat on the Mylar substrate at 1 and 6 bi-layers of PVA/MMT clay.

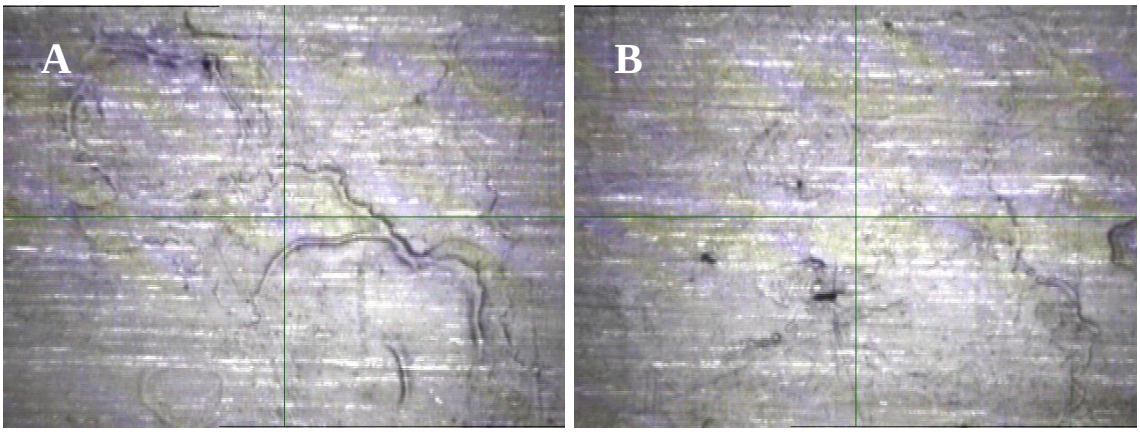

Figure 34. Image (A) 1 bi-layer and (B) 6 bi-layers of films created from a solution of PVA & MMT with no PVP basecoat.

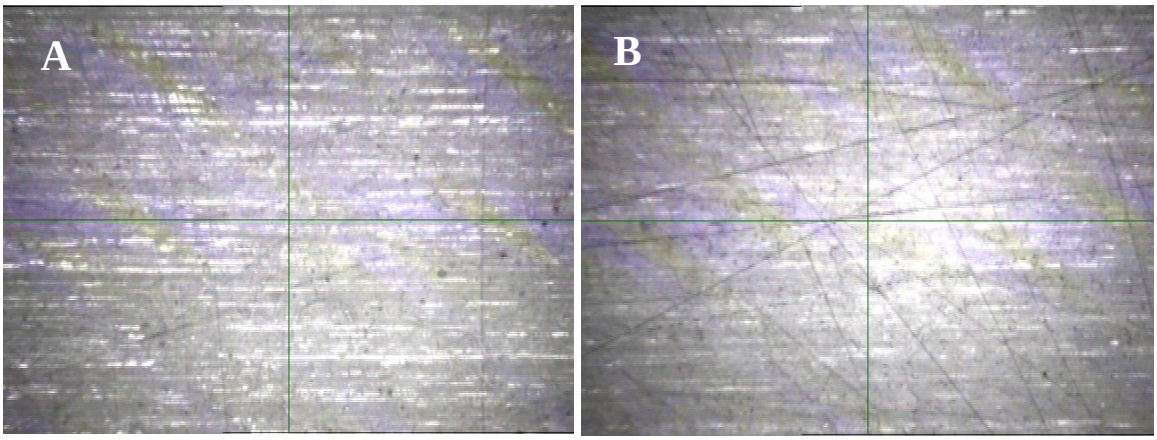

Figure 35. Image (A) 1 bi-layer and (B) 6 bi-layers of films created from a solution of PVA & MMT with a PVP basecoat.

It is visually apparent that the PVP base coat reduces coalescence of PVA/MMT clay solutions, resulting in a uniform film. Figure 36 is an AFM image of the PVA/MMT clay film at 1 bi-layer, without the PVP base coat. The films Z range is 652.07 nm, which is very high compared to the 59.919 nm of the PVP/MMT clay film.

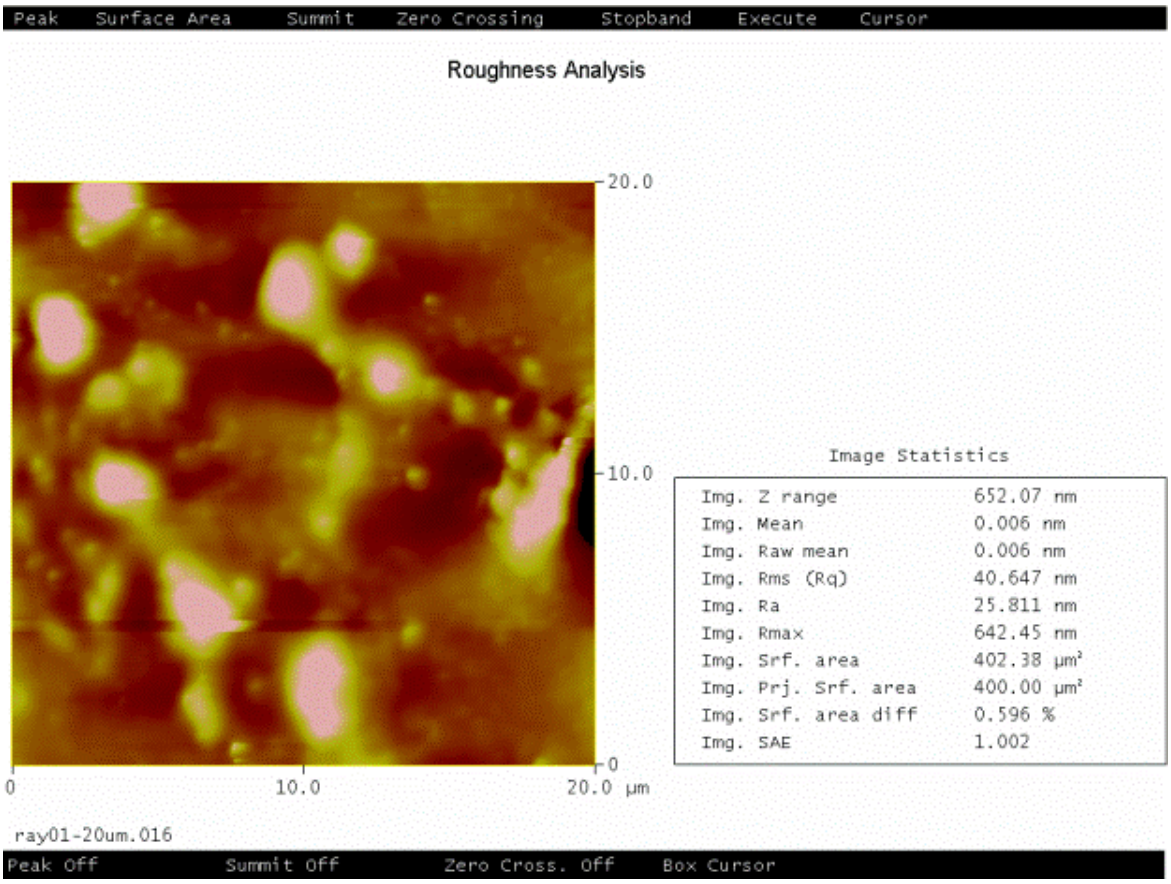

Figure 36. AFM image of a film created from a solution PVA & MMT. 1 bi-layer with no PVP base coat. Results indicated how non-uniformed the film is.

Figure 37, a 3 bi-layer PVA/MMT film illustrates the effects heat has on the drop dispersion and film formation. As with the PVP/MMT film, the addition of heat causes the droplets to dry rapidly and prevents them from dispersing evenly and or coalescing. The film in figure A, which was created without heat one can see how the droplets flowed and dispersed across the substrate. The film in figure B, which was created with heat applied to the platen, prevented the droplets from dispersing due to rapid evaporation.

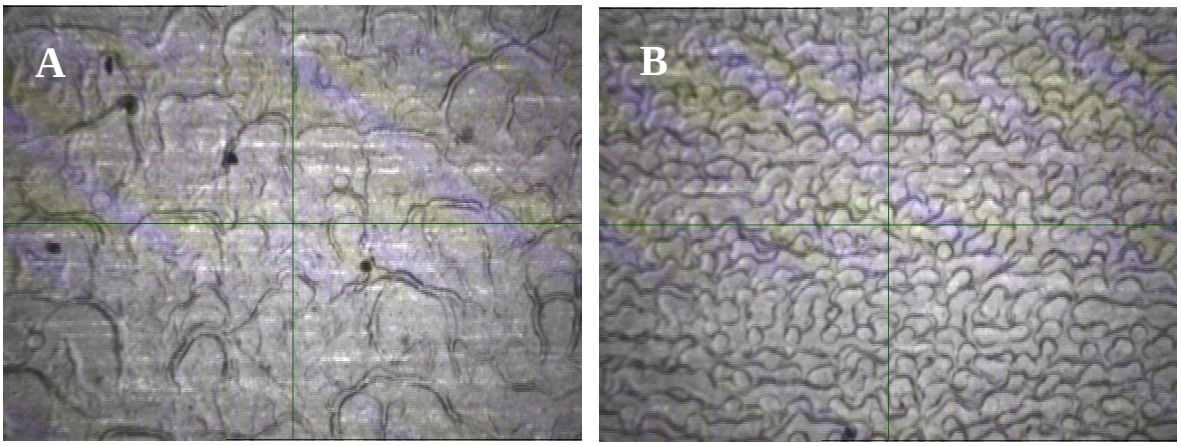

Figure 37. Images of a film created from a solution of PVA & MMT indicating the effects of heat on the film formation. (A) 3 bi-layers of PVA/MMT no platen heat. (B) 3 bi-layers at 45 C.

Again, ion milling and elemental analysis was performed to determine exactly where the film began and ended in order to measure the films thickness. Figure 38 shows the EDS spots in the milled film where the elemental data analysis was conducted. The results are given below in Figures 39-41. EDS spots 1 and 2 show the presence of Al and Si, but spot 3 does not, indicating it is the substrate. Table 6 provides the film thickness for each of the bi-layers.

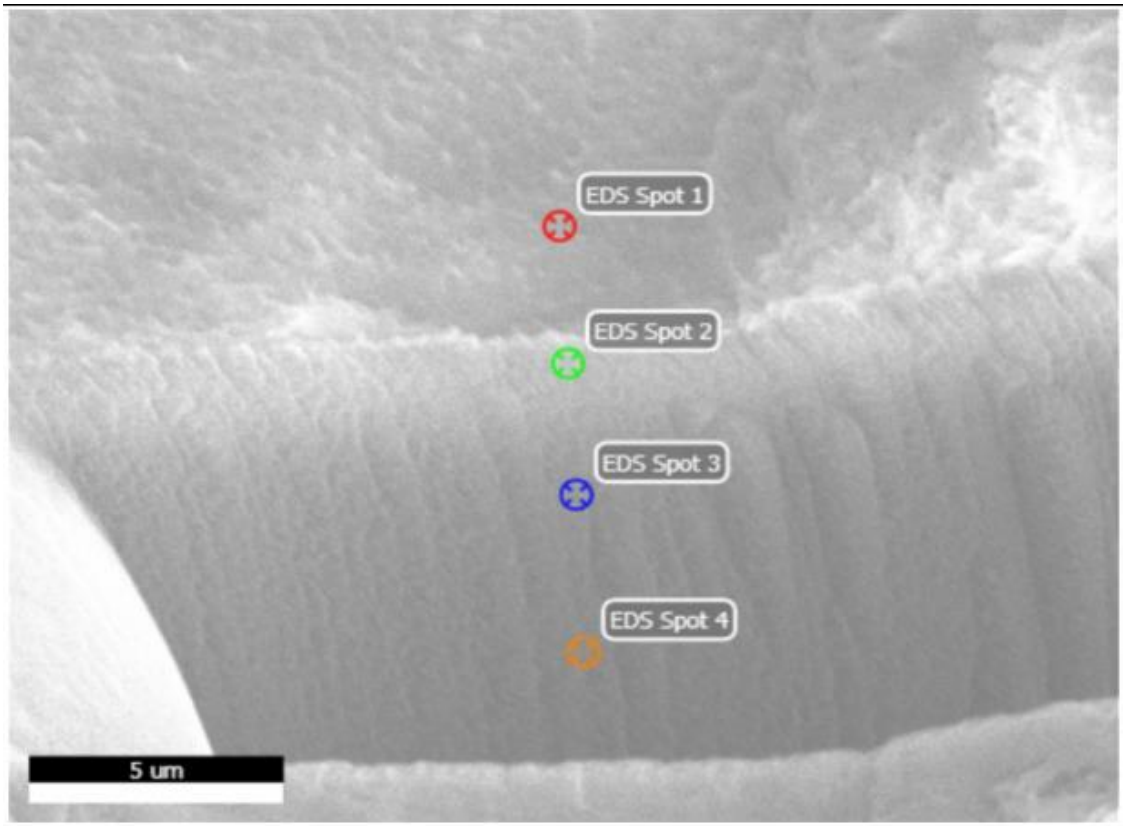

Figure 38. Image of EDAX point analysis performed on a film made of PVA & MMT printed on a Mylar substrate.

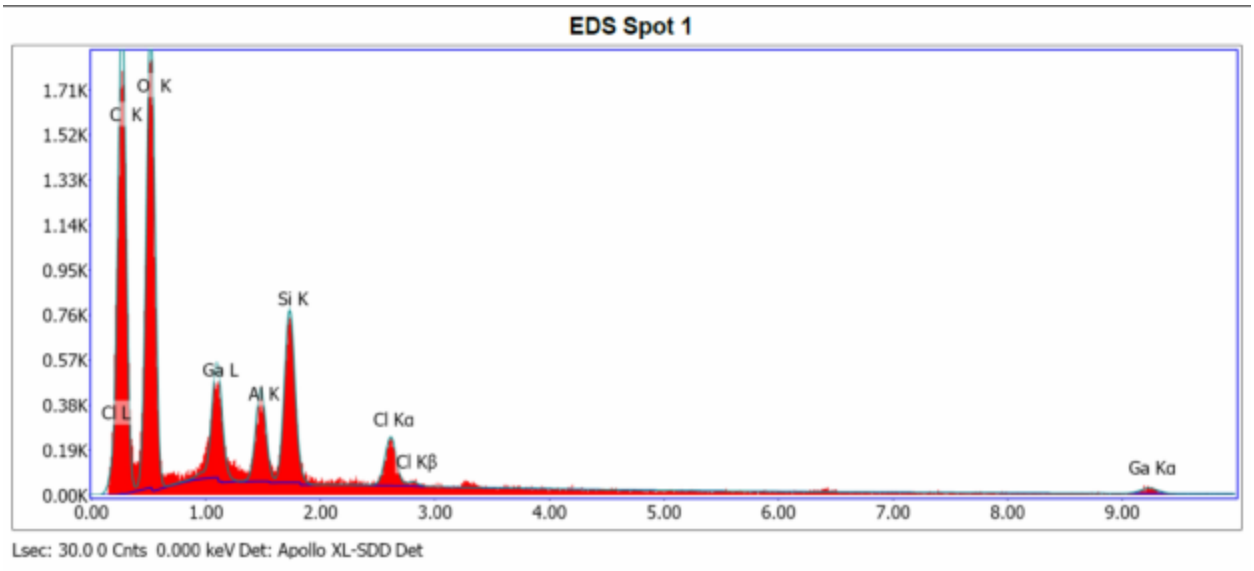

Figure 39. Image of EDAX point (1) analysis of the PVA/MMT film on a Mylar substrate. The presence of Al and Si indicates the presence of the PVA&MMT film.

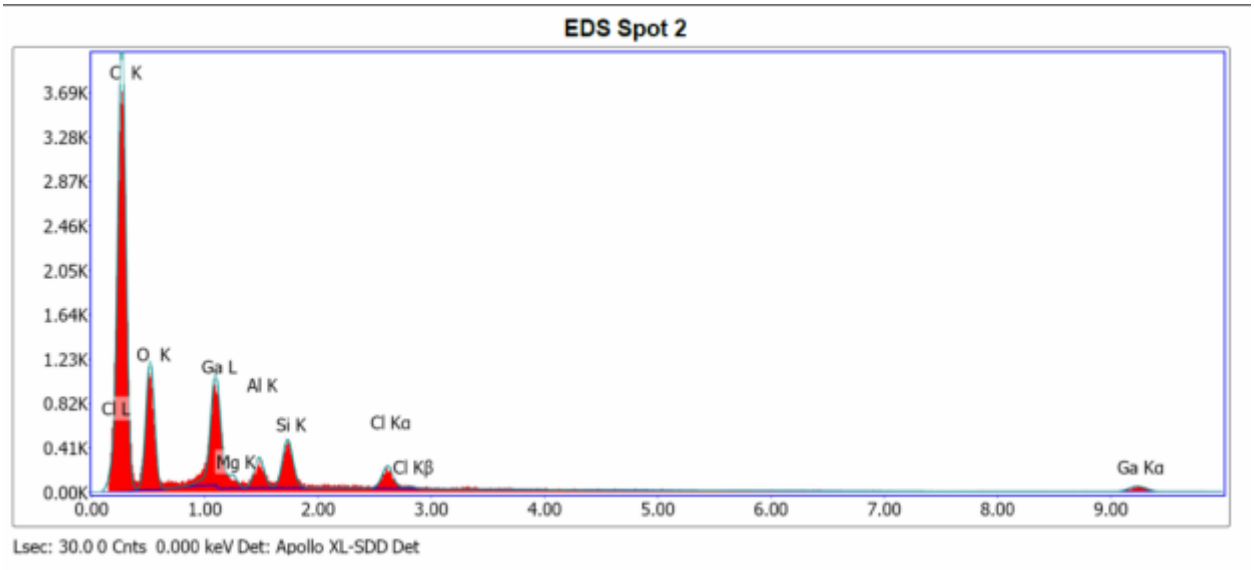

Figure 40. Image of EDAX point (2) analysis of the PVA/MMT film on a Mylar substrate. The presence of Al and Si indicates the presence of the PVA&MMT film.

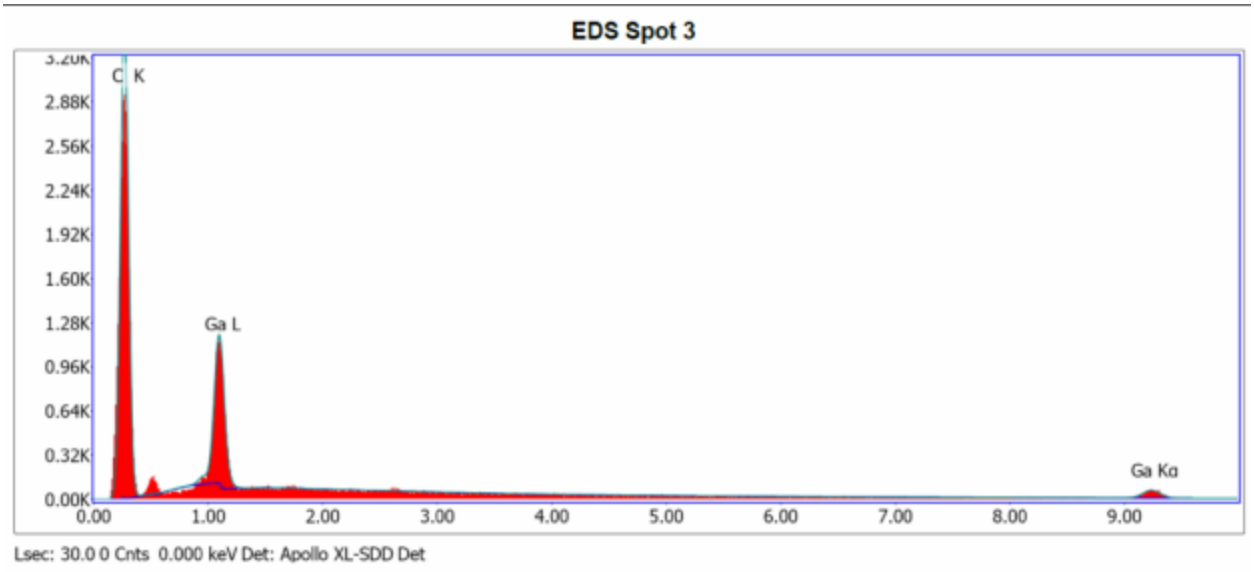

Figure 41. Image of EDAX point (3) analysis of the PVA/MMT film on a Mylar substrate. The lack of Al and Si indicates it is the Mylar substrate.

Table 6. Calculated film thickness for a film created from a solution of PVA & MMT.

PVA & MMT			
Ink Solution Density g/cm^3	Bi-Layers	Film Weight g	Film Thickness µm
1.800	1	0.00006	2.90
1.800	2	0.00009	4.35
1.800	3	0.00014	6.77
1.800	4	0.00019	9.19
1.800	5	0.00024	11.60
1.800	6	0.00028	13.54

Since it was determined the drops were coalescing, leading to large voids between the drops, it was determined that a PVP base coat would provide better drop formation. For the layered films produced to test for potential application, the PVP base was used.

The results of the permeability of both the PVA/MMT nanoclay (with and without the PVP base) are given below in Table 7.

Table 7. Oxygen Transmission rates for films created from a solution of PVA & MMT with no PVP base coat and with a PVP base coat.

PVA & MMT LAYERED	$cm^3/m^2/24hr/mil$	% REDUCTION	PVA&MMT WITH PVP BASE COAT	$cm^3/m^2/24hr/mil$	% REDUCTION
Mylar no coating	5.3		Mylar no coating	5.3	
1 BI-LAYER	4.9	8%	1 BI-LAYER	4.1	23%
2 BI-LAYER	4.8	9%	2 BI-LAYER	3.9	26%
3 BI-LAYER	4.7	11%	3 BI-LAYER	3.7	30%
4 BI-LAYER	4.6	13%	4 BI-LAYER	3.5	34%
5 BI-LAYER	4.6	13%	5 BI-LAYER	2.9	45%
6 BI-LAYER	4.5	15%	6 BI-LAYER	2.5	53%

Compared to the 6 bi-layer without the PVP base, the films that were applied to a substrate that had a PVP application exhibited greater barrier strength. The thickest film, with twelve layers of alternating PVA and MMT clay on a PVP base, has an oxygen transmission level of $2.5cm^3/m^2/24hr/mil$. Depending on the industry and application, this may or may not be an acceptable transmission rate.

5.3 PEG and MMT Clay

Printing the PEG/MMT nanoclay films directly onto the Mylar substrate produced similar issues as those which had been encountered with PVA. Drop dispersion (as viewed through the fiducial camera) was poor. The decision was made to print the films for testing on a substrate treated with PVP as had to be done with the PVA. The permeability results for the PEG/MMT clay (both with and without a PVP base on the Mylar substrate) are given in Table 8.

Table 8. Oxygen Transmission rates for films created from a solution of PEG & MMT with no PVP base coat and with a PVP base coat.

PEG & MMT LAYERED	$cm^3/m^2/24hr/mil$	% REDUCTION	PEG&MMT WITH PVP BASE COAT	$cm^3/m^2/24hr/mil$	% REDUCTION
Mylar no coating	5.3		Mylar no coating	5.3	
1 BI-LAYER	5.0	6%	1 BI-LAYER	5.0	6%
2 BI-LAYER	4.9	8%	2 BI-LAYER	4.9	8%
3 BI-LAYER	4.9	8%	3 BI-LAYER	4.9	8%
4 BI-LAYER	4.8	9%	4 BI-LAYER	4.7	11%
5 BI-LAYER	4.5	15%	5 BI-LAYER	4.5	15%
6 BI-LAYER	4.5	15%	6 BI-LAYER	4.5	15%

The PVP base made little or no difference in the permeability results for PEG and MMT nanoclay. It is obvious by looking at the table there was a minimal change in the oxygen barrier properties regardless of use of PVP. Figures 42 and 43 show the difference in a sample printed with and without a PVP base coat on the Mylar substrate at 1 bi-layer and 6 bi-layers.

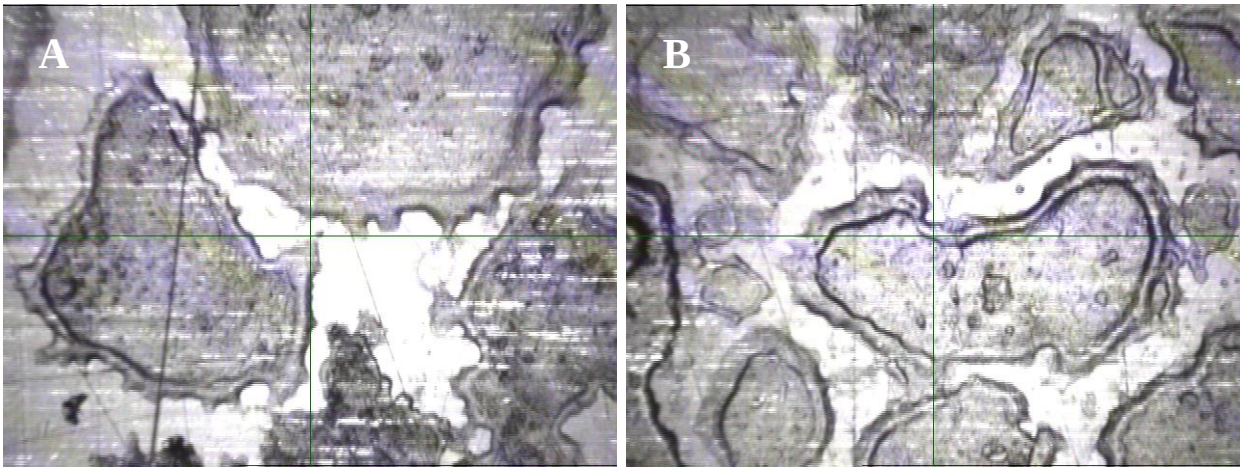

Figure 42. Images of films created from a solution of PEG & MMT indicating the effects of film formation with no PVP base coat. (A) 1 bilayer and (B) 6 bi-layers.

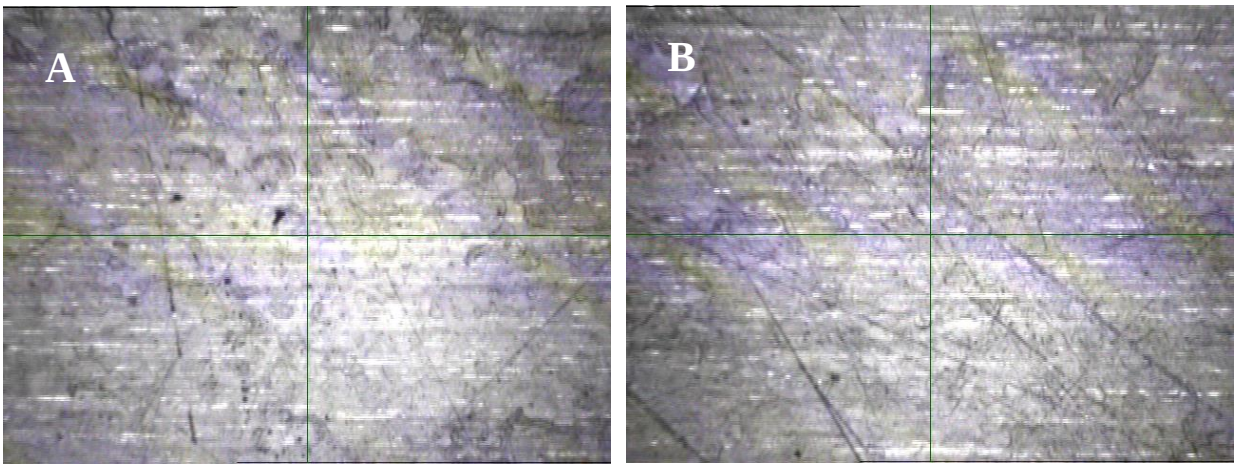

Figure 43. Images of films created from a solution of PEG&MMT indicating the effects of film formation with a PVP base coat. (A) 1 bilayer and (B) 6 bi-layers.

There is little or no uniformity in the films with no PVP base. Drop dispersion is erratic and leaves large voids between drops. Layers placed on the PVP base coat appear more uniform with signs of coalescence, rather than dispersion. This is due to drop contact angles and surface energies.

Due to the permeability data, it was determined this would not be an acceptable oxygen barrier film. Thickness does not matter as there was no increased benefit associated with additional bi-layers of material, up to 6 bi-layers. Table 9 illustrates the calculated film thickness for each bi-layer.

Table 9. Calculated thickness of films created from a solution of PEG & MMT.

PEG & MMT			
Ink Solution Density g/cm³	Bi-Layers	Film Weight g	Film Thickness µm
1.800	1	0.00007	3.50
1.800	2	0.00009	4.50
1.800	3	0.00014	7.00
1.800	4	0.00021	10.50
1.800	5	0.00026	13.00
1.800	6	0.00030	15.00

5.4 Graphenol and MMT Clay

Like the PVA and the PEG, the Graphenol exhibited the tendency to bead up when applied directly to the Mylar substrate. The permeability results for the Graphenol/MMT clay solution applied directly to the Mylar substrate with and without a PVP base coat are given in Table 10.

Table 10. Oxygen Transmission Rates of films created from a solution of Graphenol & MMT.

GRAPHENOL & MMT LAYERED	cm³/m²/24hr/mil	% REDUCTION	GRAPHENOL & MMT WITH PVP BASE COAT	cm³/m²/24hr/mil	% REDUCTION
Mylar no coating	5.3		Mylar no coating	5.3	
1 BI-LAYER	4.9	8%	1 BI-LAYER	4.2	21%
2 BI-LAYER	4.7	11%	2 BI-LAYER	4.1	23%
3 BI-LAYER	4.6	13%	3 BI-LAYER	4.1	23%
4 BI-LAYER	4.4	17%	4 BI-LAYER	4.0	25%
5 BI-LAYER	4.1	23%	5 BI-LAYER	3.8	28%
6 BI-LAYER	4.0	25%	6 BI-LAYER	3.7	30%

Based on the results, the PVP base coat made a marginal difference in the oxygen barrier properties of the film. Figures 44 & 45 below shows a Graphenol/MMT clay

sample with 1 and 6 bi-layers printed both with and without a PVP base on the Mylar substrate.

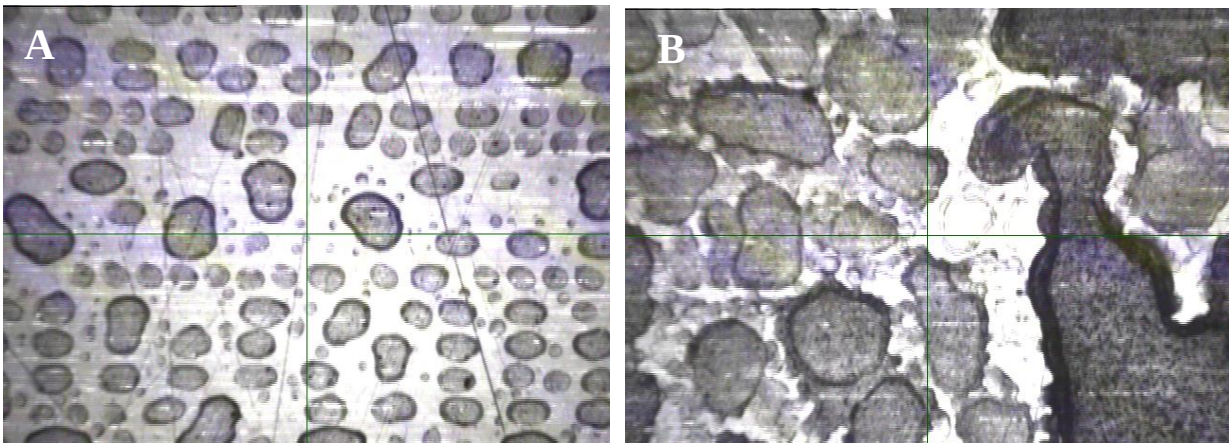

Figure 44. Images of films created from a solution of Graphenol & MMT indicating the effects of film formation with no PVP base coat. (A) 1 bi-layer and (B) 6 bi-layers.

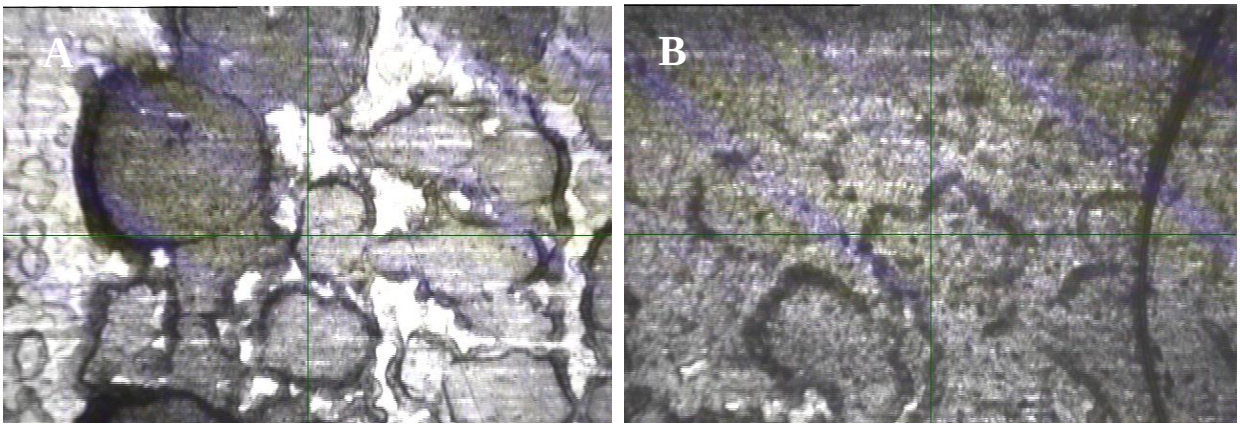

Figure 45. Images of films created from a solution of Graphenol & MMT indicating the effects of film formation with a PVP base coat. (A) 1 bi-layer and (B) 6 bi-layers.

It is visually apparent that none of these films is uniform. Permeability results indicate they exhibit poor oxygen barrier capabilities. It is believed the pH level in the humic acid could impact the bonding between the clay and the Graphenol. It could also

affect the surface energy and droplet contact angle between the substrate and Graphenol droplets, leading to non-uniform dispersion.

Due to the permeability data, it was determined this would not be an acceptable oxygen barrier film. Thickness does not matter in this instance, as there was no increased benefit associated with additional bi-layers of material, up to 6 bi-layers.

5.5 Wide Angle X-ray Scattering (WAXS) Results and Analysis

The printed films were analyzed using WAXS to determine if any reflections could be located giving an indication of the level of intercalation and ordering taking place. The samples were analyzed using a scanning range of 1 to 35 degrees. The first film to be scanned was the 6 bi-layer PVP/MMT. The scan indicated a very highly ordered system with an average d spacing of 58Å. The remaining PVP/MMT films were scanned using the same settings and all of them produced results similar to the 6 bi-layer film sample.

All of the PVP/MMT films indicated a very highly ordered system with ten to eleven reflections. The high amount of ordering is believed to be due to the self-assembly of ordered layers of clay intercalated by PVP mediated by ion-dipole bonding to the exchangeable cation on the montmorillonite surface. The intercalation being driven by displacement of waters of hydration on the sodium cations by the polymer molecules. The entropy decrease for every PVP molecule when intercalating is more than offset by the entropy increase of the multiple moles of water displaced. The results of the scans can be seen in Figures 46 to 51.

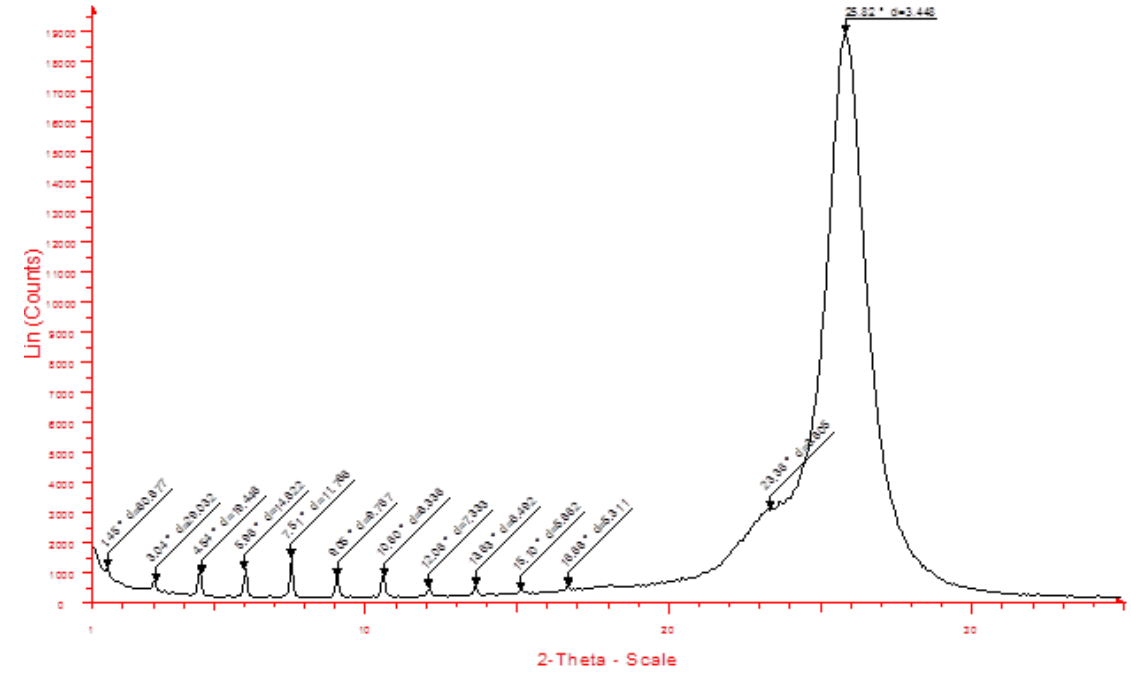

Figure 46. Wide Angle X-ray Scattering results for a 1 bi-layer film created from a solution of PVP & MMT.

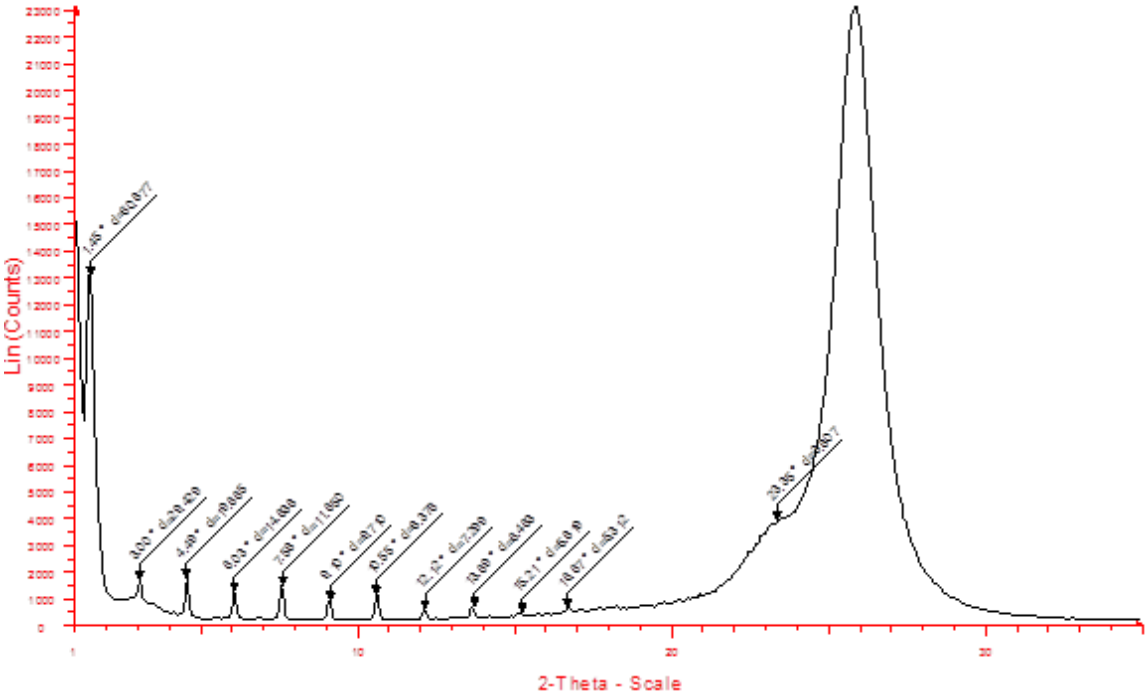

Figure 47. Wide Angle X-ray Scattering results for a 2 bi-layer film created from a solution of PVP & MMT.

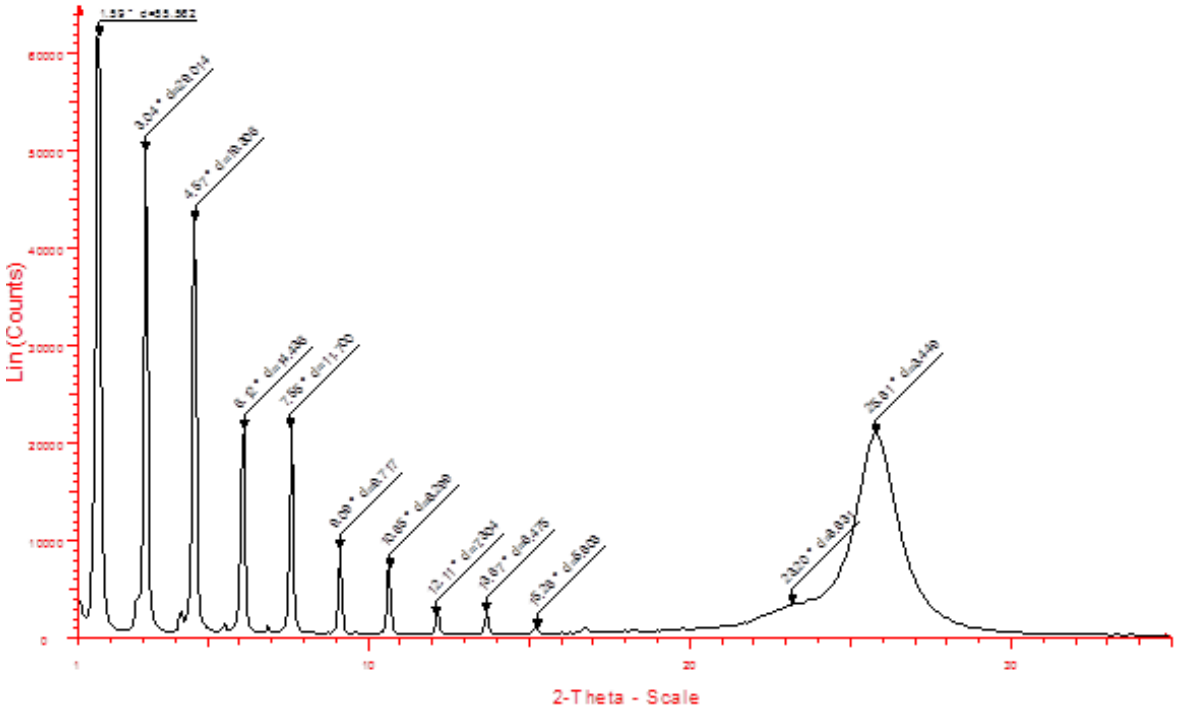

Figure 48. Wide Angle X-ray Scattering results for a 3 bi-layer film created from a solution of PVP & MMT.

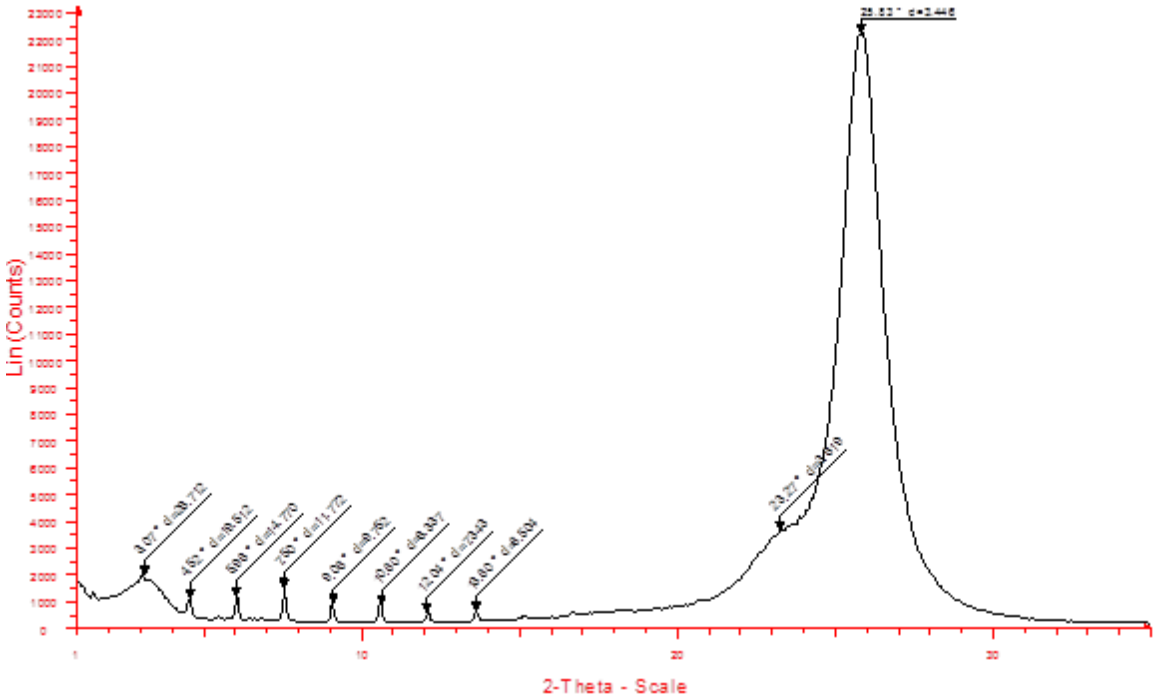

Figure 49. Wide Angle X-ray Scattering results for a 4 bi-layer film created from a solution of PVP & MMT.

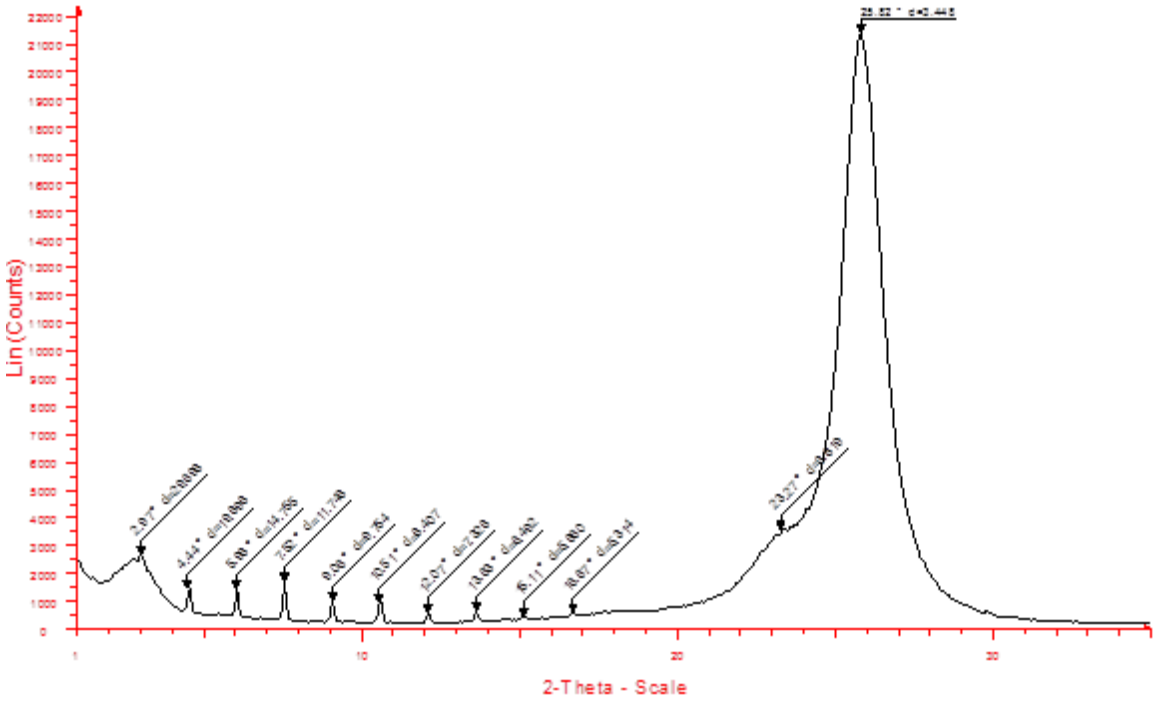

Figure 50. Wide Angle X-ray Scattering results for a 5 bi-layer film created from a solution of PVP & MMT.

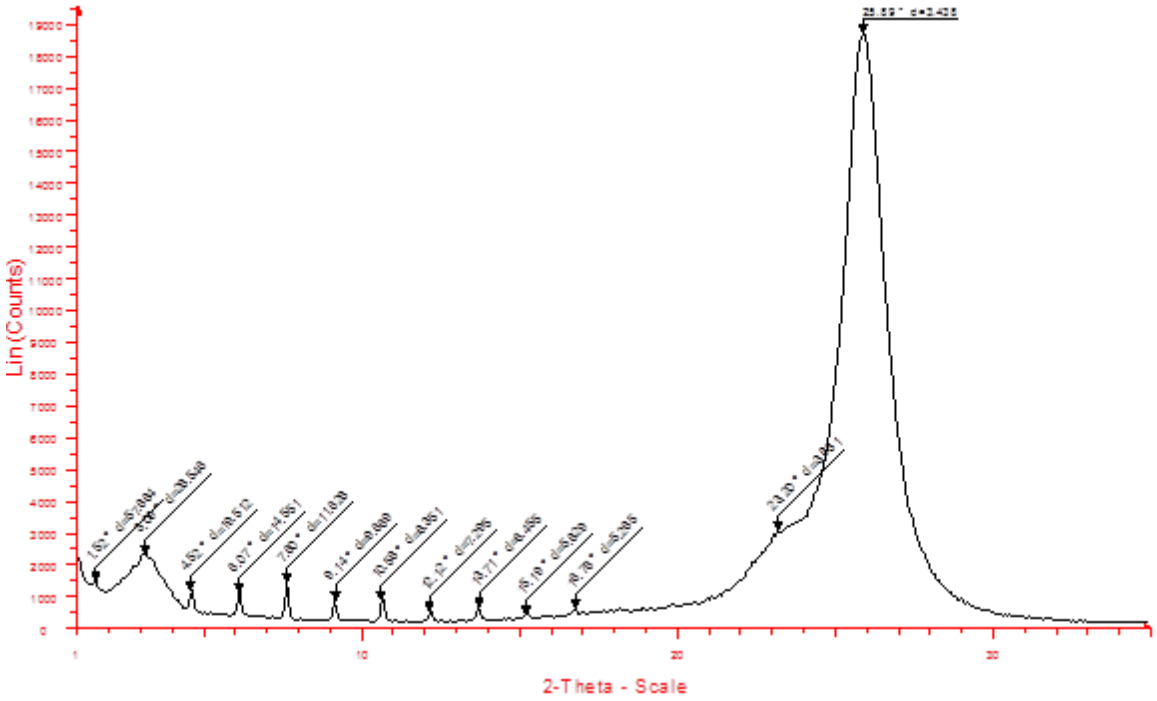

Figure 51. Wide Angle X-ray Scattering results for a 6 bi-layer film created from a solution of PVP & MMT.

The PVA/MMT and PEG/MMT films were also scanned to determine if they contained a similarly ordered structure. The scans indicated what would be expected from a traditional polymer/clay composite film; there was no highly ordered system as in the case of the PVP/MMT films. In the case of PEG and PVA, these polymers are very flexible and can bond plate to plate limiting the gallery spacing to a relatively small value. This results in a tactoid structure with large amounts of polymer unintercalated. The results of the PVA and PEG scans can be seen in figures 52 and 53. Figure 54 is a scan of the Mylar substrate without any coating, this was done to confirm the large peak on all of the scans was coming from the Mylar substrate.

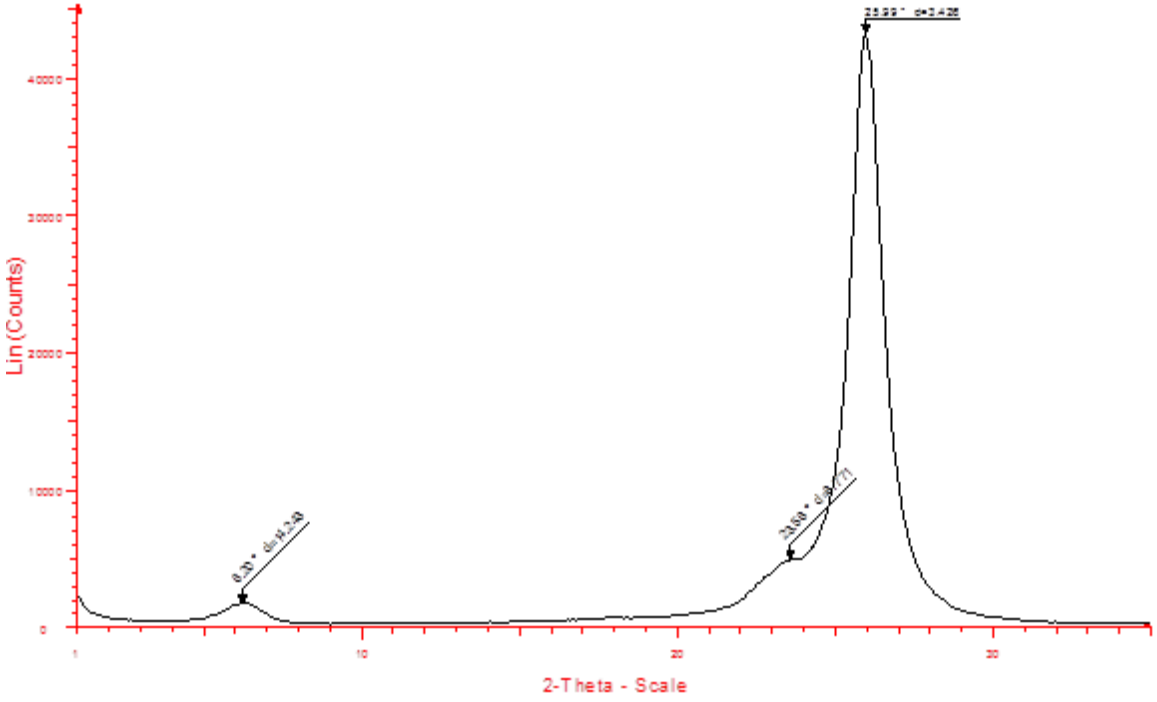

Figure 52. Wide Angle X-ray Scattering results for a 6 bi-layer film created from a solution of PVA & MMT.

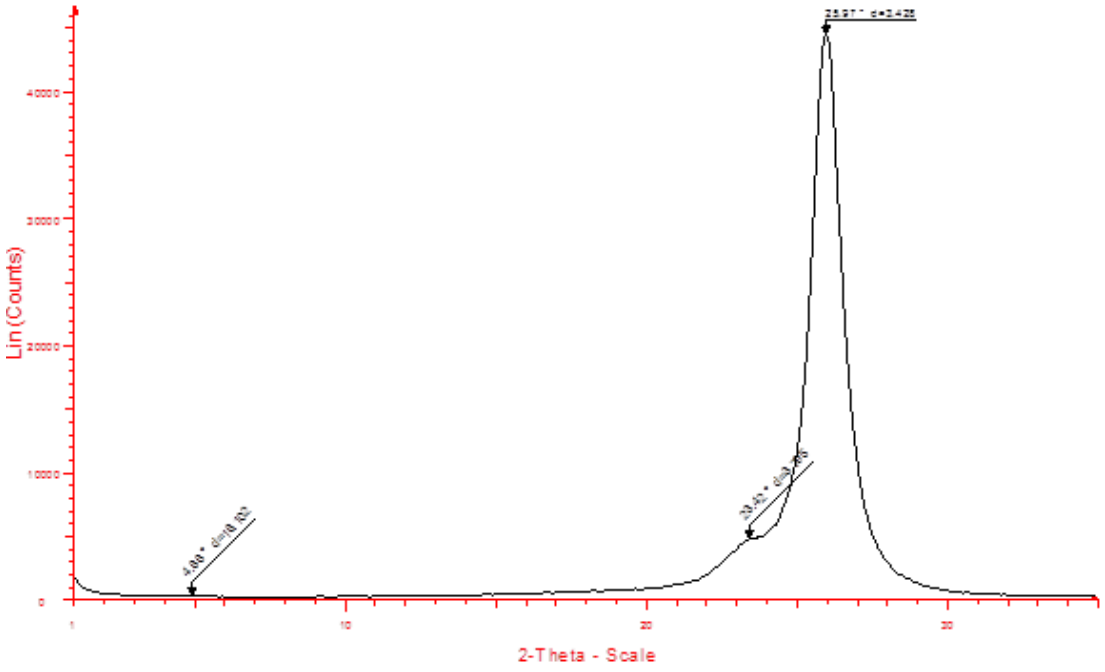

Figure 53. Wide Angle X-ray Scattering results for a 6 bi-layer film created from a solution of PEG & MMT.

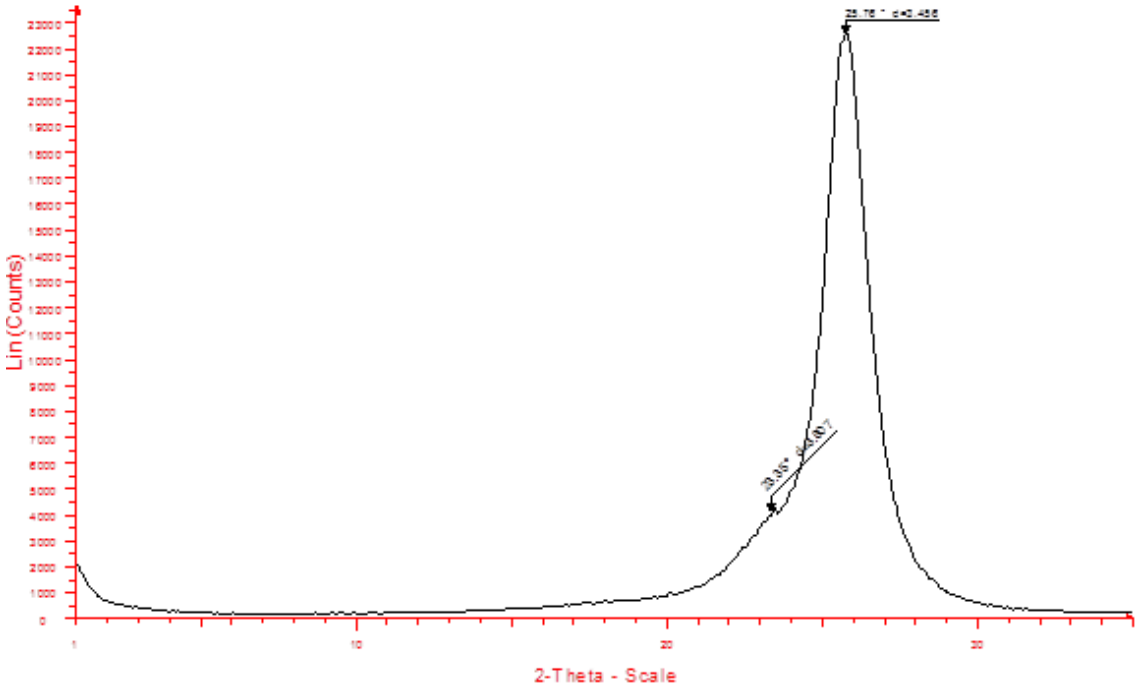

Figure 54. Wide Angle X-ray Scattering results for a Mylar substrate without any coating.

CHAPTER 6

Conclusions

6.1 Summary

Films consisting of PVP & MMT, PVA & MMT, PEG & MMT, and Graphenol & MMT could be printed with a Dimatix 2831 3D DOD materials printer. The films with the best properties were produced without any platen heat. Adding heat slowed or prevented the bonding action between the polymers and MMT nanoclay.

It was possible to be print films consisting of various polymers and Graphenol. Some of films such as the PVP/MMT and PVA/MMT/PVP produced better films and gas barrier properties than the PVA/MMT and PEG/MMT. Figure 46 illustrates the oxygen transmission rates for each film that was printed.

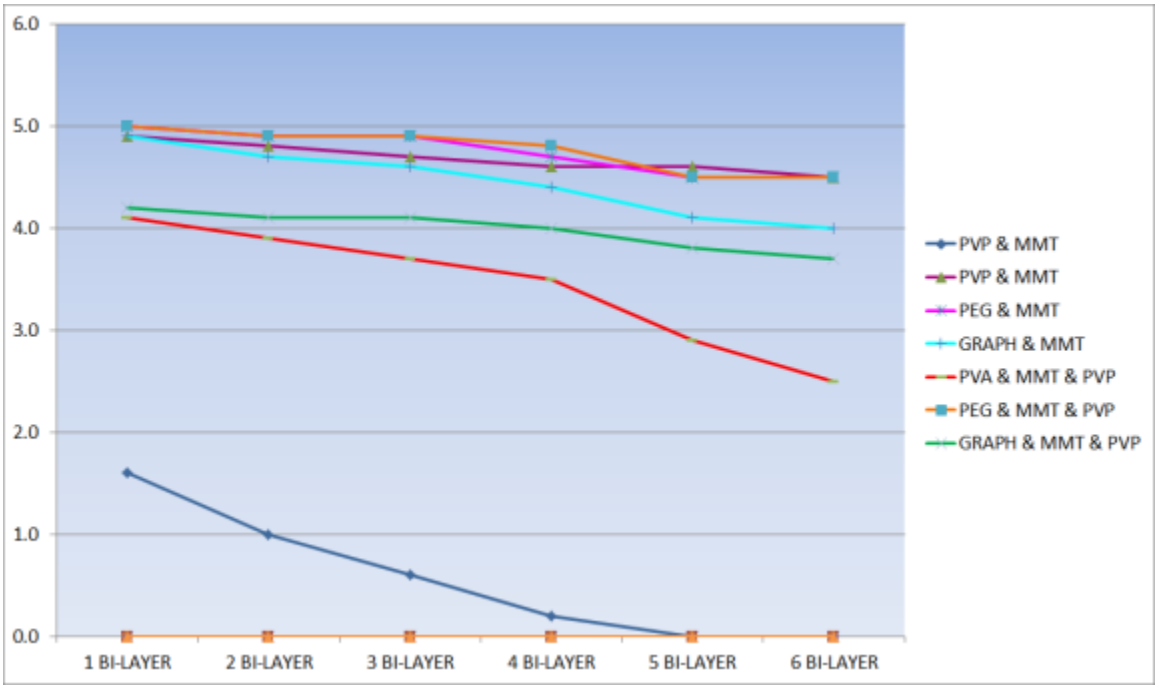

Figure 55. Oxygen transmission rate comparison of films made with a DOD printer.

From the graph above, the film consisting of PVP & MMT exhibits the best gas barrier properties. In addition to producing the best barrier results, it produced the most uniformed and transparent film. The properties of the PVP & MMT film are due to its bonding interactions with the MMT nanoclay and its ability to interact with the Mylar substrate.

Although the PVA & MMT films without a base coat of PVP did not produce films with good barrier properties, it was discovered that adding a base layer of PVP prior to printing vastly improved the films uniformity and oxygen transition rate, making it a viable oxygen barrier film. The PVA & MMT films had to be produced with an ink solution of a lower weight percentage due to is higher viscosity and extreme tackiness, which plugged up the printing nozzles.

The film thickness of all the films ranged from 2.90 to 15.19µm, Table 11 lists the thickness value of each bi-layer for each polymer MMT nanoclay ink solution. The thinner films for PVA & MMT are believed to be from the lower weight percentage needed in order to print the ink solution.

Table 11. Film thickness values for each bi-layer

	PVP & MMT	PVA & MMT	PEG & MMT
Bi-Layers	Film Thickness µm	Film Thickness µm	Film Thickness µm
1	3.92	2.90	3.50
2	5.39	4.35	4.50
3	7.84	6.77	7.00
4	10.78	9.19	10.50
5	13.23	11.60	13.00
6	15.19	13.54	15.00

The research proved that it is possible to print films made of PEG & MMT and Graphenol & MMT. They would not be viable gas barriers. The films were not uniformed with or without a PVP base layer and there were a lot of void areas between the droplets due to coalescence, drop contact angles, and surface energies.

6.2 Commercialization Potential

Based on the barriers film market growth predicted by Smithers pria, (See Appendix VI for details), films produced by DOD printing should be well accepted in the market place. The study indicates the growth is being driven by a number of key trends ranging from socio-economic, demographic and lifestyle changes to the development of new materials, innovations in existing materials and emerging trends within end-use segments.

The study states that the polymer materials used for the manufacture of transparent barrier films can be grouped into three broad categories, barrier base web materials, barrier polymers and inorganic barrier materials.

In a different report Smithers claims the global high barrier packaging film consumption is at approximately 1.76 million tonnes in 2014 with a value of $15.9 billion and is forecasted to grow at a CAGR of 5.0% between 2014 and 2019.

The report claims the innovation in and implementation of smart and active packaging over the next 10 years will be the key disruptive factor affecting the flexible packaging industry. These technologies have been retarded by high cost, consumer resistance to items such as sachets in packaging, and concerns about excessive packaging.

The deployment of intelligent packaging is expected to become more frequent with decreasing cost, increasing emphasis on food safety, anti-counterfeiting, new regulations, and brand owner/consumer demand. The DOD printed films should do well in this arena.

The global specialty films market was worth $22.4 billion in 2013 and is forecast to grow 5.4% annually to reach $29.1 billion by 2018. The range of specialty films on the market is broad, with very different properties and functions adding value for the consumer. Film types are also at different stages of development, exhibit different supply/demand dynamics, and growth potential.

6.3 Limitations

The biggest limitation in printing the films was producing ink solutions dilute enough to from droplets with the DMC-11601 print head designed for the Dimatix 2831 printer. Larger print nozzles would have made it easier to print the viscous polymers and MMT nanoclay ink solution.

6.4 Future Work

Due to the positive results of placing a PVP base coat on the Mylar substrate prior to printing the PVA films, future research should investigate the results of adding multiple layers of PVP prior to printing PVA, PEG, and other materials. DOD Printers equipped with larger print head nozzles should be utilized to identify the effects of film formation utilizing larger droplets and a more viscous ink solution.

Additional substrate materials should be tested to determine the effect of film formation based on substrate material. Additional research should be conducted on the films mechanical properties to determine their durability.

APPENDIX SECTION

Appendix I

Dimatix DMP 2831 DOD Printer Cartridge Settings

2.0 Cartridge Settings

In the start up procedure we showed you how to select a file with a preset cartridge setting that had been predetermined for the test fluid by FUJIFILM Dimatix. Now we will get into the details of the settings and the editor screens.

Click on the **Edit** button in the **Cartridge Settings** box to display the following screen.

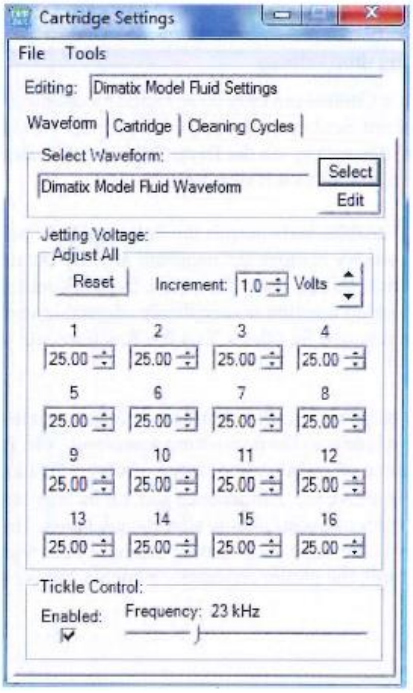

Figure 4 - 5 Cartridge Settings screen

In the above window you can load a previously created cartridge setting file from the **File** menu. You can also save your cartridge setting files

2.1 Waveform Tab

From the **Waveform** tab the voltage of each nozzle can be individually adjusted by typing a number in the individual nozzle box or by clicking on the up or down arrow in the nozzle box. You may want to do this to adjust drop velocities of individual nozzles, since velocity

Figure A1-1. Page 23 of operations manual for Dimatix DMP 2831 Printer.

is a function of voltage (see Figure 8-5). You can also change all of them simultaneously with the **Adjust All** arrows. *(See Waveform Editor for effects of voltage on jetting).* The **Increment** number is the amount the voltage will change with one click on the up or down arrow buttons. The **Waveform** tab displays the active waveform. You can load previously saved waveforms using the **Select** button or you can edit the active waveform using the **Edit** button.

Note: Once you have established the settings for a particular fluid, you may have to adjust the voltages for a new cartridge to match the drop velocity of a previous cartridge. See **Drop Watcher** for instructions on setting drop velocity.

Note: Tickle Control can only be accessed by opening the cartridge settings of the Print Set-Up screen in the **DDM** main window. Opening the cartridge setting via the **Drop Watcher** does not allow you to change tickle control as it is displayed in gray.

The **Tickle Control** enables and controls the low amplitude pulse that is given to the nozzle periodically simply to move the meniscus slightly but not eject a drop. For certain jetting materials this prevents the nozzle from "skinning over" due to fluid evaporation. The "tickle" function is completely adjustable and, is very important for some fluids and not required for others. Test this function with your fluid before setting it as a default.

The low amplitude pulse that tickle control sends to the nozzle can be modified in the **Waveform Editor** window as the non-jetting waveform. The frequency set in tickle control is always active when the printer is not printing. This includes the times during which the carriage is above the maintenance pad, on its way to the selected print area, or on its way back from one print pass to start the next pass. However, during printing, the tickle frequency is the same as the jetting frequency set with the waveform editor. So during one print job, the printer repeatedly switches between the two pulses.

Figure A1-2. Page 24 of operations manual for Dimatix DMP 2831 Printer.

2.2 Cartridge Tab

If you click on the **Cartridge** tab in the **Cartridge Settings** window, the following screen displays.

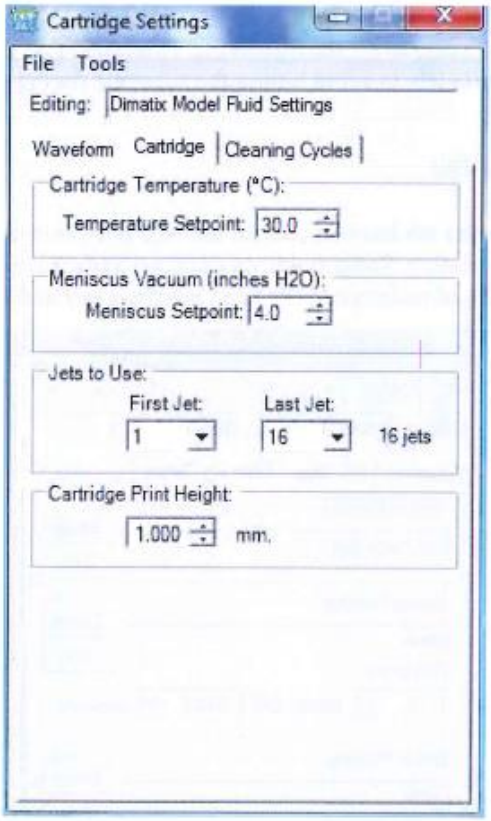

Figure 4 - 6 Cartridge Settings – Cartridge Tab

This screen lets you set the **Cartridge Temperature**. This is usually used when the fluid is too viscous to jet and you need to lower the viscosity by raising the temperature to get the desired jetting performance.

Also on this window is the setting for **Meniscus Vacuum**. Ink jetting devices operate under negative pressure to keep the meniscus at the edge of the nozzle. You may need to adjust this depending on the viscosity and surface tension of your fluid. Four inches of water is a typical value. Having the correct meniscus vacuum level usually affects the high frequency performance of the fluid you are jetting.

The **Jets to Use** function allows you to select the range of nozzles you wish to use to jet your pattern, if you want to use fewer than all sixteen. The software automatically

Figure A1-3. Page 25 of operations manual for Dimatix DMP 2831 Printer.

compensates for the number of nozzles used but the nozzles selected can only be one series of adjacent nozzles.

The **Cartridge Print Height** sets the distance of the printhead above the substrate. It can be adjusted from .250 mm to 1.50 mm.

Note: Take care to set the **Substrate Thickness** and **Cartridge Print Height** accurately to avoid hitting the substrate during printer operation.

2.3 Cleaning Cycles Tab

The **Cleaning Cycles** tab lets you control how the print cartridge is cleaned before, during, and after printing. Some fluids do not need periodic maintenance, while others need a high amount of maintenance to keep nozzles clear and functioning properly.

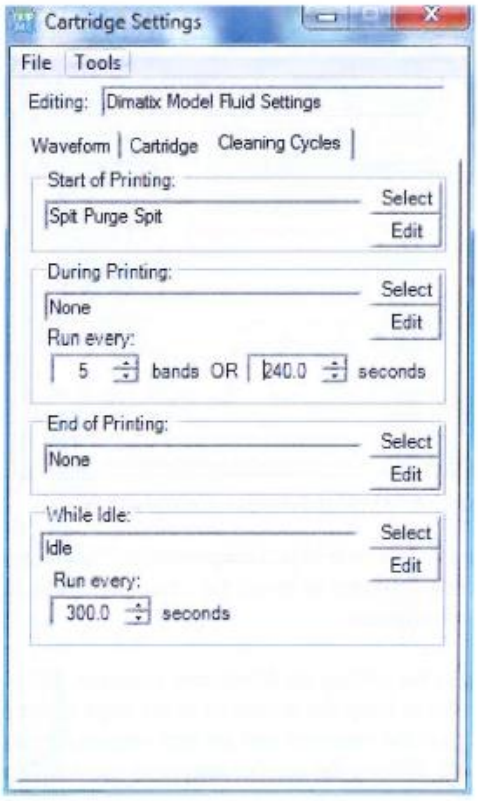

Figure 4 - 7 Cartridge Settings – Cleaning Cycles tab

Figure A1-4. Page 26 of operations manual for Dimatix DMP 2831 Printer**.**

- **Select** button – lets you select an existing cycle in the cleaning cycle folder.
- **Edit** button – lets you edit that cycle with the editor window.
- **Start of Printing** – refers to the cleaning you want to do at the beginning of the print. Select a cycle you wish to run to enter one in that box or you can edit an existing file with the **Edit** button.
- **During Printing** – refers to the cleaning cycle you want to run while printing your pattern. This can be set to run every so many number of **Bands** (*one cycle of the carriage across the platen and back is a band*) or every so many **Seconds** of printing time. Select a cycle you wish to run by clicking on **Select** and choose one from the folder or you can edit an existing one with the **Edit** button. Whichever is more frequent between **Run every** x **Bands OR Seconds** (depending on printing speed) is the cycle that is used **During Printing.**
- **End of Printing** – refers to the cleaning you would like to do at the end of your printing. Select a cycle you wish to run to enter one in that box or you can edit with the **Edit** button.
- **While Idle** – refers to any cleaning you would like to do while the system is not printing but is on and you have a cartridge installed. Select a cycle you wish to run to enter one in that box or you can edit with the **Edit** button.
- **None** – is a preexisting empty cleaning cycle that you can use in order for the printer to not do any cleaning during that time.
- **0** – can be entered where numbers are required to indicate not to run that cycle.

3.0 Cleaning Cycle Editor

The **Cleaning Cycle Editor** is run

- by clicking the **Edit** button next to any of the cleaning cycles or
- by selecting **Cleaning Cycle Editor** from the **Tools** menu in the **Cartridge Settings** window or the DDM Main screen or
- by selecting the **Cleaning** group in the **Drop Watcher** window.

Figure A1-5. Page 27 of operations manual for Dimatix DMP 2831 Printer**.**

From this editor you can create sequences of operations that can be saved as a cleaning cycle file. Refer to the **Cartridge Maintenance** section in the back of the manual for more details. The default cleaning cycle, **Spit Purge Spit**, is shown below.

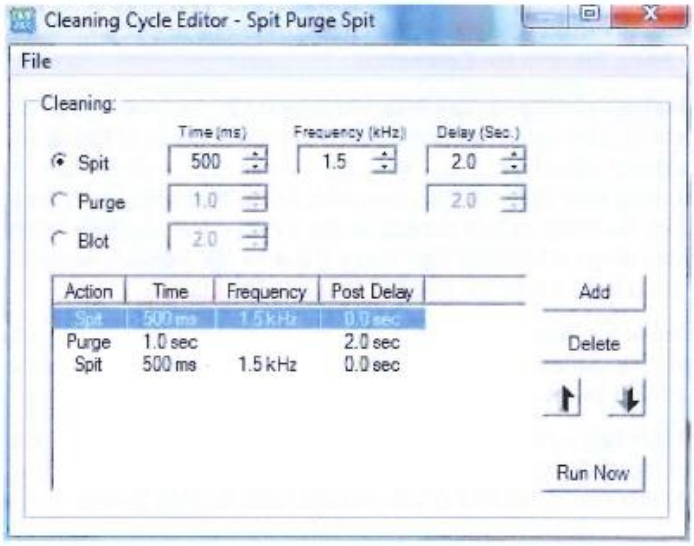

Figure 4 - 8 Cleaning Cycle Editor screen

- **Spit** – refers to jetting the nozzles for the designated time at the given frequency.
- **Purge** – refers to pushing fluid out through the jetting device with pressure (system is preset to 5psi). This process is usually used to get air out of the jetting device.
- **Blot** – refers to the cartridge simply coming down and making contact with the cleaning pad for the designated time. As the nozzle plate is recessed into the cartridge it does not touch the cleaning pad. The cleaning pad gets close enough to absorb fluid residue on the nozzle plate.

  Note: It is important to make sure that the cleaning pad is not saturated or clogged to ensure good removal of the fluid from the nozzles after purging or spitting.

- **Delay** time – is the time after the cleaning before going to the next step in the cycle.

A cleaning cycle can be very simple, such as a "2 second blot" or they can consist of several combinations of actions (spitting, purging, and blotting) with varying times.

Here is how to create a cleaning cycle:

1. Click on the **Spit**, **Purge**, or **Blot**.

Figure A1-6. Page 28 of operations manual for Dimatix DMP 2831 Printer

2. Then enter a number or use the arrows for the **Time**, **Frequency** or **Post Delay** that you want.
3. Click the **Add** button to enter it into the table and incorporate it into the cycle.
4. If you want another action to occur next, simply repeat the process.
5. If you want to delete a step, highlight it in the table by clicking on it, then click the **Delete** button.
6. When you have built your cleaning cycle, **Save** it with a name that describes what it does using the **Save As** from the **File** menu.

If desired you can run the cleaning cycle you just created by clicking on the **Run Now** button in the **DDM** main window.

Figure A1-7. Page 29 of operations manual for Dimatix DMP 2831 Printer

4.0 Waveform Editor

The waveform editor is where you make changes to the waveform by adding or deleting segments, make changes to the segments, or rescale a waveform.

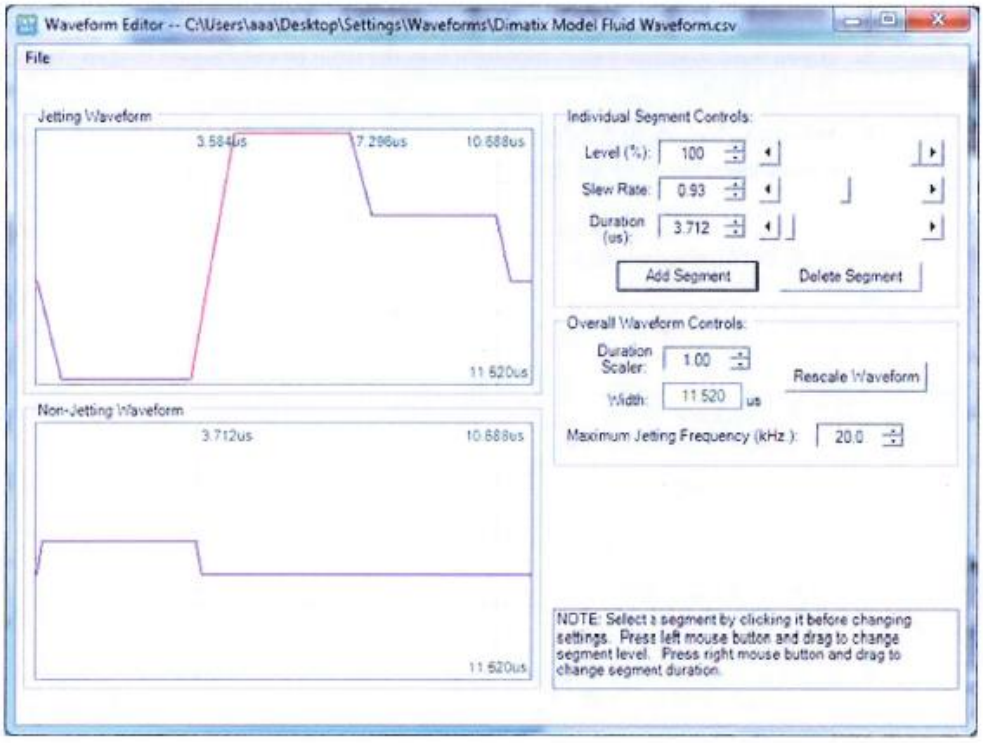

Figure 4 - 9 Waveform Editor screen

This is the control screen for the electrical signal that triggers the drop ejection. This signal is shown in the **Jetting Waveform** section. The signal consists of multiple segments (four in the above example). To adjust a segment, simply point your with your mouse and click on it. The selected segment changes from blue to red.

The *Waveform Basics* chapter, later in this manual, describes how changing the waveform affects drop ejection. There is an application note available through the Tech Support link at the bottom of the FUJIFILM Dimatix home page that elaborates on this topic.

Figure A1-8. Page 30 of operations manual for Dimatix DMP 2831 Printer.

4.1 Individual Segment Controls

In this group you have several parameters at your control. If you want to modify a segment, click on that segment in the graph with the mouse to highlight it. Now modify the parameters for it by typing in a number, using the up/down arrows or slider bar.

Level – This is the percent of the amplitude relative to the value specified in the **Cartridge Settings Waveform** screen.

Slew Rate – This is the slope of the line in the waveform during voltage ramps.

Duration – This is the length (in time) of the segment.

You can add waveform segments to optimize drop ejection. Click on the segment that you want to place a new segment in front of and click the **Add** button. You can now modify that segment as you would the others. You can delete a segment simply by clicking on it and selecting the **Delete** button.

Note: The duration and the level of a segment can also be modified by holding down the mouse button and moving the mouse. Hold down the **left** mouse button and move the mouse up or down to modify the level of a segment. Hold down the **right** mouse button and move the mouse left or right to adjust the duration of a segment. These instructions are in the box to the right of the graph.

4.2 Overall Waveform Controls

Duration Scaler – This feature allows the user to easily scale the entire waveform pulse width at once. This is useful when you are using fluids with different densities. Fluids with higher densities generally need longer pulses. Enter a number in the box then click the **Rescale Waveform** button. The entire waveform's width changes by multiplying its current width by the **Rescale** number. For example, if you enter 1.1 in the **Duration Scalar** box, it adjusts each waveform segment's length proportionally to multiply the waveform's overall width by 1.1, which is a 10% increase.

Width – This box displays the overall pulse time width for the entire waveform.

Maximum Jetting Frequency – The maximum jetting frequency is established by the user during initial fluid characterization using the drop watcher system. During initial characterization the maximum frequency of 80 kHz should be entered into the waveform file being loaded. This value dictates the scale for the **Jetting Frequency Maximum** in the **Drop Watcher** window. After the user has established the maximum sustainable jetting frequency in the drop watcher **it is essential** to ensure the maximum jetting frequency

Figure A1-9. Page 31 of operations manual for Dimatix DMP 2831 Printer.

Appendix II

Dimatix DMP 2831 Drop Watcher Settings

Chapter **6**

Drop Watcher

1.0 Drop Watcher

In the bottom left of the main **DDM** window is the **Drop Watcher** button. Clicking on it moves the carriage to the right side of the platen, positioning the nozzles over the drop watcher camera system. This system allows direct viewing of the jetting nozzles, the faceplate surrounding the nozzles, and the actual jetting of the fluid. The **Cartridge Settings** window also comes up at this time to allow you to modify the waveform and view the changes in jetting characteristics.

Note: **Tickle Control** is not active (displayed in gray) when you open the **Cartridge Settings** window via the drop watcher. In order to be able to change tickle control, open the cartridge settings window directly by clicking the **Edit** button in the **Print Setup Tab** in the **DDM**.

Figure A2-1. Page 61 of operations manual for Dimatix DMP 2831 Printer**.**

Figure 6 - 1 Drop Watcher screen

1.1 Jetting Nozzle Box

Once the carriage and cartridge are in position, click on the **Jetting Nozzle** box – number 8 should be in the box. When you click on it, the system brings nozzle number 8 of the cartridge into the center of the screen. You can then increment up or down to different nozzles and the system moves that nozzle into center position in the screen. There is also a row of the nozzle numbers across the screen in which you can turn any of them on or off.

Figure A2-2. Page 62 of operations manual for Dimatix DMP 2831 Printer**.**

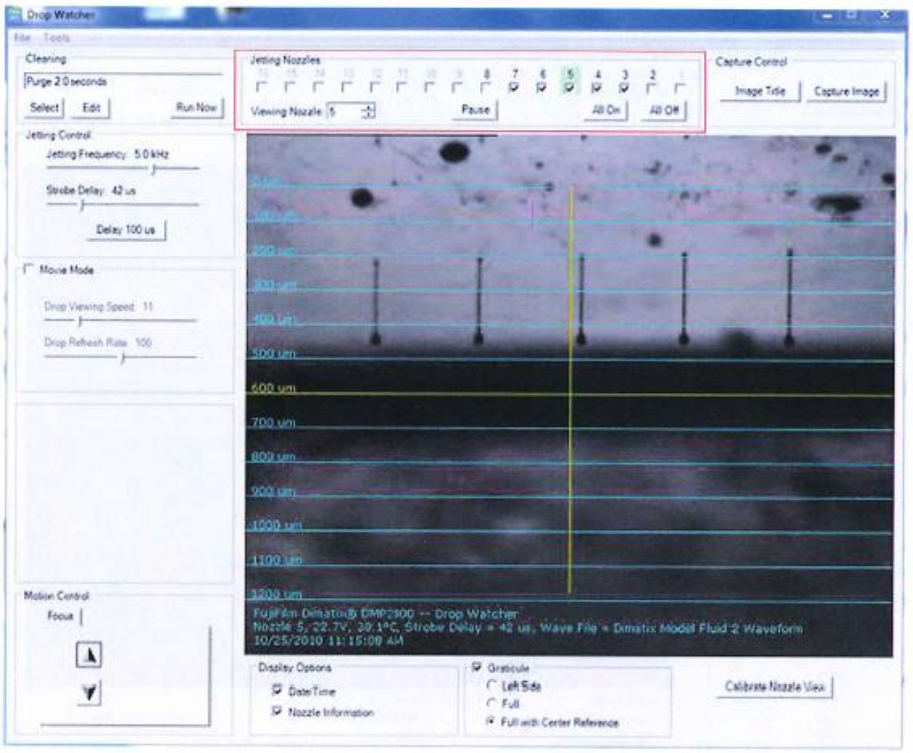

Figure 6 - 2 Jetting Nozzles box

By clicking the box associated with each nozzle it ejects drops out of that nozzle or turns it off. By right clicking a box, the nozzle moves to center position. The nozzle in center position always has a green shade. To minimize spraying off of the absorbent **Drop Watch Pad,** the user interface limits selecting jetting nozzles to the four surrounding the **Viewing Nozzle**.

1.2 Calibrate Nozzle View

The **Calibrate Nozzle View** feature automatically controls the stage motion to keep the nozzles in line when drop watching regardless of the cartridge angle. To perform this operation use the following procedure:

Figure A2-3. Page 63 of operations manual for Dimatix DMP 2831 Printer**.**

Start by clicking on the **Calibrate Nozzle View** button in the lower right of the **Drop Watcher** screen.

Figure 6 - 3 Calibrate Nozzle View button

1. Find nozzle 1 (the right most orifice), put the mouse pointer on the nozzle and click-drag it to the cross-hair on the screen. Use the focus buttons as necessary to refine the nozzle's focus.
2. Click the **Next** button and drag the image to the right until nozzle 16 (the left most nozzle) is under the cross-hair. Use the focus buttons again as necessary to refine the nozzle's focus.
3. Click the **Next** button again and you are done calibrating the nozzle view. Now, when you select any nozzle from one to sixteen, the selected nozzle should be close to the 0 line opening and in focus.

For the stage to move the selected nozzle into position you must index through the nozzles using the **Jetting Nozzle** box. When you open the drop watcher it tries to

Figure A2-4. Page 64 of operations manual for Dimatix DMP 2831 Printer.

center nozzle #8 in the middle of the screen and put nozzle 8 in the **Jetting Nozzle** box. By clicking the cursor in the box it turns the nozzle on and moves it up to the 0 line.

Note: The **Calibrate Nozzle View** feature can also be accessed by selecting the **Calibrate Nozzle View** option of the **Tool** menu.

1.3 Cleaning Box

If you want to do a maintenance cycle to improve jetting, you can do that by clicking on the **Run Now** button on the **Cleaning** box in the upper left corner of the window.

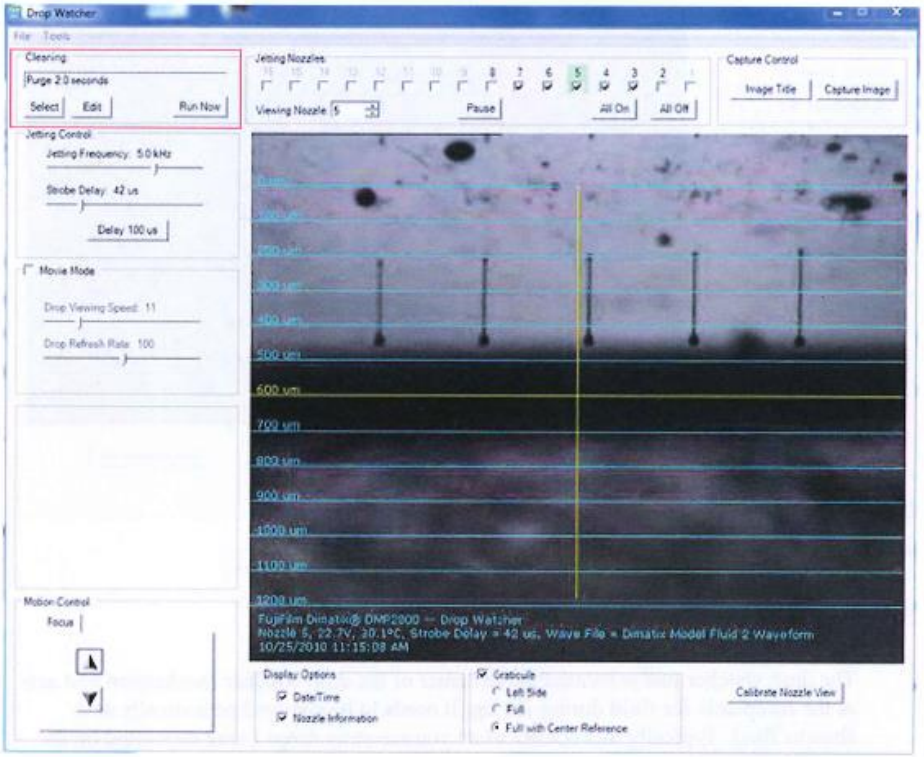

Figure 6 - 4 Cleaning box

1.4 Motion Control Box

There are two arrow buttons near the bottom left of the screen, which allow you to **Focus** the drop watcher camera on the nozzles and drops by clicking repeatedly until the image is

Figure A2-5. Page 65 of operations manual for Dimatix DMP 2831 Printer**.**

in focus. Holding down these buttons results in the camera moving with increased increments.

Figure 6 - 5 Motion Control box

1.5 Drop Watcher Pad

The drop watcher pad is located in the center of the drop watcher mechanism and acts as the receptacle for fluid during jetting. It needs to be changed periodically as it absorbs fluid. Typically this occurs when you see stray drops being deposited on the nozzle surface during drop watching or fluid is covering the side of the pad holder. To replace the pad simply pull out the holder and insert a new one.

1.6 Viewing Modes

The drop watcher system provides you with two different viewing modes.

If you select the **Movie Mode** check box, it lets you watch a stroboscopic movie of drops in flight as they are ejected from the nozzle. This is real time continuous jetting

Figure A2-6. Page 66 of operations manual for Dimatix DMP 2831 Printer.

Appendix III

Dimatix DMP 2831 Pattern Maker

1.1 Predefined Standard Patterns

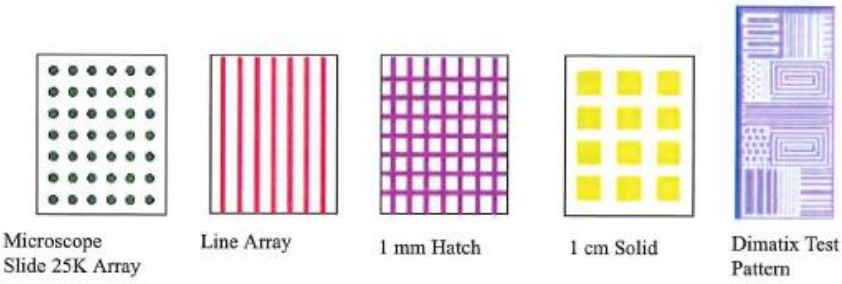

Figure 5 - 2 Predefined test patterns

2.0 Create Your Own Pattern

The **Pattern Editor** lets you create or modify patterns of drops for printing, and easily repeat them over the entire substrate if needed. The basic pattern, at the lowest level, (**Pattern Array**) is a collection of rectangles that are called pattern **Drop Position Arrays**. Each of these rectangles may be small enough to represent a single drop, or thin enough to represent a line of drops, or large enough to represent a fully filled-in rectangular area.

In all cases, X increases to the right, and Y increases toward the front of the printer. All dimension parameters are in millimeters except for the **Drop Spacing**, which is in micrometers. All dimensions entered into the pattern generator are rounded onto the Drop Spacing.

Figure A3-1. Page 39 of operations manual for Dimatix DMP 2831 Printer**.**

By selecting the **Edit** button on the **Select Pattern** screen the following screen appears:

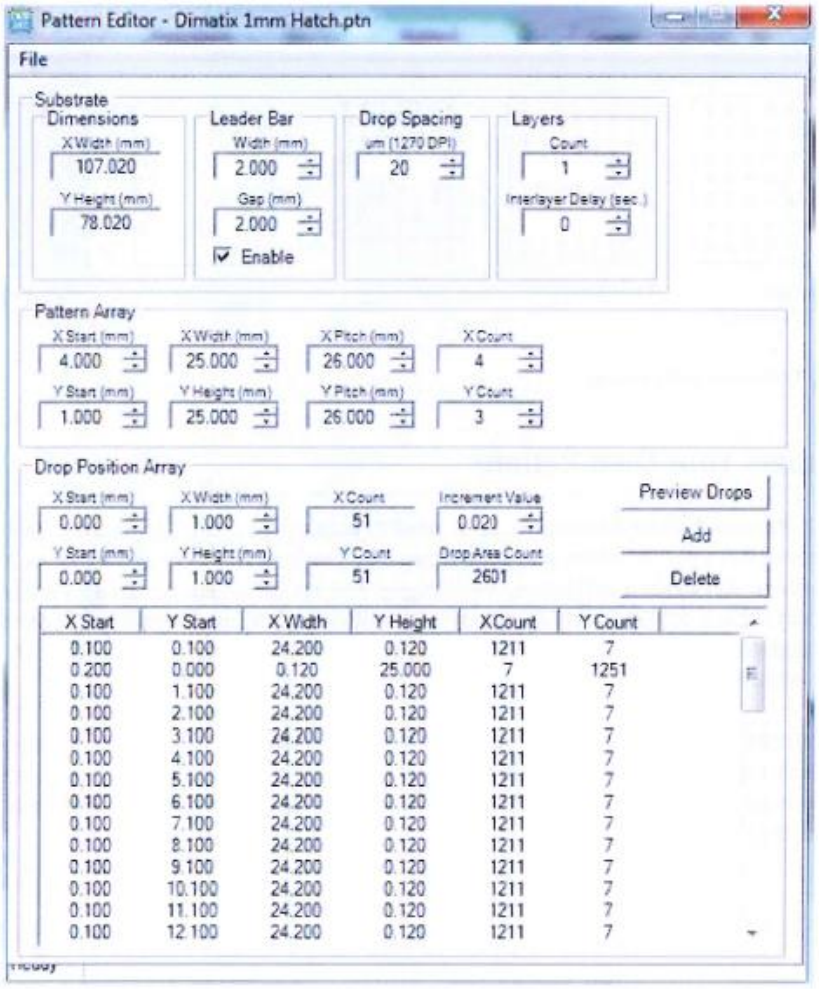

Figure 5 - 3 Pattern Editor screen

2.1 Substrate

The **Dimensions** is the total area to print. Generally most people jet on only a single substrate. But you could place several smaller substrates on the platen and jet on all of them at once. Verify that the total area is not larger than your substrate.

The **Leader Bar** is a vertical bar that can be jetted to the left of your pattern by checking the **Enable** box. This is a commonly used procedure in ink jet printing to pre-

Figure A3-2. Page 40 of operations manual for Dimatix DMP 2831 Printer**.**

jet nozzles to keep them active and their drop velocity uniform to improve pattern quality. The **Width** of it and the **Gap** of the leader bar can be entered in the boxes.

Note: Your pattern is automatically shifted to the right when you create a leader bar by the amount of gap and width. It is not automatically returned to its original position if you later decide to disable the leader bar.

The **Drop Spacing** is the center to center distance from one drop to the next in X and Y position to create the pattern. Although this value can be adjusted in 1 µm increments it is always rounded to the next 5 µm increment as soon as you start printing this pattern file. The X spacing is controlled by the x axis encoder, while the y axis is controlled by the cartridge angle.

Note: For the first print outs of Dimatix Model Fluid on ink jet paper a drop spacing of about 20 µm usually gives good printing results.

The **Layers** box feature allows you to reprint the same pattern over itself automatically. The **Count** number is the number of times you want to print the pattern and the **Interlayer Delay** is the delay time between each layer, additional to the amount of time spent doing any before print or after print maintenance on the cartridge.

If you click on the **Preview Drops** button, a window pops up showing the area you have designated. The total area of the window represents the platen. If the substrate area you entered is smaller than the platen it shows as a beige shape inside the white area.

Figure A3-3. Page 41 of operations manual for Dimatix DMP 2831 Printer.

Your **Pattern Array** area is delineated within the substrate area outlined.

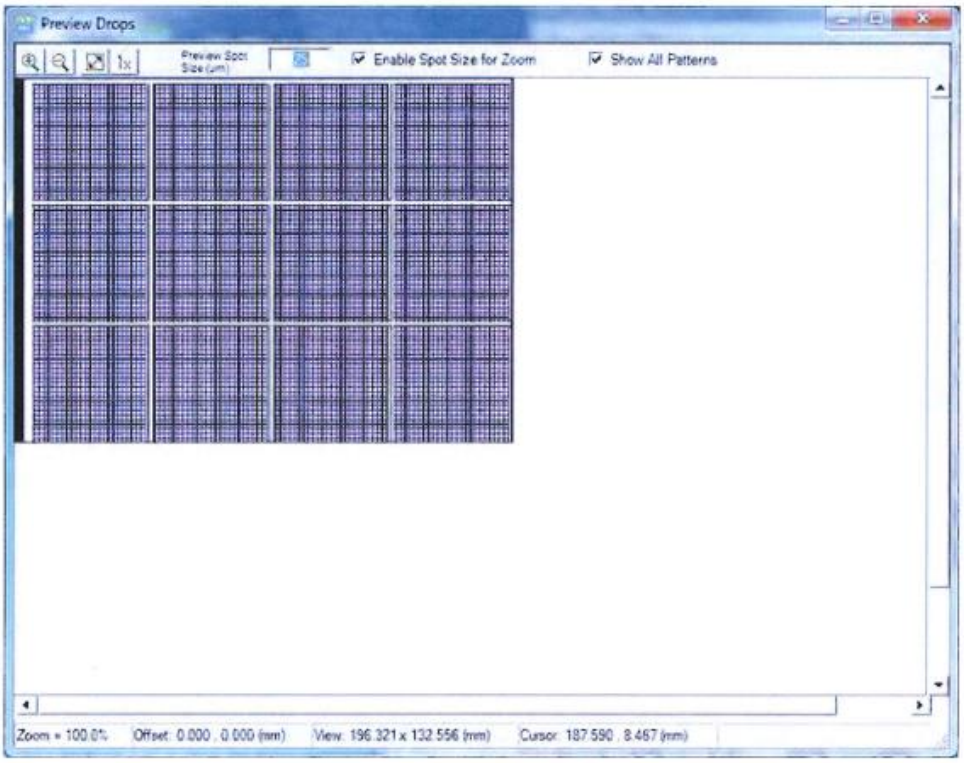

Figure 5 - 4 Pattern Block Array

2.2 Pattern Block Array

In the **Pattern Array** box enter the point on your substrate where you want the pattern to start printing in X and Y, referencing from the print origin. Then enter the **X width** and **Y height** of the block you want to make. The X and Y sizes entered should be at least large enough to enclose the collection of rectangles defined in the **Drop Positions Array** box (see below).

Note: The default print origin is approximately -1 mm, 7 mm (x,y) from the 0,0 corner scribed in the back left of the platen. See the *Fiducial Camera* section of this manual for more information.

To print a repetitive array of the pattern block in your print area, enter the X and Y **Pitch** dimensions. The **Pitch** is the distance from the start of one pattern to the next. Enter the number of patterns (**X count**) to print in the *horizontal* direction, and the number of patterns (**Y count**) to print in the *vertical* direction.

Figure A3-4. Page 42 of operations manual for Dimatix DMP 2831 Printer.

Appendix IV

Dimatix DMP 2831 Fiducial Camera

Chapter 7

Fiducial Camera

On the main **DDM** window go into the **Tools** menu and select **Fiducial Functions** or click on the gray **Fiducial Camera** button in the lower left.

Figure 7 - 1 Fiducial Camera screen

Figure A4-1. Page 79 of operations manual for Dimatix DMP 2831 Printer**.**

The above image is a sample screen shot of the main **Fiducial Camera** window. The fiducial camera is used when you want to deposit a pattern on a pre-patterned substrate, or if you are jetting a layer with a different cartridge material or to inspect the printed features.

The **Camera Field of View**. This has a width of 1.62 mm and a height of 1.22 mm with a resolution of 2.54 µm per pixel.

The **Fiducial Camera** operates in a **Dark Field** or a **Bright Field** mode. Therefore there are two different light sources the operator can select. The following picture illustrates the hardware switch positions on the camera for the different illumination modes.

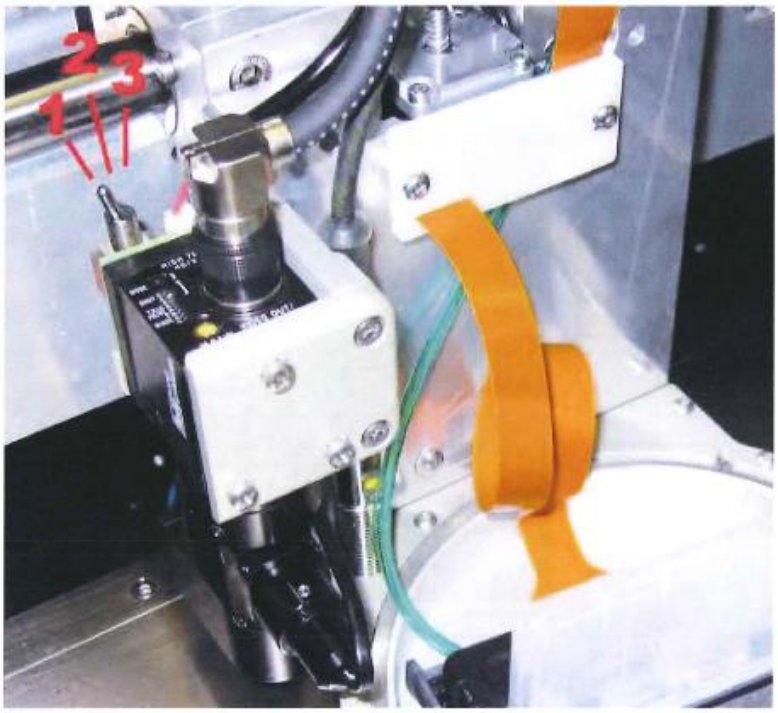

Figure 7 - 2 Camera switch for different illumination modes

- Position 1: **Bright Field** mode
- Position 2: both light sources are switched on
- Position 3: **Dark Field** mode

The **Dark Field** mode (switch position 3) allows viewing clear fluids on highly reflective surfaces. It requires very low light intensity only. Move the **Light Intensity** slider almost all the way to the left. In this mode the light source illuminates the sample

Figure A4-2. Page 80 of operations manual for Dimatix DMP 2831 Printer.

in a way that the objective only collects scattered light from the substrate. This results in dark backgrounds with bright objects on top of them. The **Bright Field** mode (switch position 1) works after the same principle as a regular microscope. The light shines on the object and gets directly reflected back into the objective. It requires a high light intensity, so the **Light Intensity** slider has to be moved all the way to the right.

Note: The gain pot located on the top of the camera can be adjusted to one extreme or the other to improve the range of the **Light Intensity** slider for either bright or dark field mode.

1.0 Features

- **Light Intensity** – This slider allows you to adjust the light intensity of the camera to optimize the contrast of the image.
- **Use Reference Point** – By checking this box the DMP positions the pattern's reference point to the **Image Reference Point**. It does this only with the Fiducial Camera window open. If you do not use the reference point, the image is printed from the print origin.
- The position of the **Reference Point** you have selected relative to the selected **Print Origin** is displayed in the **X and Y position text fields**. This is the physical point on the substrate that you want to align a .bmp file for printing.
- **Move to Reference Point** – This button moves the center crosshair to the position of the reference point.
- **Set Reference Point** – This feature lets you select the reference point in the video screen. More detailed instructions for this feature can be found in the *Alignment Procedures* chapter.

Note: A reference point an only be used for imported .bmp images; not for Dimatix Patterns generated with the Pattern Generator. See .bmp printing for more information.

Figure A4-3. Page 81 of operations manual for Dimatix DMP 2831 Printer.

Appendix V

Characterization Equipment

Figure A5-1. Image of a BURKER NANO Dimension 3100 AFM.

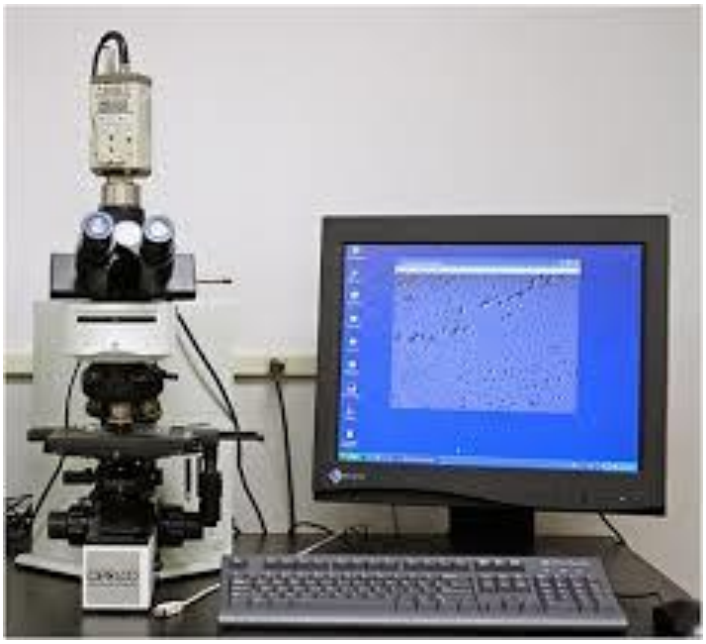

Figure A5-2. Image of an Olympus BX60 Optical Microscope.

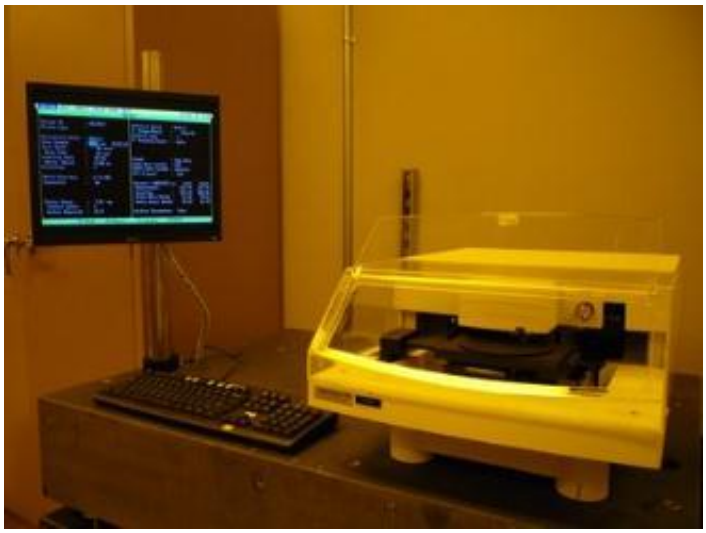

Figure A5-3. Image of an Alpha Step 500 Surface Profilometer.

Figure A5-4. Image of a Helios Nano Lab 400 Scanning Electron Microscope.

Figure A5-5. Image of a Bruker D8 Focus Powder X-Ray Diffractometer.

Figure A5-6. Image of a Mocon Ox-Tron 2/60 Oxygen and Moisture analyzer.

Appendix VI

Smithers Pira Marketing Information

Transparent Barrier Films market is forecast to reach $8.2 billion by 2017

09 August 2012

The global market for transparent barrier films is worth $6.7 billion in 2012 and is forecast to grow by 4.3% during the five-year period to 2017 to reach $8.2 billion according to a new study by Smithers Pira. Demand for transparent barrier film is being driven by a number of key trends ranging from socio-economic, demographic and lifestyle changes to the development of new materials, innovations in existing materials and emerging trends within end-use segments.

The Future of Transparent Barrier Films - Global Market Forecasts to 2017 examines global market and technology trends for transparent barrier films for the period 2007-12 and presents forecasts for the five-year period to 2017. Market forecasts are presented by geographic market, material, and end-use sector. In addition to packaging markets, the report includes an assessment of the future prospects for transparent barrier films in fast-growing electronics applications such as photovoltaic modules and displays, as well as other non-packaging markets.

According to the study, polymer materials used for the manufacture of transparent barrier films can be grouped into three broad categories. Barrier base web materials (including PA, PET, PP, PE, and PVC), barrier polymers (EVOH, PVdC, PEN and fluoropolymers), and inorganic barrier coatings such as silicon oxide (SiOx) and aluminum oxide (AlOx).

Global transparent films market: share by base web material, 2012 (%)

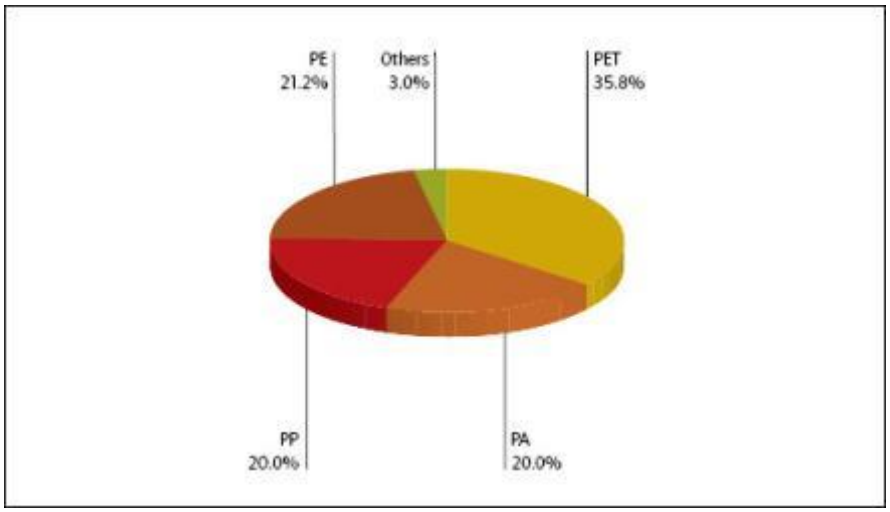

Source: Smithers Pira

PET is the most widely used barrier web, followed by PE, PA, and PP. PET and PA-based transparent barrier films are forecast to grow at the highest rates over the forecast period. PET film will be driven by the further development of barrier food packaging applications and further growth in the thick film (>50µ) market, spurred on by developments in photovoltaic and flat-screen applications. PA film will benefit from growth in demand for retort stand-up pouches as an alternative to cans and glass jars, along with growth in pharmaceutical packaging applications.

EVOH is the most widely used transparent barrier polymer. It is gaining share, mainly due to environmental concerns about PVdC in Northern Europe and the US, and from aluminum, in spite of difficulties related to poor water-barrier characteristics.

Barrier Coatings

Barrier coatings are set to show the fastest growth for transparent barrier film materials over forecast period.

Inorganic vapor coatings used for transparent barrier films include silicon oxide (SiOx), aluminum oxide (AlOx) and ormocers. Global consumption of transparent barrier films using inorganic barrier coatings are forecast to grow during the period 2012-17 at a CAGR of 8.2%, which is almost twice as high as the transparent barrier films market as a whole. Inorganic barrier coatings are applied almost exclusively to food packaging such as retort and microwavable packaging, lidding for meat packs, dry foods, and stand-up pouches. Barrier coatings will benefit from growing consumer demand for more convenient and microwavable products and the longer shelf life that these materials provide.

https://www.smitherspira.com/market-reports/transparent-barrier-films-market-is-forecast-to-reach-8-2-billion-by-2017.aspx

Global high barrier packaging film consumption forecast to reach 2.24 million tons by 2019

28 April 2014

Global high barrier packaging film consumption is at approximately 1.76 million tons in 2014 with a value of $15.9 billion. This is forecast to grow at a CAGR of 5.0% between 2014 and 2019 according to a new market report by Smithers Pira.

The Future of High Barrier Packaging Films to 2019 examines global market trends for high barrier packaging films for the period 2008-13, and also presents forecasts for the five-year period from 2014-19. Market forecasts are presented by high barrier polymer type, packaging product, end-use sector, and geographic region. This report also contains

an analysis of industry structure, major market participants, market drivers and trends and cutting-edge technology developments.

In this report, high barrier packaging films are defined as flexible films that are smaller than 250µ in gauge with an oxygen gas transmission rate in the range <5cm³/m²/day (25µ films). Market data in the report includes base webs, plus high barrier film/coating and tie or sealing layers.

According to The Future of High Barrier Packaging Films to 2019, there is a growing demand for packaging materials that give even greater protection to their contents. This is especially noticeable in the food, beverage and pharmaceutical industries. As plastics have become more and more common, concerns have arisen about their ability to allow the exchange of gases and vapors that can compromise the quality and safety of packaged products. Therefore, a variety of barrier technologies have been commercialized that preserve, protect and promote; optimize shelf life, reduce the need for preservatives, provide transparency and gloss, and serve as a printing substrate. Without this barrier, packaging, perishable goods such as food, beverages, and pharmaceuticals would be susceptible to a wide range of deterioration processes.

However, barrier packaging is restricted by factors such as susceptibility to degradation, recycling problems and cost. EVOH, for example, is water sensitive because absorption of atmospheric moisture reduces its barrier properties towards oxygen and carbon dioxide. Mechanical recycling also becomes a problem with multilayer structures containing more than one type of plastic, as they cannot easily be recycled. Environmental pressure groups have also raised concerns about increases in the amount of food packaging, with many companies responding by reducing their packaging.

High barrier films are found in six main flexible packaging products: bags and pouches, stand-up pouches, (retort and non-retort), tray lidding film, forming webs, wrapping film and blister pack base webs. According to the report, bags and pouches are by far the leading pack type accounting for over half of global high barrier packaging film consumption in 2014. Forming webs and lidding film are the next largest pack types.

Stand-up pouches are forecast to grow at the fastest rate during the five-year period to 2019. Stand-up pouches offer brand owners product differentiation and strengthen brand loyalty, while providing customers with convenience, and the ability to retort and microwave. Lidding film and forming webs are also set to grow at higher than the market average rate. The trend toward case-ready fresh meat packaged in trays under low-oxygen MAP will drive growth in barrier film lid stock and forming webs. Wrapping film, on the other hand, is forecast to grow at a relatively low rate, mainly as a result of slow growth in key end-use sectors such as baked goods and snack foods.

https://www.smitherspira.com/market-reports/packaging/news/global-high-barrier-packaging-film-consumption-forecast-to-2019.aspx

Intelligent Packaging and Recyclability to be Top Two Disruptive Technologies in Flexible Packaging

27 March 2014

The top five disruptive technologies in flexible packaging are forecast to be intelligent (smart) packaging, recyclability, packaging open ability, bio based polymers and digital printing, according to a new market report by Smithers Pira.

Ten-Year Forecast of Disruptive Technologies in Flexible Packaging to 2023 identifies and assesses technological, economic, consumer, sociological, environmental, and regulatory developments, and trends, which will impact the flexible packaging industry over the next 10 years to 2023. The 25 highest ranked developments were selected for further study with regard to their impact on the flexible packaging supply chain, commercial products and associated technologies and trends. Based on current flexible packaging markets, the center of attention within the report is inevitably food and beverage packaging, but other applications are considered including pharmaceuticals, household chemicals, medical devices, and electronics, together with a wide range of flexible packaging materials including plastics, paper, and metal foils.

Because of growing consumer focus on convenience and sustainability, general flexible packaging use has been growing rapidly worldwide both in absolute and percentage terms. It is gaining market share from other packaging formats such as rigid packaging. This growth is projected to continue because flexible packaging, particularly pouch packaging, uses less energy and materials, and has lower transport costs, environmental impact, and carbon footprint than its rigid counterparts.
These current trends concerning flexible packaging and rapid growth are anticipated to continue and increase over the next 10 years to 2023. There will be continuous development of new flexible packaging products for new markets and applications encroaching on traditional rigid packaging. High growth is expected in Europe and North America, as well as in the emerging markets of Asia and Central and South America.

Important drivers from a manufacturing viewpoint will include savings in materials, manufacturing and transportation costs and increased line filling speeds for pouches to match those for rigid bottles. From the consumer viewpoint, two important drivers will be the growing focus on convenience and sustainability.

The new market study states that the innovation in and implementation of smart and active packaging over the next 10 years will be the key disruptive factor affecting the flexible packaging industry. So far, these technologies have been retarded by high cost, consumer resistance to items such as sachets in packaging, and concerns about excessive packaging. However, the deployment of intelligent packaging is expected to become much more frequent with decreasing cost, increasing emphasis on food safety, anti-counterfeiting, new regulations, and brand owner/consumer demand. These technologies, particularly together with printed electronics and digital printing, will become more widespread in the years to 2023. This will lead to dramatically expanded perceptions of

the function of packaging, beyond the traditional containment, preservation, protection and identification to include a wide range of monitoring, tracking, warning, remediation, authentication, communication and brand protection.

According to the report, the second most disruptive technology in flexible packaging is recyclability. Because of the small amount of material used in a flexible package, it generates much less waste than other formats. However, it is not currently feasible to mechanically recycle postconsumer flexible packaging because of its thin film structure, multi-layered composition, and often contamination by food waste. This situation could create problems with the sustainability and recyclability goals of many major corporations or with the reduced or zero landfill policies of many governments. More easily recyclable materials and barrier structures, including monolayers, are expected to be introduced over the next 10 years, but this will not resolve the problem unless improved collection, sorting and recycling infrastructure is implemented.

https://www.smitherspira.com/market-reports/news/disruptive-technologies-in-flexible-packaging.aspx

The Future of Specialty Films to 2018

The global specialty films market is projected to be worth $22.4 billion in 2013 and is forecast to grow 5.4% annually to reach $29.1 billion by 2018. The range of specialty films on the market is broad, with very different properties and functions adding value for the consumer. Film types are also at different stages of development and exhibit different supply/demand dynamics and growth potential. **The Future of Specialty Films to 2018** explains it all, providing projections of opportunities, drivers, and technical and product developments, which are underpinned by detailed five-year market forecasts that will give you exclusive insights into regional growth, consumer trends, regulatory changes, and new applications.

https://www.smitherspira.com/market-reports/packaging/specialty-films-2018.aspx

LITERATURE CITED

1) Andres, C. M., & Kotov, N. A. Inkjet Deposition of Layer-by-Layer Assembled Films. *J. of the Amer. Chem. Soc.* **132**(41), 14496-14502 (2010).

2) Bharadwaj, R. K., Mehrabi, A. R., Hamilton, C., Trujillo, C., Murga, M., Fan, R. Chavira, A., & Thompson, A. K. Structure–property relationships in cross-linked polyester–clay nanocomposites. *Polymer* **43**(13), 3699-3705 (2002).

3) Nielsen, L. E. Models for the Permeability of Filled Polymer Systems. *Journal of Macromol. Sci. (Chem.) A1* ***B*** *(5*), 929-942 (1967).

4) Arys, X., Jonas, A. M., Laguitton, B., Legras, R., Laschewsky, A., & Wischerhoff, E. Structural studies on thin organic coatings built by repeated adsorption of polyelectrolytes. *Prog. Org. Coat.* **34,** 108-118 (1998).

5) Derocher, J. P., Gettelfinger, B. T., Wang, J., Nuxoll, E. E., & Cussler, E. L. Barrier membranes with different sizes of aligned flakes. *J. Membr. Sci.* **254**(1), 21-30 (2005).

6) Kamal, M. R, & Jinnah, I. A. Permeability of oxygen and water vapor through polyethylene/polyamide films. *Polym. Eng. Sci.* **24**(17), 1337-47 (1984).

7) Data Sheet, SELAR OH Barrier Resins, EI DuPont De Nemours and Company, Wilmington, DE (1990).

8) Brydges, W. T., Gulati, S. T., & Baum, G. Permeability of glass ribbon-reinforced composites. *J. Mater. Sci.* **10**(12), 2044-49 (1975).

9) Fredrickson, G. H., Bicerano, J. Barrier properties of oriented disk composites. *Journal of Chemical Physics* **110**(4), 2181-88 (1999).

10) Sweet, R. G. High frequency recording with electrostatically deflected ink-jets. *Rev. Sci. Instrum.* **36**(2), 131-136 (1965).

11) Le, H. P. Progress and Trends in Ink-jet Printing Technology, Progress and Trends in Ink-jet Printing Technology. *J. of Imaging Science and Technology* **42**(1), 49-62 (1998).

12) Zoltan, S. L. (Clevite Corp.) Pulse droplet ejection system, U.S. Patent 3683212 (1974).

13) Kyser, E. L., & Sears, S. B. (Silonic Inc.) Method and apparatus for recording with writing fluids and drop projection means therefore, U.S. Patent 3946398 (1976).

14) Decher, G. Fuzzy nanoassemblies: Toward layered polymeric multicomposites. *Science* **277**(5330), 1232–1237 (1997).

15) Tang, Z. Y., Wang, Y., Podsiadlo, P., & Kotov, N. A. Biomedical Applications of Layer-by-Layer Assembly: From Biomimetics to Tissue Engineering. *Adv. Mater*. **18** (24), 3203–3224 (2006).

16) Tang, Z. Nanostructured artificial nacre. *Nat. Mater.* **2**(6), 413–18 (2003).

17) Podsiadlo, P.; Kaushik, A. K.; Arruda, E. M.; Waas, A. M.; Shim, B. S.; Xu, J. D.; Nandivada, H., Pumplin, B. G., Lahann, J., Ramamoorthy, A. & Kotov, N. A. Ultrastrong and Stiff Layered Polymer Nanocomposites. *Science* **318**(5847), 80–83 (2007).

18) Mamedov, A. A., Kotov, N. A., Prato, M., Guldi, D. M., Wicksted, J. P., & Hirsch, A. Molecular design of strong single-wall carbon nanotube/polyelectrolyte multilayer composites. *Nat. Mater.* **1**(3), 190–194 (2002).

19) Hammond, P. T. Form and Function in Multilayer Assembly: New Applications at the Nanoscale. *Adv. Mater*. **16**(15), 1271–1293 (2004).

20) Ariga, K., Lvov, Y., Onda, M., Ichinose, I., & Kunitake, T. Alternate layer-by-layer assembly of organic dyes and proteins is facilitated by pre-mixing with linear polyions. *Chem. Lett.* **1**, 125–126 (1997).

21) Kotov, N. A., Dekany, I., & Fendler, J. H. Layer-by-Layer Self-Assembly of Polyelectrolyte-Semiconductor Nanoparticle Composite Films. *J. Phys. Chem*. **99**(35), 13065–69 (1995).

22) Tan, H. L., McMurdo, M. J., Pan, G., & Van Patten, P.G. Temperature Dependence of Polyelectrolyte Multilayer Assembly. *Langmuir* **19**(22), 9311-14 (2003).

23) McAloney, R. A., Sinyor, M., Dudnik, V., & Goh, M. H. Atomic Force Microscopy Studies of Salt Effects on Polyelectrolyte Multilayer Film Morphology. *Langmuir* **17**(21), 6655-6663 (2001).

24) Decher G., Science 277 (1997).

25) Decher G., Hong J.D., Schmitt J., Thin Solid Films 210/211 831 (1992).

26) Lvov Y., Decher G., Höhwald M., Langmuir 481 (1993).

27) Bertrand, P., Jonas, A., Laschewsky, A., & Legras, R. Ultrathin polymer coatings by complexation of polyelectrolytes at interfaces: suitable materials, structure and properties. *Macromol. Rapid Comm.* **21**(7), 319-348 (2000).

28) Decher G., & Schlenoff, J. B., Multilayer thin films: Sequential assembly of nanocomposite materials, Wiley-VCH: Weinheim, Germany (2003).

29) Nolan, C. M., Serpe, M. J., & Lyon, L.A. Thermally Modulated Insulin Release from Microgel Thin Films. *Biomacromolecules* **5**(5), 1940-46 (2004).

30) Kim, J. H., Kim, S. H., & Shiratori, S. Fabrication of nanoporous and hetero structure thin film via a layer-by-layer self assembly method for a gas sensor. *Sensors and Actuators B* **102**(2) 241-247 (2004).

31) DeLongchamp, D. M., & Hammond, P. T. Highly Ion Conductive Poly(ethylene oxide)-Based Solid Polymer Electrolytes from Hydrogen Bonding Layer-by-Layer Assembly. *Langmuir* **20**(13), 5403-5411 (2004).

32) Yao G. J., Wang, B. Q., Dong, Y. P., Zhang, M. F., Yang, Z. H., Yao, Q. L., Yip, L. J. W., & Tang, J. Self-assembly and photovoltaic properties of multilayer films based on partially doped polyaniline and poly(4-carboxyphenyl)acetylene. *Polym. Sci. A Polym. Chem*. **42**(13), 3224-29 (2004).

33) Von Klitzing, R., & Tieke, B. Polyelectrolyte Membranes. *Adv. Polym. Sci*. **165**, 177-210 (2004).

34) Sui, Z. J., Salloum, D., & Schlenoff, J. B. Effect of Molecular Weight on the Construction of Polyelectrolyte Multilayers: Stripping versus Sticking. *Langmuir* **19**(6), 2491-95 (2003).

35) Kolarik, L., Furlong, D. N., Joy, H., Struijk, C., & Rowe, R. Building Assemblies from High Molecular Weight Polyelectrolytes. *Langmuir* **15**(23), 8265-75 (1999).

36) Tan, H. L., McMurdo, M. J., Pan, G., & Van Patten, P.G. Temperature Dependence of Polyelectrolyte Multilayer Assembly. *Langmuir* **19**(22), 9311-14 (2003).

37) Büscher, K., Karlheinz, G., Ahrens, H., & Helm, C. A. Influence of Adsorption Conditions on the Structure of Polyelectrolyte Multilayers. *Langmuir* **18**(9), 3585-91 (2002).

38) Mermut, O., & Barrett, C. J. Effects of Charge Density and Counterions on the Assembly of Polyelectrolyte Multilayers *Journal of Physical Chemistry B* **107**(11) 2525-2530 (2003).

39) Dubas, S. T., & Schlenoff, J. B. Factors Controlling the Growth of Polyelectrolyte Multilayers. *Macromolecules* **32**(24), 8153-60 (1999).

40) Decher, G., Hong, J. D., & Schmitt, J. Buildup of ultrathin multilayer films by a self-assembly process: III. Consecutively alternating adsorption of anionic and cationic.

41) Lvov, Y., Decher, G., & Höhwald, M. Assembly, structural characterization, and thermal behavior of layer-by-layer deposited ultrathin films of poly(vinyl sulfate) and poly(allylamine). *Langmuir* **9**(2), 481-486 (1993).

42) Ramsden, J. J., Lvov, Y. M., & Decher, G. Determination of optical constants of molecular films assembled via alternate polyion adsorption. *Thin Solid Films* **254**(1-2), 246-251 (1995).

43) Decher, G., and Schmitt, J. Fine-Tuning of the film thickness of ultrathin multilayer films composed of consecutively alternating layers of anionic and cationic polyelectrolytes. *Progress in Colloids and Polymer Science: Trends in Colloid & Interface Science VI* **89,** 160-164 (1992).

44) McAloney, R. A., Sinyor, M., Dudnik, V., & Goh, M. H. Atomic Force Microscopy Studies of Salt Effects on Polyelectrolyte Multilayer Film Morphology. *Langmuir* **17**(21), 6655-6663 (2001).

45) Elbert, D. L., Hebert, C. B., & Hubbell, J. A. Thin Polymer Layers Formed by Polyelectrolyte Multilayer Techniques on Biological Surfaces. *Langmuir* **15**(16), 5355-62 (1999).

46) Picart, C., Mutterer, J., Richert, L., Luo, Y., Prestwich, G. D., Schaaf, P., Voegel, J. C., & Lavalle, P. Molecular basis for the explanation of the exponential growth of polyelectrolyte multilayers. *PNAS* **99**(20), 12531-35 (2002).

47) Lavalle, P., Gergely, C., Cuisinier, F. J. G., Decher, G., Schaaf, P., Voegel, J. C., & Picart, C. Comparison of the Structure of Polyelectrolyte Multilayer Films Exhibiting a Linear and an Exponential Growth Regime: An in Situ Atomic Force Microscopy Study. *Macromolecules*

48) Mattoussi, H., Radzilowski, L. H., Dabbousi, B. O., Thomas, E. L., Bawendi, M. G., & Rubner, M. F. Electroluminescence from heterostructures of poly(phenylene vinylene) and inorganic CdSe nanocrystals. *J. Appl. Phys.* **83**(12), 7965-74 (1998).

49) Aliev, F. G., Correa-Duarte, M. A., Mamedov, A., Ostrander, J. W., Giersig, M., Liz- Marzan, L. M., Kotov, N. A. Layer-By-Layer Assembly of Core-Shell Magnetite Nanoparticles: Effect of Silica Coating on Interparticle Interactions and Magnetic Properties. *Adv. Mater*. **11**(12), 1006-10 (1999).

50) Vossmeyer, T., Guse, B., Besnard, I., Bauer, R. E., Mullen, K., & Yasuda, A. Gold Nanoparticle/Polyphenylene Dendrimer Composite Films: Preparation and Vapor-Sensing Properties. *Adv. Mater*. **14**(3) 238-42 (2002).

51) Park, J., Fouche, L. D., & Hammond, P. T. Multicomponent Patterning of Layer-by-Layer Assembled Polyelectrolyte/Nanoparticle Composite Thin Films with Controlled Alignment. *Adv. Mater*. **17**(21), 2575-79 (2005).

52) Treacy, M. M. J., Ebbesen, T. W., & Gibson, J. M., Exceptionally high Young's modulus observed for individual carbon nanotubes. *Nature* **381**(6584), 678-680 (1996).

53) Yu, M. F., Lourie, O., Dyer, M. J., Moloni, K., Kelly, T. F., & Ruoff, R. S. Strength and Breaking Mechanism of Multiwalled Carbon Nanotubes Under Tensile Load. *Science* **287**(5453), 637-40 (2000).

54) Breuer, O., & Sundararaj, U. Big returns from small fibers: A review of polymer/carbon nanotube composites. *Polym. Compos.* **25**(6), 630-645 (2004).

55) Lier, G. V., Alsenoy, C. V., Doren, V. V., & Geerlings, P. Ab initio study of the elastic properties of single-walled carbon nanotubes and grapheme. *Chem. Phys. Lett*. **326**(1-2), 181-85 (2000).

56) Sturcova, A., Davies, G. R., & Eichhorn, S. J. Elastic Modulus and Stress-Transfer Properties of Tunicate Cellulose Whiskers. *Biomacromolecules* **6**(2), 1055-61 (2005).
58. Manevitch, O. L., & Rutledge, G. C. Elastic Properties of a Single Lamella of Montmorillonite by Molecular Dynamics Simulation. *J. Phys. Chem. B* **108**(4), 1428-35 (2004).

57) Mack, J. J., Viculis, L. M., Ali, A., Luoh, R., Yang, G., Hahn, H. T., Ko, F. K., & Kaner, R. B. Graphite Nanoplatelet Reinforcement of Electrospun Polyacrylonitrile Nanofibers. *Adv.Mater*. **17**(1), 77-80 (2005).

58) Samir, M. A. S. A., Alloin, F., & Dufresne, A. Review of Recent Research into Cellulosic Whiskers, Their Properties and Their Application in Nanocomposite Field. *Biomacromolecules* **6**(2), 612-626 (2005).

59) Ray, S. S., & Okamoto, M. Polymer/layered silicate nanocomposites: A review from preparation to processing. *Prog. Polym. Sci*. **28**(11), 1539-1641 (2003).

60) P Podsiadlo, AK Kaushik, EM Arruda, AM Waas, BS Shim, J Xu, H Nandivada, BGpumplin, J Lahann, A Ramamoorthy, NA Kotov, Science 318 (2007) 80.

61) FG Aliev, MA Correa-Duarte, A Mamedov, JW Ostrander, M Giersig, LM Lis-Marzán, NA Kotov, Layer-By-Layer Assembly of Core-Shell Magnetite Nanoparticles: Effect of Silica Coating on Interparticle Interactions and Magnetic Properties *Adv. Mater*. **11**(12), 1006-1010 (1999).

62) Z Tang, NA, S Magonov, B Ozturk, *Nat. Mater.* **2**(6), 413-18 (2003).

63) Podsiadlo, P., Tang, Z., Shim, B.S., & Kotov, N. A. Counterintuitive Effect of Molecular Strength and Role of Molecular Rigidity on Mechanical Properties of Layer-by-Layer Assembled Nanocomposites. *Nano Letters* **7**(5), 1224-31 (2007).

64) Ingersoll, D., Kulesza, P. J., & Faulkner, L. R. Polyoxometallate-Based Layered Composite Films on Electrodes: Preparation Through Alternate Immersions in Modification Solutions. *J. Electrochem. Soc*. **141**(1), 140- (1994).

65) NA Kotov, I Dekany, JH Fendler, J. Phys. Chem. 99 (1995) 13065.

66) AA Mamedov, NA Kotov, M Prato, DM Guldi, JP Wicksted, A Hirsch, Nat. Mater. 1 (2002) 190.

67) Jiang, C., Ko, H., & Tsukruk, V. V. S train-Sensitive Raman Modes of Carbon Nanotubes in Deflecting Freely Suspended Nanomembranes. *Adv. Mater*. **17**(17), 2127-31 (2005).

68) Greenemeier, L., *Scientific American*, News-October 11 2007 [http://www.sciam.com/article.cfm?id-8F6AA474-E7F2-99DF-3332C34C30DF9269&prin…]

69) Dagani, R. Here comes paper 2.0. *Chem. Eng. News* **79**(3), 40-43 (2001).

70) Seeboth, A., Schneider, J., & Patzak, A. Materials for intelligent sun protecting glazing. *Sol. Energy Mater. and Sol. Cells* **60**(3), 263-77 (2000).

71) Green, M., *Chem. Ind.* **17** 641- (1996).

72) Monk, P. M. S., Mortimer, R. J., & Rosseinsky, D. R. Electrochromism: Fundamentals and Applications; Weinheim: New York (1995).

73) Mortimer, R. J. Organic electrochromic materials. *Electrochimica Acta* **44**(18), 2971-81 (1999).

74) Bach, U., Corr D., Lupo, D.,Pichot, F., & Ryan, M. Nanomaterials-Based Electrochromics for Paper-Quality Displays. *Adv. Mater.* **14**(11), 845-848 (2002).

75) DeLongchamp, D. M., Kastantin, M., & Hammond, P. T. High-Contrast Electrochromism from Layer-By-Layer Polymer Films. *Chem. Mater*. **15**(8), 1575-86 (2003).

76) DeLongchamp, D. M., & Hammond, P. T. Layer-by-Layer Assembly of PEDOT/Polyaniline Electrochromic Devices. *Adv. Mater.* **13**(19), 1455-59 (2001).

77) Dong, H.M., Doctoral Thesis (2006).

78) Zhang, X.G. & Basaran, O.A. An Experimental-Study of Dynamics of DropFormation. *Physics of Fluids* **7**(6), 1184-1203 (1995).

79) Dong, H.M., Carr, W.W., & Morris, J.F. An experimental study of drop-on-demand drop formation. *Physics of Fluids* **18**(7) 072102-01 – 072102-16 (2006).

80) Eggers, J. Nonlinear dynamics and breakup of free-surface flows. *Reviews ofModern Physics* **69**(3), 865-929 (1997).

81) Tekin, E., de Gans, B.J., & Schubert, U.S. Ink-jet printing of polymers - from single dots to thin film libraries. *Journal of Materials Chemistry* **14**(17) 2627-2632 (2004).

82) Sawhney, A., et al. Soft-structured sensors and connectors by inkjet printing. *Aatcc Review* **7**(6), 42-46 (2007).

83) Sirringhaus, H., et al., High-resolution inkjet printing of all-polymer transistor circuits. *Science* **290**(5499), 2123-2126 (2000).

84) Kim, J., et al., The spontaneous metal-sitting structure on carbon nanotube arrays positioned by inkjet printing for wafer-scale production of high sensitive gas sensor units. *Sensors and Actuators B-Chemical* **135**(2) 587-591 (2009).

85) Batchelor, J.C., et al., Inkjet printing of frequency selective surfaces. *Electronics Letters* **45**(1), 7-8 (2009).

86) Barret, M., Sanaur, S., & Collot, P. Inkjet-printed polymer thin-film transistors:Enhancing performances by contact resistances engineering. *Organic Electronics* **9**(6) 1093-1100 (2008).

87) Mabrook, M.F., et al., The morphology, electrical conductivity and vapour sensing ability of inkjet-printed thin films of single-wall carbon nanotubes. *Carbon* **47**(3), 752-757 (2009).

88) Kelly, P.F., King, R.S.P., & Mortimer R. J. Fingerprint and inkjet-trace imaging using disulfur dinitride. *Chemical Communications* **46**, 6111-6113 (2008).

89) Xu, T., et al., Inkjet-Mediated Gene Transfection into Living Cells Combined with Targeted Delivery. *Tissue Engineering Part A* **15**(1), 95-101 (2009).

90) Xu, T., et al., Inkjet gene printing: A novel approach to achieve gene modified cells for tissue engineering. *Tissue Engineering Part A* **14**(5), 869-870 (2005).

91) Xu, T., et al., Inkjet gene printing: A novel approach to achieve gene modified cells for tissue engineering. *Tissue Engineering Part A* **14**(5), 869-870 (2005).

92) Saunders, R.E., Gough, J.E., & Derby, B. Delivery of human fibroblast cells by piezoelectric drop-on-demand inkjet printing. *Biomaterials* **29**(2), 193-203 (2008).

93) Derby, B., Bioprinting: inkjet printing proteins and hybrid cell-containing materials and structures. *Journal of Materials Chemistry* **18**(47), 5717-5721 (2008).

94) Li, Y.C., et al., Inkjet Printed Electrode Arrays for Potential Modulation of DNA Self-Assembled Monolayers on Gold. *Analytical Chemistry* **80**(22), 8814-8821 (2008).

95) Antohe, B. V., Wallace, D. B. Acoustic phenomena in a demand mode piezoelectric ink jet printer. *J. Imaging Sci. Technol.* **46**, 409–14 (2002).

96) Reis, N., Ainsley, C., & Derby B. Ink-jet delivery of particle suspensions by piezoelectric droplet ejectors. *J. Appl. Phys.* **97**, 094903 (2005).

97) Reis N., Ainsley C., Derby B. Ink-jet delivery of particle suspensions by piezoelectric droplet ejectors. *J. Appl. Phys.* **97**:094903 (2005).

98) Hoyt, J.W. & Taylor, J.J. Turbulence structure in a water jet discharging in air. *Physics of Fluids* **20**(10), S253-S257 (1977).

99) Martin, G. D., Hoath, S. D., & Hutchings, I. M. Inkjet printing: the physics of manipulating liquid jets and drops. *J. Phys. Conf. Ser.* **105**, 012001 (2008).

100) Rouse, P.E., A theory of the linear viscoelastic properties of dilute solutions of coiling polymers. *Journal of Chemical Physics* **21**(7), 1272-1280 (1953).

101) Zimm, B.H., Dynamics of polymer molecules in dilute solution - viscoelasticity, flow birefringence and dielectric loss. *Journal of Chemical Physics* **24**(2), 269-278 (1956).

102) Hsieh, C.C., Li, L., & Larson, R. G. Modeling hydrodynamic interaction in Brownian dynamics: Simulations of extensional flows of dilute solutions of DNA and polystyrene. *Journal of Non-Newtonian Fluid Mechanics* **113**(2-3) 147-191 (2003).

103) Liu, Y.G., Jun, Y. G., & Steinberg, V. Concentration dependence of the longest relaxation times of dilute and semi-dilute polymer solutions. *Journal of Rheology* **53**(5) 1069-1085 (2009).

104) Tirtaatmadja, V., McKinley, G.H., & Cooper-White, J. J. Drop formation and breakup of low viscosity elastic fluids: Effects of molecular weight and concentration. *Physics of Fluids* **18**(4), 043101-01 – 043101-18 (2006).

105) Christanti, Y.& Walker, L. M. Effect of fluid relaxation time of dilute polymer solutions on jet breakup due to a forced disturbance. *Journal of Rheology* **46**(3) 733-748 (2002).

106) Christanti, Y. & Walker L. M., Surface tension driven jet break up of strainhardening polymer solutions. *Journal of Non-Newtonian Fluid Mechanics* **100**(1-3) 9-26 (2001).

107) Shore, H.J. and Harrison, G. M. The effect of added polymers on the formation of drops ejected from a nozzle. *Physics of Fluids*, 2005. **17**(3), 7 (2005).

108) Xu, D., et al., Inkjet printing of polymer solutions and the role of chain entanglement. *Journal of Materials Chemistry* **17**(46), 4902-4907 (2007).

109) Schiaffino S., & Sonin A. A. Molten droplet deposition and solidification at low Weber numbers. *Phys. Fluids* **9**, 3172–87 (1997).

110) Yarin, A. L. Drop impact dynamics: splashing, spreading, receding, bouncing. *Ann. Rev. Fluid Mech*. **38**, 159–92 (2006).

111) Rioboo, R., Marengo, M., & Tropea, C. Time evolution of liquid drop impact onto solid, dry surfaces. *Exp. Fluids* **33**, 112–24 (2002)

112) Tanner LH. 1979. Spreading of silicone oil droplets on horizontal surfaces. *J. Phys. D Appl. Phys.* 12:1473– 84.

113) Stow CD, Hadfield MG. 1981. An experimental investigation of fluid-flow resulting from the impact of a water drop with an unyielding dry surface. *Proc. R. Soc. London Ser. A* 373:419–41

114) Deegan, R. D., Bakajin, O., Dupont, T. F., Huber, G., Nagel, S. R., & Witten, T. A. Capillary flow as the cause of ring stains from dried liquid drops. *Nature* **389**, 827–29 (1997).

115) CH Klute, J. Appl. Polym. Sci. 1 (1959) 340.

116) Nielsen, L. E. Models for the Permeability of Filled Polymer Systems. *Journal of Macromol. Sci. (Chem.) A1* ***B****(5*), 929-942 (1967).

117) EL Cussler, SE Hughes, WJ Ward, R Aris, Journal of Membrane Science 38 (1988) 161.

118) Maxwell, J. C. Treatise on Electricity and Magnetism, Vol. I, Claredon Press, London (1881).

119) Perry, D., Ward, W. J., & Cussler, E. L. Unsteady diffusion in barrier membranes. *Journal of Membrane Science* **44**(2-3), 305-11 (1989).

120) Eitzman, D. M., Melkote, R. R., & Cussler, E. L. Barrier membranes with tipped impermeable flakes. *AIChE J*. **42**(1), 2-9 (1995).

121) Kamal, M. R, & Jinnah, I. A. Permeability of oxygen and water vapor through polyethylene/polyamide films. *Polym. Eng. Sci.* **24**(17), 1337-47 (1984).

122) Data Sheet, SELAR OH Barrier Resins, EI DuPont De Nemours and Company, Wilmington, DE (1990).

123) Falla, W. R., Mulski, M., & Cussler, E. L. Estimating diffusion through flake-filled membranes. *Journal of Membrane Science* **119**(1), 129- (1996).

124) Yang, C., Smyrl, W. H., & Cussler, E. L. Flake alignment in composite coatings. *Journal of Membrane Science* **231**(1-2), 1-12 (2004).

125) Lape, N. K., Nuxoll, E. E., & Cussler, E. L. Polydisperse flakes in barrier films. *Journal of Membrane Science* **236**(1-2), 29-37 (2004).

126) Fredrickson, G. H., Bicerano, J. Barrier properties of oriented disk composites. *Journal of Chemical Physics* **110**(4), 2181-88 (1999).

127) PH Messersmith, P. H., & Giannelis, E. P. Synthesis and barrier properties of poly(ε-caprolactone)-layered silicate nanocomposites. *Journal of Polymer Science Part A-Polymer Chemistry* **33**(7), 1047-57 (1995).

128) Giannelis, E.P. Polymer Layered Silicate Nanocomposites. *Adv. Mater.* **8** (1), 29-35 (1996).

129) Giannelis, E. P. Polymer-layered silicate nanocomposites: Synthesis, properties and applications. *Applied Organometallic Chemistry* **12**(10-11), 675-680 (1998).

130) Osman, M. A., Rupp, J. E. P., & Suter, U. W. Gas permeation properties of polyethylene-layered silicate nanocomposites. *J. Mater. Chem.* **15**, 1298-1304 (2005).

131) Sanchez-Valdes, S., López-Quintanilla, M. L., Ramírez-Vargas, E., Medellín-Rodríguez, F. J., & Gutierrez- Rodríguez, J. M. Effect of Ionomeric Compatibilizer on Clay Dispersion in Polyethylene/Clay Nanocomposites. *Macromol. Mater. Eng.* **291**(2), 128-136 (2006).

132) Koo, W. H., Jeong, S.M., Choi, S. H., Baik, H. K., Lee, S. M., & Lee, S. J. Water Vapor Barrier Properties of Transparent SnO2−SiOx Composite Films on Polymer Substrate. *Journal of Physical Chemistry B* **108**(49), 18884-89 (2004).

133) Vaia, R. A., Ishii, H., & Giannelis, E. P. Synthesis and properties of two-dimensional nanostructures by direct intercalation of polymer melts in layered silicates. *Chem. Mater*. **5**(12), 1694-96 (1993).

134) Lebaron, P., Wang, Z., & Pinnavaia, T. Polymer-layered silicate nanocomposites: An overview. *J. Appl. Clay Sci*. **15**(1-2), 11-29 (1999).

135) Bharadwaj, R. K., Mehrabi, A. R., Hamilton, C., Trujillo,C., Murga, M., Fan, R. Chavira, A., & Thompson, A. K. Structure–property relationships in cross-linked polyester–clay nanocomposites. *Polymer* **43**(13), 3699-3705 (2002).

136) Krishnamoorti, R., & Giannelis, E. P. Rheology of End-Tethered Polymer Layered Silicate Nanocomposites. *Macromolecules* **30**(14), 4097-4102 (1997).

137) MA Osman, JEP Rupp, UW Suter, J. Mater. Chem. 15 (2005) 1298.

138) Osman, M. A., Mittal, V., Morbidelli, M., & Suter, U. W. Macromolecules 37 (2004) 7250.

139) Nazarenko, S., Meneghetti, P., Julmon, P., Olson, B. G., & Qutubuddin, S. Gas barrier of polystyrene montmorillonite clay nanocomposites: Effect of mineral layer aggregation. *Journal of Polymer Science B* **45**(13)**,** 1733-1753 (2007).